Doctoral theses at NTNU, 2017:220

André Kapelrud

Spin pumping, spin transfer, and spin Hall effects in magnetic insulator-normal metal systems

NTNU
Norwegian University of
Science and Technology

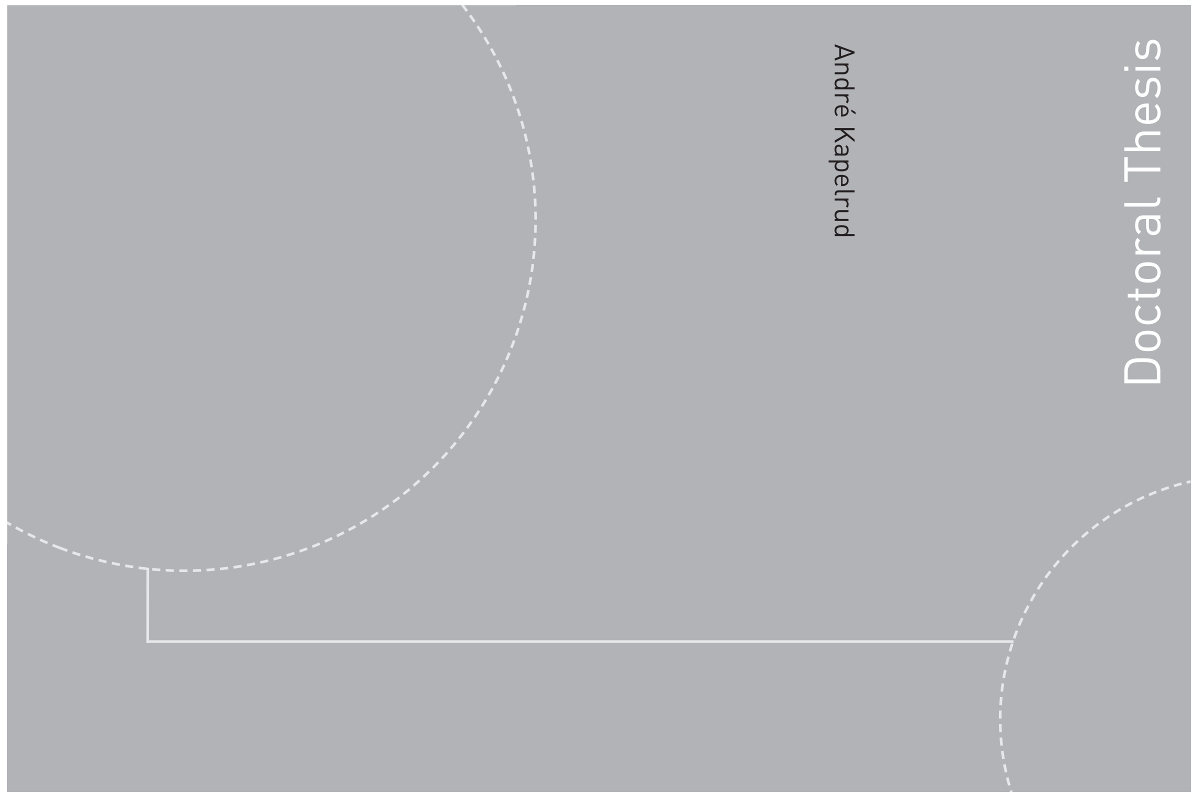

Doctoral Thesis

André Kapelrud

Doctoral theses at NTNU, 2017:220

NTNU
Norwegian University of Science
and Technology
Faculty of Natural Sciences
Department of Physics

NTNU

ISBN 978-82-326-2512-3 (printed version)
ISBN 978-82-326-2513-0 (electronic version)
ISSN 1503-8181

NTNU
Norwegian University of
Science and Technology

André Kapelrud

Spin pumping, spin transfer, and spin Hall effects in magnetic insulator-normal metal systems

Thesis for the degree of Philosophiae Doctor

Trondheim, July 2017

Norwegian University of Science and Technology
Faculty of Natural Sciences
Department of Physics

NTNU
Norwegian University of
Science and Technology

NTNU
Norwegian University of Science and Technology

Thesis for the degree of Philosophiae Doctor

Faculty of Natural Sciences
Department of Physics

ISBN 978-82-326-2512-3 (printed version) ISBN
978-82-326-2513-0 (electronic version) ISSN
1503-8181

Doctoral theses at NTNU, 2017:220

Printed by Skipnes Kommunikasjon as

Abstract

This thesis presents four research papers on two topics within the field of spintronics. Three of the papers present theoretical models concerned with the topics of spin wave mode-dependent spin pumping, spin transfer, and spin Hall effects in ferromagnetic insulator–normal metal layered structures. The fourth paper details results from experiments investigating the training and recovery of the exchange bias effect in a metallic spin valve structure.

Paper I addresses the enhancement of the Gilbert damping that occurs due to the spin pumping effect from a precessing magnetization. We studied a ferromagnetic insulator in contact with a normal metal that is assumed to act as a perfect spin sink. In this paper we showed for the first time that the higher excited spin wave modes in the insulator film has twice as strong renormalization of the Gilbert damping as the uniform mode. We also show that the Gilbert damping renormalization for an easy-axis surface anisotropy-induced surface-localized spin wave mode can be an order of magnitude stronger than for the uniform mode.

Paper II extends the formalism of Paper I to a system consisting of a ferromagnetic insulator–normal metal–ferromagnetic insulator stack. We compute the Gilbert damping renormalization spectrum for both symmetric and antisymmetric film thickness configurations, and show that the modes are either acoustically or optically coupled across the metallic spacer layer. The acoustic and optical modes experience a different renormalization of the Gilbert damping, depending on the thickness ratio of the two insulator films, the nonlocal dipole–dipole interactions through the in-plane wave number, as well as the spin relaxation properties and conductivity of the metallic spacer layer. We also discuss how an easy-axis surface anisotropy can induce surface modes that are robust to thickness

mismatches of the two insulator films.

Paper III is a sequel to Paper I, and presents a more accurate model of the eigenmodes and their Gilbert damping renormalization in the bilayer system. In this paper we take the effect of spin back flow from the normal metal into account. The different permutations of the field configuration and the surface-anisotropy types are adressed, and measures for the alternating and direct inverse spin Hall effect are presented.

Paper IV presents findings related to the training effect in an exchange-biased metallic spin valve structure. High rate field sweeps were executed while performing magnetoresistive measurements on the valve. The measurements show reduced coercive field as a function of sweep iteration number. Upon pausing the field sweeps, the coercive field was shown to recover towards its initial state at a speed depending on the sweep rate, sweep number and the rest interval length in a logarithmic fashion.

Contents

Preface

This thesis is submitted in partial fulfillment to the requirements of the degree of *Philosophiae Doctor* (Ph.D.) at the *Norwegian University of Science and Technology* (NTNU). During my time as a Ph.D. student I have done obligatory coursework consisting of four courses at 7.5 study points each, the total being equivalent to one semester. Three of the four courses were Ph.D.-level courses, while one was a Master level course. In total one quarter of the first four years were spent performing teaching duties in student labs for the courses: Measurement Techniques, Instrumentation, and Physics. The latter for non-physics students. During the 2011 fall semester I lectured, as well as prepared and corrected exams, for the undergrad course "Physics 2".

I started out in Erik Wahlström's Scanning Tunneling Microscopy group, were I worked in close collaboration with Magne Saxegaard on his scanning tunneling microscope purpose-built for point contact measurements.[1] There, I mainly spent my time focusing on instrumentation electronics and software design for the experemental setup. After 9 months I changed fields from Wahlström's experimental group to Arne Brataas' spintronics theory group. As part of Brataas' spintronics group, I have focused my attention on the phenomenon of mode dependent spin pumping, spin transfer and spin Hall effects in ferromagnetic insulator–normal metal layered structures.

The work was mostly performed at the Department of Physics, NTNU, with the exception of two semesters I spent as a guest in Gerrit E.W. Bauer's group in the Theoretical Physics research group at the Kavli Institute of Nano Science at Delft University of Technology, the Netherlands.

The outline of the thesis is as follows: Chapter 1 sets the stage for this thesis by taking a look at the current state of electronics and by introducing the reader to the appropriate sub field of physics; Chapter 2 recapitulates some core concepts related to magnetism in condensed matter; Chapter 3 focuses on the details of spin wave dynamics in thin-film ferromagnetic insulators; while Chapter 4 presents a review of the main findings of the four scientific papers this thesis is built around. Some of the implementation details that are not discussed directly in the papers can also be found in this chapter.

This thesis uses Gaussian *centimetre–gram–second* (cgs) units throughout. Using a system of units other than *Système international d'unités* (SI) is becoming increasingly difficult to justify these days. Nevertheless, most journal articles and treaties on magnetism from the previous century that I have read as a part of working on this thesis were written in Gaussian units. cgs units were common in works on magnetism because of the advantage offered by having all Maxwellian fields share the same basic units. This removes some of the complexity hidden in the units of the constants μ_0 and ε_0 in the SI system of units. It is my personal opinion that the Gaussian form of Maxwell's equations, and most equations derived from those equations, are the easiest to work with. A nice summary of unit systems in relation to Maxwell's equations can be found within Jackson[2].

Being a Ph.D. student has been an interesting and sometimes very challenging endeavor. The immense joy when calculations give results and papers are published stand in deep contrast to sign errors, dead ends, and the sometimes grueling months inbetween the minor successes. It might be that the process of finalizing a body of work the size of a thesis makes you vulnerable to an academic equivalent of the "Stockholm syndrome"; all the hardships seem to be overshadowed by the nostalgia towards that time when you invested all your efforts into solving a hard problem and succeeded.

As a "senior" Ph.D. student I hope that I have been helpful to those that started after me; both through discussions regarding spintronics and by readily providing my own notes on the subject with them. I also hope that this thesis can be of use too someone trying to get into the field of spintronics and spin dynamics.

André Kapelrud
Trondheim, Norway
July 24, 2017

List of Papers

Paper I: A. Kapelrud, and A. Brataas
«Spin Pumping and Enhanced Gilbert Damping in Thin Magnetic Insulator Films»

Physical Review Letters 111, 097602 (2013)

Paper II: H. Skarsvåg, A. Kapelrud, and A. Brataas
«Spin Waves in Ferromagnetic Insulators Coupled via a Normal Metal»

Physical Review B 90, 094418 (2014)

Paper III: A. Kapelrud and A. Brataas
«Spin pumping, dissipation, and direct and alternating inverse spin Hall effects in magnetic-insulator/normal-metal bilayers»

Physical Review B 95, 214413 (2017)

Paper IV: D.Z. Yang, A. Kapelrud, M. Saxegaard, and E. Wahlström
«Training and recovery behaviors of exchange bias in FeNi/Cu/Co/FeMn spin valves at high field sweep rates»

Journal of Magnetism and Magnetic Materials, 324, 3223-3226 (2012)

Clarification on the Author's Contributions to the Papers

- In the production of Paper I and III, I carried out the majority of the analytical calculations, designed and programmed the numerical code and executed the appropriate simulations using Mathematica. I was also the main author of the text and figures.

- In Paper II, I extended the numerical code from Paper I to a trilayer system after the analytical model created by the main author, Hans

Skarsvåg. I took part in the discussion of the results and in creating the code for the numerical analysis. I contributed with minor changes to the main text. I also provided the Mathematica code to produce Figure 1b, while Figure 1a was adapted from code I provided.

- In Paper IV, I made parts of the instrumentation electronics, specifically the voltage-controlled current source that was used in the initial magnetoresistive measurements. I took part in the preliminary discussion of the measurement results. I also wrote the data storage routines and helped redesign parts of the software to allow higher data throughput.

Acknowledgements

This thesis would not have been possible without the immense support of my supervisor Arne Brataas. I joined his group at a time when he was ready to leave for his sabatical at Harvard. He arranged it so that I could visit Professor Gerrit. E.W. Bauer's group at the Kavli Institute of Nano Science at Delft University of Technology, the Netherlands. I want to express my gratitude both to Professor Bauer for welcoming me into his group and to Arne for the opportunity.

Arne, I am grateful for the supervision you have provided, the discussions and conversations we have had, as well as the patience you have shown me during these years.

Erik Wahlström deserves a big thank you, supervising me during the first part of my first year, and for supporting me when I made the switch to theory.

Special thanks are needed for the people I've collaborated with: Dezheng Yang for teaching me how to use an Scanning Tunneling Microscope (STM); Magne Saxegaard for including me in his interesting STM build and for setting an excellent example of what it means to be a dedicated Ph.D. student; Hans Skarsvåg for being my "sparring partner" in countless discussions on all things related to spintronics.

I would also like to sincerely thank all the great people I've met at the Department of Physics, here at NTNU, over the years. In roughly the "order of appearance": Einar, Henrik, Arne, Justin, Åsmund, Kjetil, Alireza, Severin, Jostein, Erlend, Peder, Vegard, Lars, Cecilia, Camilla, Peter, Eirik, Sverre, Therese, William, Eva, Stefan, and all the rest. Thanks for the countless discussions over coffee, workshops and seminars.

My friends from other related sciences that have been very supporting during the last years: Halvor, Erlend Magnus, Gard, Ingvild, Jørgen,

Sigrid, Siri-Malén, Femke and Wouter. You are the best!

I would like to express my gratitude towards my parents, Unni and Tormod, who have always supported me and pushed me forwards. I would probably not have reached this stage without the immense support from them and from my loving brother, Johan, who always led the way when we were younger and have continued to do so in our adult life. My grandparents have always been a source of inspiration and of support, two of whom I sadly lost during the past two years.

Thank you, Camilla, for babysitting Elida during the final weeks of me finishing the work on this thesis.

And last but not least.: Dear Inga, this thesis wouldn't have happened without your love. You never really asked to live with a Ph.D. student and all that entails, but you have nevertheless been with me all the way. You moved in with me the year I started my Ph.D., and willingly moved to the Netherlands with me the year after. Now we are well settled here in Trondheim, married and have the sweetest daughter together. You are both exceptionally wonderful!

Part I

Background

1 Introduction

1.1 The Current State of Electronics

The first commercially available microprocessor, the 4-bit Intel 4004, was released in 1971 by the Intel Corporation[3] and within a few years several companies were producing microprocessors at affordable rates. This lead to the era of the *personal computer* (PC), starting in the mid 1970s.

As a baseline, consider that some of the early PCs featured microprocessors from the beginning Intel 8-bit microprocessor range. The Intel 8080, released in 1974, had a 2 MHz clock frequency, 4500 on-chip transistors and a line width of 6 μm (about an order of magnitude smaller than the breadth of the human hair). Contrast this to the 8080's successor, the Intel 8086 released in 1978. It had an initial clock frequency of 5 Mhz, 29000 transistors and a 3 μm feature size. At the heart of this extreme development was Intel Co-founder Gordon E. Moore, who in 1965 had made the observation that the complexity for minimum cost was doubling every year[4;5]. The later emendation that the number of components per chip was expected to double every other year[6] has since proven to be a remarkable accurate prediction. It is aptly know as "Moore's law".

For the first four decades this trend was driven almost solely by the continued minituarization of the transistor and the resulting increased clock frequency. By the mid 2000s the frequency had hit 3.8 GHz with Intel's Pentium 4 line of microprocessors.[7] With an end-of-line feature size of 65nm, the Pentium 4 architecture was troubled with very high heat output, nearing 100W when stressed.

This lead to the introduction of *multi core* microprocessors, where the focus turned from "race car"-like raw speed to parallel computing for increased performance. The Intel Core 2 line of processors had from two to six on-chip cores that could be utilized for parallelization.

Adding several slower clocked computation cores to the microprocessor die have given us the benefit of still being able to uphold Moore's law with respect to the transistor count. However, the addition of more cores have put greater demands on the software programmer, in that parallel data algorithms cannot rely on data being synchronized across cores. Some software problems are also not easily parellelizable, so there isn't always beneficial to add more cores to a processor. At this time of writing (spring 2017) the number of cores in consumer level microprocessors are seldom over 8, with most models having 2 or 4 cores.[7] The fabrication process used in commercial production sits currently at 14 nm,[8] with companies soon to be pushing to 10nm processes.[7] The minituarization of the transistor is expected to end somewhere around 5 nm, where the transistor's gate has become so narrow that quantum mechanical tunneling becomes a major issue.

The goal of having biennual doubling of performance are now pursued differently from what is was in earlier decades. Currently, the semiconductor industry are trying to uphold Moore's law not only by minituarization and by adding more cores, but also by large architectural changes in the design of processors. A nonexhaustive list of such additional changes include:[7] less heat dissipation per transistor through advanced material design, making it possible to increase the lateral transistor density; more efficient macrostructures in the chips, leading to shortening of transmission lines between computation blocks; more dedicated function blocks embedded within the chip, decreasing the number of clock cycles spent per instruction; higher and faster cache levels and more efficient memory caching; faster peripherals, like faster *random access memory* (RAM) and hard drives.

The advent of the PC in the mid 1970s and the extreme improvement of the underlying technology has truly changed the way people work, are entertained and how we interact with each other. Over the last decades we have seen yearly leaps in performance and continued miniaturization of electronics, not only for the PC, but also for embedded electronics. The hand held devices of today all rely on battery powered multi-core processors with such a high performance one could only dream of just a decade ago. This has facilitated huge changes in our daily lives and on modern society as a whole.

In a way, the technology of today feeds its own progress, as a doubling of performance leads to increased potential applications and chance of new discoveries. The modern day physicist can utilize the new gained performance to investigate bigger and/or more complex systems. Hence, it should be argued that it is in *Physics'* best interest that researchers focus on improving solid state computing technology. As discussed above, the feature size of the transistors are likely to hit a limit in the near future. However, this comes as no surprise to our community where thousands of researchers have for already decades been working hard on finding and engineering new technology. One such field of research is in spin transport electronics, better known as *spintronics*, where we seek to gain control over the intrinsic spin of particles, both in isolation from and in combination with manipulating the electronic charge of them.

1.2 Spintronics

The orbital moment of particles is analogous to the orbital moment of a planet around a star, and the intrinsic spin of particles can conceptually be compared to a planet's rotation about itself. However, the quantum nature of particles dictate that the intrinsic spin is itself quantized.[9;10] Elementary particles are spin-$\frac{1}{2}$, meaning that the projection of the spin along a chosen measurement direction can take two values, usually referred to as "spin up" and "spin down". Manipulating the spins of individual particles is certainly possible, but in this thesis I will focus on what happens when multiple spins correlate.

The spin of localized electrons in a material can interact with neighbouring spins through the quantum mechanical *exchange interaction* originating from the Pauli exclusion principle.[11;12] In some materials the exchange interaction favors parallel alignment of the spins, resulting in a spontaneous breaking of symmetry. This is what we call ferromagnetism. From quantum mechanics we also know that the spin of a particle couples with magnetic fields, i.e. the particle spin has an assosciated magnetic moment. If the spins in a material align spontaneously, then the resulting nonzero total magnetic moment per unit volume is what we call the magnetization of the system. It is this magnetization we are interrested in manipulating, either directly by externally applied classical magnetic fields or by using some more novel effects from spintronics.

The birth of spintronics can arguably be attributed to the discovery of the *Giant Magnetoresistance* (GMR) effect. GMR was discovered independently by Fert[13] and Grünberg[14], for which they both were awarded the Nobel prize in Physics in 2007. The turnaround time from initial discovery in 1988 to commercial application in 1997, in the form of read heads in magnetic disc drives, was almost shockingly short.[15] Even though solid state drives (SSDs) based on conventional electronics have more or less taken over the consumer market for storage, disc drives are still important in storing large collections of data. This is because of the data density and the non-volatility of such drives.

The GMR effect occurs in *spin valve* structures, i.e. *ferromagnet* (FM)–*normal metal* (NM)–ferromagnet stacks. If one of the ferromagnets is engineered to be more rigid than the other layer, by means of exchange pinning to an adjoining antiferromagnet via the *exchange bias* effect[16] or because of it having a larger coercive field than the other FM, the magnetizations in the ferromagnets can be made to align or dealign by applying an external magnetic field. When electrons pass through the stack they will be spin polarized by the spin-split band structure in the ferromagnets. If the two ferromagnets are antialigned, the electrons are more likely to scatter when crossing the interface from the NM into the second FM. Relative to the aligned case this causes an increased electrical resistance across the spin valve. Another refinement of the GMR effect include the use of an insulating layer sandwitched inbetween the ferromagnets, creating what is known as *magnetic tunnel junctions* and where the magnetoresistive effect is suitable named the *tunnel magnetoresistance*.[1]

The *spin transfer torque* (STT) effect was independently predicted by Slonczewski[18] and Berger[19]. If a spin polarized current enters a FM with the electron spins noncollinear to the magnetization direction in the FM, the electron spins will start to precess around the equilibrium direction. Within a short material characteristic spin coherence length the spins will have dephased with one another.[20] Hence, the spin component perpendicular to the FM's equilibrium magnetization direction is effectively ab-

---

[1] The TMR effect was actually discovered before the GMR effect, but was forgotten until the early 90s.[17]

sorbed. This acts as a net torque on the magnetization. If the spin polarized current is strong enough, the torque will make the FM's magnetization precess with a larger cone angle around its equilibrium direction, and eventually switch into the opposite direction.[21] One demonstrated application of STT is in switching the magnetization state of the less rigid (free) layer in a spin valve by passing a current through the structure. This creates the possibility of using a spin valve as a memory device, where the alignment of the free and fixed layer can be thought of as a classical bit. RAM technology based on STT, so-called STT-MRAM, is currently one of the fastest RAM technologies out there, both in achieveable read and write bandwidths.[7]

It was later understood that there is an inverse to the STT effect; when a precessing FM is brought into contact with a NM, electrons that are either travelling through the FM, or are reflected off an FM–NM interface, pick up and carry away angular momentum from the FM. This effect is known as *spin pumping* (SP).[22–26] One of the side effects of spin pumping is the induced enhancement of the damping of the magnetization's precessional motion. This effect is well studied for the case of uniform magnetization within the FM.[22;23] If the magnetization within the FM is spatially and/or time dependent the effect of SP can be harder to predict, and this is one of the main topics of this thesis.

Magnonics

In the field of *Magnonics*,[27] dynamic excitations of the magnetization around the equilibrium are studied. If such an excitation is phase-coherent in the FM we call it a *spin wave* (SW)[28]. The characteristics of spin waves depend on several factors: the shape of the FM, any applied external magnetic fields (static or dynamic), long range magnetic dipolar interactions, local material properties and interfacial interactions with other materials (like STT and SP described above). All these properties combine to create spectra of spin wave eigenmodes within the ferromagnet.[29] The field of magnonics is not new in itself, as there was alot of activity in the 1950s through 1980s, but activity within this field of research picked up again as the spintronic effects were discovered.

Probably the most common material in use in the study of magnonics is the *ferromagnetic insulator* (FI) *yttrium-iron-garnet* (YIG), which is a synthetic crystal in the garnet family. The main reasons for the widespread use of YIG is because of its low intrinsic damping, orders of magnitude weaker than in metallic ferromagnets. Another remarkable property is that when YIG is put in contact with a normal metal, the local magnetization dynamics close to the interface couple to the spins of conduction electrons in the NM that are reflecting off of the FI-NM interface.[30] There has been renewed interrest in magnonics because of this discovery. It was shown experimentally that a travelling spin wave can be excited at one location using STT and detected somewhere else using the SP effect; the intermediate signal carried by a pure spin-wave signal with no transported charge carriers. This creates opportunities for isolating charge and spin, and possibly also for creating new devices based on pure spin-wave technology.

2 *Magnetism in Solids*

This chapter focuses on some prerequisites for discussing magnonics and spin wave dynamics in layered structures. Both relations from classical and quantum physics are needed, as the semiclassical models used in later chapters lean heavily on these basic concepts.

2.1 Relations from Classical Electrodynamics

We recall that classical electrodynamics are governed by Maxwell's equations[2;31]

$$\begin{aligned} \nabla\cdot\mathbf{B} &= 0, & \nabla\times\mathbf{H} &= \frac{4\pi}{c}\mathbf{J} + \frac{1}{c}\frac{\partial\mathbf{D}}{\partial t}, \\ \nabla\cdot\mathbf{D} &= 4\pi\rho, & \nabla\times\mathbf{E} &= -\frac{1}{c}\frac{\partial\mathbf{B}}{\partial t}, \end{aligned} \tag{2.1}$$

where **B** is the magnetic field, **H** is the free magnetic field, **E** is the electric field, **D** is the electric displacement field, and **J** is the free electric current density. The **H**- and **D** fields are defined through the relations

$$\mathbf{B} = \mathbf{H} + 4\pi\mathbf{M}, \quad \mathbf{D} = \mathbf{E} + 4\pi\mathbf{P}, \tag{2.2}$$

where **M** is the material's magnetization and **P** is the electric polarization of the medium. I will defer discussing the electric field until Sec. 2.5.4.

The magnetic dipole moment is a pseudovector classically defined with the help of the free current density

$$\boldsymbol{\mu} = \int \frac{1}{2c}\mathbf{r}\times\mathbf{J}(\mathbf{r})\,d\mathbf{r} \tag{2.3}$$

where c is the speed of light and $\mathbf{r}$ is the position vector. The simplest example is a current loop, giving $\boldsymbol{\mu} = \frac{I\mathbf{A}}{c}$, where $|\mathbf{A}|$ is the enclosed area of the loop, the direction $\hat{\mathbf{A}} = \mathbf{A}/|\mathbf{A}|$ is normal to the loop plane given by the right hand rule from the current's circulation direction, and I is the circulating current's magnitude.

Most often, it is more appropriate to work with the dipole moment density, the *magnetization*, given by

$$\mathbf{M}(\mathbf{r}) = \frac{1}{2c}\mathbf{r} \times \mathbf{J}(\mathbf{r}), \tag{2.4}$$

which is the term under the integral sign in Eq. (2.3),

A magnetic moment in a magnetic field, $\mathbf{B}$, experiences a torque

$$\boldsymbol{\tau} = \frac{\partial \mathbf{L}}{\partial t} = \boldsymbol{\mu} \times \mathbf{B}, \tag{2.5}$$

where $\mathbf{L}$ is the assosciated classical angular momentum. This torque is acting to align the magnetic moment with the field. The force experienced by a dipole moment $\boldsymbol{\mu}$ in a field is given by $\mathbf{F} = \nabla(\boldsymbol{\mu} \cdot \mathbf{B})$, so the potential energy of a dipole moment in a magnetic field is given by

$$F_d = -\boldsymbol{\mu} \cdot \mathbf{B}. \tag{2.6}$$

Now, the dipole field, $\mathbf{B}_d = \mathbf{B}_d(\mathbf{r})$, emanating from a dipole moment itself is given by

$$\mathbf{B}_d(\mathbf{r}) = \frac{3\mathbf{r}(\mathbf{r} \cdot \boldsymbol{\mu})}{|\mathbf{r}|^5} - \frac{\boldsymbol{\mu}}{|\mathbf{r}|^3}, \tag{2.7}$$

which together with Eq. (2.6) implies that a magnetization experiences a non-local dipole–dipole interaction between different points in the magnetized body. This is explored in greater detail in Sec. 2.5.2 as well as in Chapter 3.

2.1.1 Free Energy

The *Helmholtz free energy* of a system is the Legendre transform of the internal energy of the system $F = U(S, \mu) - TS$, where S is the entropy and T is the temperature.[32] Through the definitions in Eqs. (2.3) and (2.4), the free energy density is a function of the system's magnetization. Thus, the total free energy of the system becomes a functional of the magnetization, written as $F = F[\mathbf{M}]$. Because of Eqs. (2.6) and (2.2), the classical $\mathbf{H}$-field can be extracted from the total free energy functional by means of a variational derivative

$$\mathbf{H} = -\frac{\delta F_d[\mathbf{M}]}{\delta \mathbf{M}}. \tag{2.8}$$

This fundamental relation comes in handy when discussing the different effective field contributions in a dynamic, magnetized system in Sec. 2.5.

2.1.2 Boundary Conditions

Integrating Maxwell's equations over a small pillbox volume straddling an interface and letting the pillbox thickness across the interface tend to zero provides the boundary conditions required by the equations. For magnetic fields these are

$$H_1^{\parallel} = H_2^{\parallel}, \qquad B_1^{\perp} = B_2^{\perp}, \tag{2.9}$$

where the indices denote the two sides of the interface, $\perp$ ($\parallel$) denotes the field component perpendicular (parallel) to the interface, and the $\mathbf{B}_i$ fields are given by Eq. (2.2).

2.2 Relations from Quantum Mechanics

An object moving around some point of reference is said to have orbital angular momentum wrt. to that point. Elementary particles also have an intrinsic angular momentum known as spin,[9;10] of which the classical analog is an object's spin about its own center of mass. A typical classical example is the earth revolving around the sun (orbital) while at the same time rotating about itself (spin).

Let us recapitulate some key concepts learned in elementary quantum mechanics.[33;34]. Quantum mechanics tells us that the spin angular momentum of particles is $S = \hbar\sqrt{s(s+1)}$, where $\hbar$ is the reduced Planck constant, and where the spin quantum number, s, must be a half integer: $s = 0, \frac{1}{2}, 1, \frac{3}{2}, \ldots$ determined by the type of particle. Measuring the spin of a particle along any given direction gives us the spin component $S_i = \hbar m_s$ where $m_s \in \{-s, -s+1, \ldots, s-1, s\}$. In a cartesian basis, $\{S_i\}$, the commutator relation between individual spin components is given by

$$[S_i, S_j] = i\hbar\varepsilon_{ijk}S_k \tag{2.10}$$

where ε_{ijk} is the antisymmetric Levi-Civita tensor.

Like in the classical case (see Eq. (2.5)), a quantum mechanical angular momentum is accompanied by a magnetic dipolar moment. For the a free electron, the dipole moment is simply proportional to the spin

$$\boldsymbol{\mu}_S = -\gamma \mathbf{S} = -\frac{g_S |\mu_B|}{\hbar} \mathbf{S}, \quad |\mu_B| = \frac{e\hbar}{2m_e c}, \tag{2.11}$$

where e is the elementary charge, m_e is the electron mass, and c is the speed of light, and $g_S \approx 2$ is the electron's g-factor. For an electron in an atomic orbital both spin and orbital angular momentum contribute. The dipole moment assosciated with the orbital angular momentum is

$$\boldsymbol{\mu}_L = -\frac{g_L |\mu_B|}{\hbar} \mathbf{L}, \tag{2.12}$$

where we typically have $g_L = 1$. The dipole moment assosciated with the total angular momentum, $\mathbf{J} = \mathbf{L} + \mathbf{S}$, becomes

$$\boldsymbol{\mu}_J = -\frac{g_J |\mu_B|}{\hbar} \mathbf{J}, \quad g_J \approx \frac{3}{2} + \frac{s(s+1) - l(l+1)}{2j(j+1)}, \tag{2.13}$$

where g_J is known as the Landé g-factor which is found using perturbation theory. s, l and j are the quantum numbers associated with the spin, orbital and total angular momentum operators.

2.3 Atomic Magnetic Moments

Some materials have large magnetic moments, and thus interact strongly with magnetic fields. If the angular momentum of each atom in the bulk structure of a material does not interact with one another, the material would exhibit *paramagnetic* behaviour.[35] Upon applying an external magnetic field, each atom's dipole moment aligns with the field direction, but the magnetic order disappears when turning of the field due to thermal fluctuations.

Good examples of atomic elements with a finite dipole moment can be found among the transition metals, where the 3d atomic orbitals contribute to the angular momentum. An Fe^{2+} ion, with its 24 electrons, has a band filling of $1s^2\,2s^2\,2p^6\,3s^2\,3p^6\,3d^6$. The 3d subshell has quantum number $n = 3$ and orbital quantum number $l = 2$ with the azimuthal quantum number $m_l \in \{-2, -1, 0, 1, 2\}$. These 5 orbitals give $2(2l+1) = 10$ different single electron states. Considering that there are $\binom{10}{6} = 210$ possible ways of putting 6 electrons into the 10 different states, the question becomes: what spin state do these electrons organize them into in the ground state? Applying Hund's rules[33] to the case of Fe^{2+}, we find:

1. Maximize the total spin angular momentum, S_{tot}. 5 electrons fill into different orbitals so as to align their spins. The sixth electron must have opposite spin because of Pauli's exclusion principle. The total spin of the ground state becomes $S_{\mathrm{tot}} = 5 \cdot \frac{1}{2} - \frac{1}{2} = 2$.

2. Maximize the total orbital angular momentum, L. From the first rule, we know that 5 of the electrons occupy all the different m_l states. Their orbital angular momentum sums to zero. The total orbital angular momentum is thus maximized by having the sixth electron occupy the $m_l = 2$ orbital with spin down $m_s = -\frac{1}{2}$. Thus, $L = 2$, designated as D (from the word "diffuse") in spectroscopic notation.

3. The subshell is more than half-filled, so Hund's 3rd rule dictate that the total argular momentum should be maximized, giving $J = L + S = 4$.

Hence, the ground state of an Fe^{2+} ion is ${}^{2S_{\mathrm{tot}}+1}L_J = {}^5D_4$. Using these quantum numbers the dipole moment of a single Fe^{2+} ion, using Eq. (2.13) becomes $\mu_J = 6.7\mu_B$. This is only applicable to an isolated ion, and not correct for metallic Fe. When several Fe atoms combine to form a crystal structure the outer orbitals form metallic bonds with electrons in neighbouring atoms. These electrons become part of the conduction band and are shared in the crystal. In metallic Fe the orbital angular momentum of the 3d electrons is quenched by the crystal field of the surrrounding Fe atoms. The dipole moment per ion in bulk Fe is therefore lower in value than for a single Fe atom. It is found by experiment to be $\mu_J \approx 2.2\mu_B$.

If the magnetization of a material is proportional to the applied field, we say that the material exhibits linear *susceptibility*, where the susceptibility is defined through the relation

$$\mathbf{M} = \chi \mathbf{H} \,. \tag{2.14}$$

Because individual moments must fight thermal fluctuations it was expected that the susceptibility should diminish at increasing temperature. Pierre Curie showed us that the susceptibility of a paramagnetic material is inverse proportional to the temperature, $\chi = C/T$ (known as *Curie's law*), with C being Curie's constant. For non-interacting dipole moments in a paramagnetic material with total angular momentum quantum number J in a weak magnetic field (high temperature), the Curie constant is approximately given by

$$C \approx \frac{4\pi N (g_J \mu_B)^2 J(J+1)}{3k_B}, \tag{2.15}$$

where k_B is Boltzmann's constant, N is the number of (atomic) dipoles and g_J is the Landé g-factor from Eq. (2.13).[32;34]

2.4 Ferromagnetism

Adding an intrinsic *molecular field* to the magnetic **B** field when deriving Eq. (2.15), leads to the *Curie-Weiss* law

$$\chi = \frac{C}{(T - \Theta)}, \tag{2.16}$$

where Θ is the Weiss critical temperature. This relation describes ferromagnetic materials in the paramagnetic region above the ferromagnet's symmetry breaking phase transition. In real ferromagnets the critical temperature, the Curie temperature T_c, of the phase transition have been shown to be lower than the theoretical predictions following Curie-Weiss law.

Below the critical temperature a ferromagnet spontaneously develops magnetic order, even with no externally applied field. In a ferromagnetic material, localized spins align with neighbouring spins to form magnetic *Weiss domains*.[36;32] When an external magnetic field is applied the boundaries between the domains, the *domain walls*, move in such a way that the field aligned domains grow in size while the others shrink. The result is that the apparent susceptibility of ferromagnetic materials is much larger than it is for pure paramagnetic materials. Because of the spontaneous order existing in ferromagnets even with no externally applied field, they exhibit memory in the form of hysteresis when switching the direction of the applied field from one direction to another. The coercive field is the field strength required to demagnetize a ferromagnet when the ferromagnet has already reached its saturation magnetization.

We will now have a look at the mechanism that is normally attributed to causing magnetic ordering, the electrostatic exchange interaction.

2.4.1 Magnetic Order Due to Exchange Interactions

The symmetry of wave functions under coordinate exchange of two electrons' with overlapping orbitals were first considered by Heisenberg[11] and Dirac[12]. To understand how such a coordinate exchange can lead to magnetic order, consider an example system of two interacting atoms with two electrons, the simplest example being the H_2-molecule. The total Hamiltonian of the system can be modelled as

$$\mathcal{H} = \mathcal{H}_1 + \mathcal{H}_2 + \mathcal{H}_{\text{int}}, \tag{2.17}$$

where $\mathcal{H}_{\text{int}}$ describes the interaction between the atoms, and $\mathcal{H}_i$ is the single atoms' Hamiltonian when they are separate from eachother. In the following we neglect the effect of the interaction Hamiltonian on the individual spatial wavefunctions, φ_1 and φ_2, and assume that they are unchanged. If one electron is located at the coordinate $\mathbf{r}_1$ and the other at $\mathbf{r}_2$, the total spatial wave function can be described as either symmetric or antisymmetric with regards to interchange of the two electrons' positions ($\mathbf{r}_1 \leftrightarrow \mathbf{r}_2$). We define

$$\varphi_S(\mathbf{r}_1, \mathbf{r}_2) = \frac{1}{\sqrt{2}}[\varphi_1(\mathbf{r}_1)\varphi_2(\mathbf{r}_2) + \varphi_1(\mathbf{r}_2)\varphi_2(\mathbf{r}_1)], \quad \text{(symmetric)} \tag{2.18a}$$

$$\varphi_A(\mathbf{r}_1, \mathbf{r}_2) = \frac{1}{\sqrt{2}}[\varphi_1(\mathbf{r}_1)\varphi_2(\mathbf{r}_2) - \varphi_1(\mathbf{r}_2)\varphi_2(\mathbf{r}_1)]. \quad \text{(antisymmetric)} \tag{2.18b}$$

Similarly, the spin state of the system can be either antisymmetric or symmetric,

$$\chi_A = \frac{1}{\sqrt{2}}(\chi_{\uparrow\downarrow} - \chi_{\downarrow\uparrow}), \qquad \chi_S = \begin{cases} \chi_{\uparrow\uparrow} \\ \frac{1}{\sqrt{2}}(\chi_{\uparrow\downarrow} + \chi_{\downarrow\uparrow}) \\ \chi_{\downarrow\downarrow} \end{cases}, \tag{2.19}$$

where $\chi_{\uparrow\downarrow}$ denotes a total spin state with electron 1 having spin up (↑) and electron 2 having spin down (↓), etc.. Thus, the *triplet* (T) states $\{\chi_S\}$ have total spin number $S = s_1 + s_2 = 1$ while the *singlet* (S) state χ_A has total spin number $S = 0$.[33]

Pauli's exclusion principle demands for a fermionic system that the total wave function, $\Psi = \varphi(\mathbf{r}_1, \mathbf{r}_2)\chi$, of the system must be antisymmetric upon interchange of the two eletrons' state. Thus, combining the singlet and triplet states with the opposite symmetric spatial wavefunction give the possible total wave functions $\Psi_\mathrm{S} = \varphi_S\chi_A$ with assosciated energy $\varepsilon = \varepsilon_\mathrm{S}$ and $\Psi_\mathrm{T} = \varphi_A\chi_S$ with $\varepsilon = \varepsilon_\mathrm{T}$.

The total spin operator $\mathbf{S} = \mathbf{S}_1 + \mathbf{S}_2$ gives

$$\begin{aligned} \mathbf{S}^2\Psi_\mathrm{S} &= 0 \\ \mathbf{S}^2\Psi_\mathrm{T} &= \hbar^2 S(S+1)\Psi_\mathrm{T} = 2\hbar^2\Psi_\mathrm{T} \end{aligned} \tag{2.20}$$

Thus the Hamiltonian in Eq. (2.17) can be written as

$$\mathcal{H} = \varepsilon_\mathrm{S} + \frac{\varepsilon_\mathrm{T} - \varepsilon_\mathrm{S}}{2\hbar^2}\mathbf{S}^2 \tag{2.21}$$

$$= \varepsilon_\mathrm{S} + \frac{\varepsilon_\mathrm{T} - \varepsilon_\mathrm{S}}{2\hbar^2}(\mathbf{S}_1^2 + \mathbf{S}_2 + 2\mathbf{S}_1 \cdot \mathbf{S}_2)$$

$$= \frac{3\varepsilon_\mathrm{T} + \varepsilon_\mathrm{S}}{4} + \frac{\varepsilon_\mathrm{T} - \varepsilon_\mathrm{S}}{\hbar^2}\mathbf{S}_1 \cdot \mathbf{S}_2 \tag{2.22}$$

where we have used the fact that electrons have spin quantum numbers $s_1 = s_2 = \frac{1}{2}$.

Aside from the constant energy level term in Eq. (2.22), we see that the interesting physics stemming from the direct exchange is contained within the spin–spin interaction term. This term is the exchange Hamiltonian of the system, and is usually written as

$$\mathcal{H}_\mathrm{ex} = -J\mathbf{S}_1 \cdot \mathbf{S}_2, \tag{2.23}$$

where $J > 0$ favors parallel alignment of the two electron spins, while $J < 0$ favors antialigned spins. J depend on the interaction Hamiltonian, $\mathcal{H}_{\text{int}}$ and the overlap and specific details of the atomic orbitals contained in φ_1 and φ_2.

Extending this to a many-body system with more than two electrons and atomic nuclei is highly non-trivial. Nevertheless, the Heisenberg Hamiltonian[37],

$$\mathcal{H} = -\frac{1}{2}\sum_{i,j} J_{i,j}\mathbf{S}_i \cdot \mathbf{S}_j\,, \tag{2.24}$$

which sums doubly over all possible electron spin pairs, gives good insight into how magnetic order can be achieved in a bulk material. Further details on the extension from the simple two-atom system to a general many-body system is beyond the scope of this thesis. However, it should be noted that in many materials the direct exchange mechanism in Eqs. (2.23) and (2.24) is not enough to explain the magnetic order alone. For the metallic transition elements like Fe, Ni, Co, the Stoner band model is usually employed for the intinerant electrons. The density of states for spin up and spin down species electrons is shifted with respect to one another.[35] In other crystaline materials, indirect exchange effects can also be responsible, of which the most prominent examples are:

- The *Ruderman–Kittel–Kasuya–Yosida* (RKKY) interaction, which occurs in metallic systems where the conduction electrons become spin polarized through the dipole–dipole interaction at one location and carries net angular momentum to another distant site.[38;39]

- The double exchange interaction, where intermediate non-magnetic atoms or ions, effectively transmit a spin from one higher valency ion to another smaller valency ion of the same element.[40]

- The Superexchange interaction, which is similar to the double exchange, but where the ions on either side of the non-magnetic ion have the same valency.[41–44] This result in antiferromagnetic coupling of the spins across the mediating ion.

The ferromagnetic insulator Yttrium-Iron-Garnet

As mentioned in Chapter 1, the ferromagnetic insulator that is most often used in magnonics is Yttrium-Iron-Garnet (YIG), $Y_3Fe_2(FeO_4)_3$. YIG is a complicated synthetic crystal with 160 atoms per unit cell (24 Y, 16+24 Fe and 96 O), where Fe^{3+} ions occupy two different coordination sites; 16 in octahedral and 24 in tetrahedral sites.[45–48] Because the magnetic moment of YIG originates from the Fe^{3+} ions we need to know the ground state of the ions. Fe^{3+} ions have a structure close to that of Fe; the first two electrons are removed from the orbitals with the highest quantum number n, i.e. the 4s orbitals, and the third electron is taken from a 3d orbital. The ground state is altered slightly from the case of Fe^{2+} ions shown above to ${}^6S_{5/2}$. The Fe^{3+} ions on different coordination sites couple through the superexchange interaction, meaning that the spins in the two coordination sites antialign to one another. What is important here is that for every two ions in the octahedral site there are three ions on tetrahedral coordination sites with antialigned spins. Thus the theoretically expected magnetic moment per unit cell of YIG should be equal to eight Fe^{3+} ions, which due to the ground state being an S-state ($L = 0$) the dipole moment is given from the total spin $J = S_{\text{tot}} = 5/2$. Using Eq. (2.11), we find $\mu_{\text{YIG}} = 8 \cdot 5\mu_B = 40\mu_B$, i.e. the dipole moment per unit cell, where we have used $g_S = 2$.[49] Because of the finite magnetic moment of the YIG unit cell, and the localized magnetic moments, it is usually modelled as a ferromagnet with cubic symmetry.

2.5 Precessional Motion and the Landau-Lifshitz-Gilbert Equation

Consider the classical model of a charged object having angular momentum $\mathbf{J}$. Using Eq. (2.5) and the classical analogue to Eq. (2.13), $\boldsymbol{\mu}_J = -\gamma_J \mathbf{J}$, we find the equation of motion to be

$$\frac{d\mathbf{J}}{dt} = -\gamma_J \mathbf{J} \times \mathbf{B}, \tag{2.25}$$

which describes right-handed precessional motion around the axis of $\mathbf{B}$.

Now, consider a magnetic moment originating from spin angular momentum alone, e.g. from atomic moments where the electrons in the atomic orbitals organize into a state with total orbital momentum equal to zero. If this moment is subjected to a free magnetic field, **H**. The *Zeeman energy* gives us the Hamiltonian

$$\mathcal{H} = -\boldsymbol{\mu} \cdot \mathbf{H} = \gamma \mathbf{S} \cdot \mathbf{H}, \tag{2.26}$$

where Eq. (2.11) was used to express the dipole moment using the spin observable, **S**. Efhrenfest's theorem states that the time derivative of the expectation value of a quantum mechanical operator $\mathcal{O}$ is given by

$$\frac{d\langle \mathcal{O} \rangle}{dt} = \left\langle \frac{\partial \mathcal{O}}{\partial t} \right\rangle + \frac{i}{\hbar} \langle [\mathcal{H}, \mathcal{O}] \rangle. \tag{2.27}$$

Assuming the moment is in a steady state, $\langle \partial \mathbf{S} / \partial t \rangle = 0$, we find

$$\begin{aligned} \frac{d\langle \mathbf{S} \rangle}{dt} &= \frac{i}{\hbar} \langle [\gamma \mathbf{S} \cdot \mathbf{H}, \mathbf{S}] \rangle. \\ &= -\gamma \langle \mathbf{S} \rangle \times \mathbf{H}, \end{aligned} \tag{2.28}$$

where Eq. (2.10) was used to write out and simplify the commutator. We see that Ehrenfest's theorem maintains that the expectation value of our quantum mechanical observable, **S**, obeys the same equation as the classical system in Eq. (2.25).

If we take the leap and imagine several spins exchange coupled in a volume, we can define our magnetization to be $\mathbf{M} = -\gamma \sum_i \langle \mathbf{S}_i \rangle / \mathcal{V}$, where $\mathcal{V}$ is the volume of the distribution of moments, the dynamics of the expectation value of **S** in Eq. (2.28) now becomes the *equation of motion* (EOM) for the bulk magnetization,

$$\frac{d\mathbf{M}}{dt} = -\gamma \mathbf{M} \times \mathbf{H}. \tag{2.29}$$

This equation implies that $\partial_t(\mathbf{M} \cdot \mathbf{H}) = 0$ as well as $\partial_t \mathbf{M}^2 = 0$, meaning that the magnetization precesses around the **H** field with constant angle and constant length (see Figure 2.1).

In a real crystal, the magnetization will interact with the lattice vibrations in the crystal structure, resulting in a dissipation channel. One of

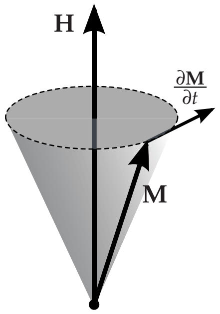

Figure 2.1: The magnetization **M** precesses around the **H** field.

the ways of modelling and adding such dissipation to Eq. (2.29) is by ensuring that the magnetization will approach **H** over time. This is exactly what Landau and Lifshitz[50] did by adding the term $\frac{\lambda}{M_s^2}(\mathbf{H} - (\mathbf{H} \cdot \mathbf{M})\mathbf{M})$ that points from **M** to **H** to the EOM, where λ is the LL damping parameter and M_s is the saturation magnetization. Using the vector triple product identity the damping term is cast into a more modern format and the EOM becomes

$$\frac{d\mathbf{M}}{dt} = -\gamma \mathbf{M} \times \mathbf{H} - \frac{\lambda}{M_s^2} \mathbf{M} \times (\mathbf{M} \times \mathbf{H}). \tag{2.30}$$

This equation is known as the *Landau–Lifshitz* (LL) equation.

A more rigorous approach was later employed by Gilbert[51] [52] who added a Rayleigh dissipation term to the Lagrange equations describing Eq. (2.29). He showed that such a term would renormalize the **H** field in the EOM,

$$\mathbf{H} \rightarrow \mathbf{H} - \frac{\alpha}{\gamma M_s} \frac{d\mathbf{M}}{dt}, \tag{2.31}$$

where α is the dimensionless Gilbert damping parameter. α is a material dependent relaxation parameter, usually in the order of $\alpha \sim 10^{-2}$ for metallic ferromagnets, while being exceptionally small in YIG, $\alpha_{\mathrm{YIG}} \approx 3 \cdot 10^{-4}$.

Inserting Eq. (2.31) into Eq. (2.29) gives us the *Landau–Lifshitz–Gilbert* (LLG) equation

$$\frac{d\mathbf{M}}{dt} = -\gamma \mathbf{M} \times \mathbf{H} + \frac{\alpha}{M_s} \mathbf{M} \times \frac{d\mathbf{M}}{dt}, \tag{2.32}$$

which describes damped precessional motion around the field, as shown in Figure 2.2.

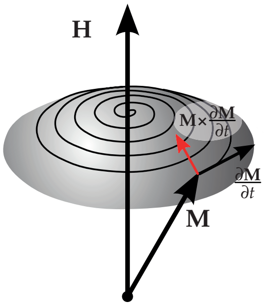

Figure 2.2: The magnetization **M** precesses around the effective field $\mathbf{H}_{\text{eff}}$ as described by the LLG equation. The magnetization spirals in towards the equilibrium direction of the **H** field, keeping $\partial_t \mathbf{M}^2 = 0$.

Extending Eq. (2.8) to a system where the total free energy of the system contains other terms besides the potential energy term in Eq. (2.6) that depend on the magnetization, gives us a definition of the effective field that is seen by the magnetization

$$\mathbf{H}_{\text{eff}} = -\frac{\delta F[\mathbf{M}]}{\delta \mathbf{M}}, \tag{2.33}$$

In a ferromagnetic system, typical contributions to the magnetization dependent part of the free energy are

$$F[\mathbf{M}] = \int_{\mathcal{V}} (f_d(\mathbf{M}) + f_{\text{ex}}(\mathbf{M}) + f_{\text{dip}}(\mathbf{M}) + f_a(\mathbf{M}))\, d\mathbf{r}, \tag{2.34}$$

where $f_d = -\mathbf{M}\cdot\mathbf{H}_e$ is the non-constant part of the Zeeman energy density (see Eq. (2.6) and Eq. (2.2)) from an externally applied field $\mathbf{H}_e$, f_a is the magnetocrystalline anisotropy energy density, f_{ex} is the exchange energy density, and f_{dip} is the self energy density due to dipole–dipole interactions within the ferromagnet.

Let us discuss these different energy contributions and calculate the corresponding contributions to the effective field.

2.5.1 Exchange Energy

The exchange energy between spins in a periodic crystal structure is given by the Heisenberg Hamiltonian of Eq. (2.24), which can be rewritten to the form $\mathcal{H}_{\mathrm{ex}} = \sum_i F_{\mathrm{ex},i}$ where

$$F_{\mathrm{ex},i} = -\mathbf{S}_i \cdot \sum_{\langle j \rangle} \frac{1}{2} J_{ij} \mathbf{S}_j, \tag{2.35}$$

is the exchange energy felt by one spin on site i due to the spins on sites j, and J_{ij} is the exchange coupling strength. Here, $\langle j \rangle$ indicates that we have limited the sum over j to be a summation over only the nearest neighbors for each site i. Using Eq. (2.11) we find that

$$F_{\mathrm{ex},i} = -\boldsymbol{\mu}_i \cdot \mathbf{B}_{\mathrm{ex}}, \quad \mathbf{B}_{\mathrm{ex}} = \frac{1}{2\gamma^2} \sum_{\langle j \rangle} J_{ij} \boldsymbol{\mu}_j \tag{2.36}$$

where B_{ex} is the effective exchange field due to all the neighboring spins j, which is the same for all sites i given that $J_{ij} = J$.

Because the exchange interaction works to align the neighbouring spins, in the continuum limit each $\boldsymbol{\mu}_j$ in $\mathbf{B}_{\mathrm{ex}}$ can be considered part of a slowly varying semiclassical vector field, $\boldsymbol{\mu}_j = \boldsymbol{\mu}(\mathbf{r}_j)$. The sum over all the moments becomes $\sum_{\langle j \rangle} \boldsymbol{\mu}(\mathbf{r}_j) = \sum_{\langle j \rangle} \boldsymbol{\mu}(\mathbf{r}_i + \boldsymbol{\delta}_j)$, where $\boldsymbol{\delta}_j$ is the distance from a site i to the nearest spins at site j. Expanding this expression to 2nd order in $\boldsymbol{\delta}_j$, and summing over all the nearest neighbors, it can be shown that the exchange field is of the form[49]

$$\mathbf{B}_{\mathrm{ex}} = \frac{2A}{M_s^2} \nabla^2 \mathbf{M} + 4\pi \Lambda \mathbf{M}, \tag{2.37}$$

where A, with units $[A] = \mathrm{erg/cm}$, is known as the exchange stiffness, which depends on the crystal symmetry, exchange coupling strength, J and the g-factor through the gyromagnetic ratio γ. The second term is akin to the Weiss molecular field. The dimensionless constant Λ is left unspecified, as the second term in Eq. (2.37) will not contribute to the effective exchange field, $\mathbf{H}_{\mathrm{ex}}$, and it therefore does not affect the EOM. As the interspin distance is small, the total contribution to the free energy from the exchange interactions becomes

$$F_{\mathrm{ex}} = -\int_{\mathcal{V}} \mathbf{M} \cdot \mathbf{B}_{\mathrm{ex}} \, d\mathbf{r}, \tag{2.38}$$

and the effective field can be extracted by inserting Eq. (2.37) into Eq. (2.38) and comparing with Eqs. (2.6) and (2.8), or formally by taking the functional derivative of Eq. (2.38) with respect to **M**. Either way, the exchange field contribution to the effective field is

$$\mathbf{H}_{\text{ex}} = \frac{2A}{M_s^2}\nabla^2\mathbf{M}. \tag{2.39}$$

The free energy contribution from the exchange field is usually written in another form;[50] performing integration by parts on Eq. (2.38) over the total volume $\mathcal{V}$, we get

$$F_{\text{ex}} = \int_{\mathcal{V}} \frac{A}{M_s^2}\sum_k (\nabla M_k(\mathbf{r}))^2\, d\mathbf{r}, \tag{2.40}$$

where the summation is over the 3 cartesian components, and where we have omitted writing out the boundary terms as they don't contribute to the effective field. To minimize the exchange energy, the curvature of the semiclassical field must be minimized. Excitations above the perfectly parallel ground state must therefore be small local deviations from equilibrium, or a spin wave if you will (see Figure 2.3 for an illustration).

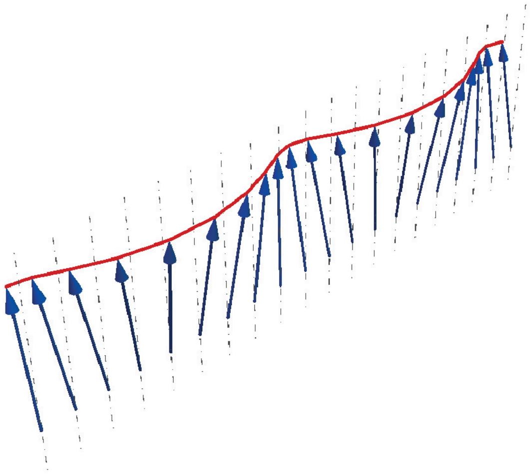

Figure 2.3: A spin wave propagating through a chain of spins.

2.5.2 The dipole–dipole Self Energy

The self energy is a direct result of Maxwell's equations and the dipole–dipole interactions. The magnetic field emanating from a magnetic dipole was given in Eq. (2.7). In the continuum limit, the magnetization in a ferromagnet is a semiclassical vector field, $\mathbf{M} = \mathbf{M}(\mathbf{r})$, and the total self energy of the magnetization due to nonlocal dipole–dipole interactions becomes

$$F_{\text{dip}} = -\iint_{\mathcal{V}} \Big[\frac{3(\mathbf{M}(\mathbf{r}) \cdot (\mathbf{r} - \mathbf{r}'))(\mathbf{M}(\mathbf{r}') \cdot (\mathbf{r}' - \mathbf{r}))}{|\mathbf{r} - \mathbf{r}'|^5} - \frac{\mathbf{M}(\mathbf{r}) \cdot \mathbf{M}(\mathbf{r}')}{|\mathbf{r} - \mathbf{r}'|^3}\Big]\, d\mathbf{r} d\mathbf{r}'. \tag{2.41}$$

Using Eq. (2.33), we find that the dipole-dipole field is given by

$$\mathbf{H}_{\text{dip}} = \int_{\mathcal{V}} \Big[3\frac{(\mathbf{M}(\mathbf{r}') \cdot (\mathbf{r} - \mathbf{r}'))(\mathbf{r}' - \mathbf{r})}{|\mathbf{r} - \mathbf{r}'|^5} - \frac{\mathbf{M}(\mathbf{r}')}{|\mathbf{r} - \mathbf{r}'|^3}\Big]\, d\mathbf{r}', \tag{2.42}$$

which in general can be compactly written as

$$\mathbf{H}_{\text{dip}} = 4\pi \int_{\mathcal{V}} \widehat{G}(\mathbf{r} - \mathbf{r}')\mathbf{M}(\mathbf{r}')\, d\mathbf{r}', \tag{2.43}$$

where $\widehat{G}$ is the 2nd rank dipole–dipole tensorial Green's function.[53–55] I leave the tensor unspecified for now, but will come back to it in the next chapter.

2.5.3 Magnetocrystaline Anisotropy Energy

The magnetocroystaline anisotropy depends on the crystal symmetry, and is often written out in power series of direction cosines wrt. the symmetry axes.[56] In YIG, the magnetocrystaline anisotropy energy is negligible, specifically if the crystal is grown along the 111 crystal direction[57]. For completeness sake I list the simplest anisotropies that are occur in the literature:

$$f_{a,\text{UD}} = \frac{K_{\text{UD}}}{2}\left(1 - \frac{\mathbf{M} \cdot \hat{\mathbf{e}}_d}{M_s}\right), \tag{2.44}$$

$$f_{a,\text{UA}} = K_{\text{UA}}\left(1 - \frac{(\mathbf{M} \cdot \hat{\mathbf{e}}_e)^2}{M_s^2}\right) \tag{2.45}$$

where $f_{a,\mathrm{UD}}$ expresses unidirectional anisotropy with preferred direction along $\hat{\mathbf{e}}_d$, while $f_{a,\mathrm{UA}}$ is uniaxial anisotropy with an easy axis along $\hat{\mathbf{e}}_e$. Letting $K_{\mathrm{UA}} < 0$ changes $\hat{\mathbf{e}}_e$ into a hard axis, giving easy plane anisotropy (except for an energy shift).

2.5.4 Maxwell's Equations in The Magnetostatic approximation

Solving the LLG equation in an infinite ferromagnet in the presence of an external field and neglecting the Gilbert damping term, any anisotropies and the exchange interaction, we expect the magnetization to precess around the magnetic field. Hence we write the magnetization in the ferromagnet as $\mathbf{M} = \mathbf{M}_s + \mathbf{m}$ and assume that the $\mathbf{H}$ field will be similar of a similar form, $\mathbf{H} = \mathbf{H}_e + \mathbf{h}$. Here, $\mathbf{M}_s || \mathbf{H}_e$, and $\mathbf{m} = \mathbf{m}(t)$ describes the precession around the static external field $\mathbf{H}_e$. $\mathbf{h} = \mathbf{h}(t)$ results from $\mathbf{m}$ and is the dynamic field due to dipole–dipole interactions in the ferromagnet.

Assuming that $\mathbf{m}$ can be described by a plane wave, $\mathbf{m} \propto e^{i(\omega t - \mathbf{k}\cdot\mathbf{r})}$, and that $|\mathbf{m}| \ll M_s$, we linearize the LLG equation in the dynamic fields, finding

$$- i\omega\mathbf{m} = -\gamma\hat{\mathbf{z}} \times (M_s\mathbf{h} - H_e\mathbf{m}), \tag{2.46}$$

where $\hat{\mathbf{z}} = \mathbf{H}_e/H_e$ is the direction of the static field. Solving this equation for the small signal dynamic field $\mathbf{m}$ it is trivial to show that $\mathbf{m} \propto \mathbf{h}$, meaning that the total field can be written as $\mathbf{M} = \widehat{\chi} \cdot \mathbf{H}$, with the susceptibility tensor given by

$$\widehat{\chi} = \begin{pmatrix} \frac{\omega_H\omega_M}{4\pi(\omega_H^2 - \omega^2)} & \frac{i\omega\omega_M}{4\pi(\omega_H^2 - \omega^2)} & 0 \\ \frac{-i\omega\omega_M}{4\pi(\omega_H^2 - \omega^2)} & \frac{\omega_H\omega_M}{4\pi(\omega_H^2 - \omega^2)} & 0 \\ 0 & 0 & 1 \end{pmatrix}, \tag{2.47}$$

where $\omega_M = 4\pi\gamma M_s$ and $\omega_H = \gamma H_e$. The denominator, $\omega_H^2 - \omega^2$ is the resonance condition of the ferromagnet. This result is the basis for the experimental technique *ferromagnetic resonance* where a ferromagnetic sample is placed inside a resonance cavity and driven into precession around an externally applied field by tuning of the external field strength.

With the plane wave ansatz above, the susceptibility from Eq. (2.47), assuming no free currents (because we are dealing with a ferromagnetic insulator) and assuming isotropic permittivity $\mathbf{D} = \varepsilon\mathbf{E}$, the Fourier transformed version of Maxwell's equations, lead to wave equations for the $\mathbf{H}$ and $\mathbf{E}$ fields in the fourier components $\mathbf{k}$. It is outside the scope of this thesis to calculate and list all the bulk solutions, but it can be shown[49] that the wave number k must fulfill certain conditions depending on the relative orientation of $\mathbf{k}$ with respect to the equilibrium direction of the externally applied field. For the two limiting geometries of $\mathbf{k} \parallel \mathbf{H}_e$ and $\mathbf{k} \perp \mathbf{H}_e$, each dispersion relation $\omega = \omega(k)$ splits into two branches; one that is asymtotically linear in k and one that converges to a constant.

Because the linearly assymptotic branch has a much higher frequency, and hence a higher excitation energy, than the other branch as k grows, certain simplifications can be made. From the Fourier transformed version of Maxwell's equations it can be shown that for the branch with lowest energy $\mathbf{E}(k) \sim k^{-2}$ as k grows, thus going quickly to zero. With this observation, we know that we only need to solve Maxwell's equations with $\mathbf{E} = 0$ if we are only interested in the dispersion that is the lowest in energy. In this limit, Maxwell's equations simplifies to

$$\nabla \cdot (\mathbf{H} + 4\pi\mathbf{M}) = 0, \qquad \nabla \times \mathbf{H} = 0, \tag{2.48}$$

which is known as the *magnetostatic approximation*.

With all the fundamental bulk properties now in place, the following chapter turns our attention to what changes need to be made when translational symmetry is broken, i.e. when we introduce interfaces and surfaces into the system.

3 Spin Waves in Thin-film Structures

When moving from a bulk ferromagnetic system into a thin-film ferromagnetic structure certain finite size effects appear. In this chapter I will discuss how the finite transverse size of the thin film changes the equations set to be solved. An important part of this is how the dipole–dipole tensor introduced in Sec. 2.5.2 is calculated for a thin film in the magnetostatic approximation (see Sec. 2.5.4).

When introducing interfaces for a precessing ferromagnet the LLG equation itself demands that certain boundary conditions are fulfilled. This amounts to conservation of spin angular momentum at the interfaces. Because of this, the spintronic interface effects of spin pumping and spin transfer torque starts to affect the dynamics of the ferromagnet. After having dealt with the dipole–dipole tensor, these interface torques will be explored and finally the appropriate boundary conditions will be determined.

3.1 Thin film magnetization dynamics

In Chapter 2.5 we found the equation of motion for a magnetization in a bulk ferromagnet. Let us now focus on what happens if we break translational symmetry in one direction. Consider an insulating ferromagnetic thin-film of thickness L, where by "thin" we mean the order of μm and smaller.

The natural coordinate system of the film (see Figure 3.1) is chosen to be such that $\hat{\boldsymbol{\xi}}$ is the film's outward normal while $\hat{\boldsymbol{\eta}}$ and $\hat{\boldsymbol{\zeta}}$ define the plane of the film. $\xi\eta\zeta$ form a right handed coordinate system. We take the origin to be in the middle of the film, and choose $\xi = -L/2$ to be the location of the substrate interface, while $\xi = L/2$ is the location of the normal metal interface. Let us further set the thickness of the normal metal capping layer to be d thick.

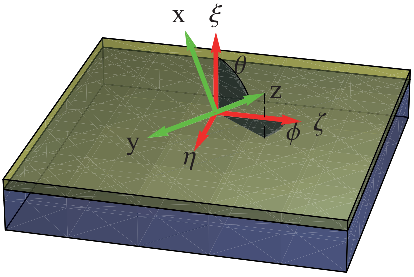

Figure 3.1: An illustration of a thin NM layer (in yellow) stacked on top of an FI film (in blue), where the natural coordinate axes of the stack geometry is overlayed on top. Here $\hat{\boldsymbol{\xi}}$ is the film normal, while $\hat{\mathbf{z}}$ is the internal field axis. $\hat{\mathbf{y}}$ is always kept in-plane, regardless of the value of θ, while $\hat{\mathbf{x}}$ tilts out-of-plane when $\theta \neq 0$.

Let us apply an external magnetic field, forming an angle θ_e with the film normal $\hat{\boldsymbol{\xi}}$ and a projected angle φ with the in plane ζ axis. It is then parametrized by the two angles as

$$\mathbf{H}_e = H_e(\cos\theta_e\hat{\boldsymbol{\xi}} + \sin\theta_e\cos\varphi\hat{\boldsymbol{\zeta}} + \sin\theta_e\sin\varphi\hat{\boldsymbol{\eta}}). \tag{3.1}$$

Assuming that the external field is strong, such that the magnetization, $\mathbf{M} = \mathbf{M}(\mathbf{r}, t)$ in the continuum limit, is close to saturation. Hence,

$$\mathbf{M}(\mathbf{r}, t) = \mathbf{M}_s + \mathbf{m}(\mathbf{r}, t), \tag{3.2}$$

where $\mathbf{m} \cdot \mathbf{M}_s \equiv 0$, and where we have $|\mathbf{m}| \ll M_s$.

The logical question to ask next is: in which direction does the static magnetization, $\mathbf{M}_s$, point? Through the dipole–dipole interactions the external field will induce a static demagnetization field in the ferromagnet. Let $\mathbf{H}_i = H_i\hat{\mathbf{z}}$, with $H_i > 0$, be the field inside the ferromagnet, and assume that it forms an angle θ with the $\hat{\boldsymbol{\xi}}$ axis. The boundary conditions required by Maxwell's equations (see Eq. (2.9)) gives[54]

$$H_e \cos\theta_e = (H_i + 4\pi M_s)\cos\theta, \tag{3.3a}$$

$$H_e \sin\theta_e = H_i \sin\theta. \tag{3.3b}$$

Hence, for $\theta_e = \pi/2$ (in-plane applied external field), $H_i = H_e$ and $\theta = \theta_e$, meaning that there is no shape anisotropy in this geometry. For $\theta_e = 0$ (perpendicularly applied external field) $\theta = \arccos(H_e/(4\pi M_s))$ when $H_e < 4\pi M_s$ and $\theta = 0$ otherwise. Ensuring that the applied field is large enough so that we get the latter case, we find that $H_i = H_e - 4\pi M_s$. For the general case of intermediate angles, $\theta_e \in (0, \pi/2)$, the internal field forms an angle $\theta > \theta_e$ with the film normal, and both the direction and angle must be calculated from the equations above.

The dynamic magnetization component $\mathbf{m}(\mathbf{r}, t)$ is in the transverse xy plane. As can be seen in Figure 3.1, we keep the y axis confined to the $\eta\zeta$ plane. For $\theta = \varphi = 0$ the directions are $\hat{\mathbf{y}} = \hat{\boldsymbol{\eta}}$ and $\hat{\mathbf{x}} = -\hat{\boldsymbol{\zeta}}$; for $\theta = \pi/2$ we have $\hat{\mathbf{x}} = \hat{\boldsymbol{\xi}}$ while $\hat{\mathbf{y}} = \hat{\boldsymbol{\eta}}$ for $\varphi = 0$ or $\hat{\mathbf{y}} = -\hat{\boldsymbol{\zeta}}$ for $\varphi = \pi/2$.[1] The transformation between the two coordinate systems is found in Appendix A.

3.1.1 In-plane Spin Waves in the Linear Response Regime

Let us refine our assumption about the dynamic magnetization $\mathbf{m}$ from Eq. (3.2) to include a plane wave moving along the $\hat{\boldsymbol{\zeta}}$ direction,

$$\mathbf{m}(\mathbf{r}, t) = \mathbf{m}_Q(\xi) \cdot e^{i(\omega t - Q\zeta)}. \tag{3.4}$$

where Q is the in-plane wave number, ω is the frequency of the wave, and $\mathbf{m}_Q$ is independent of ζ and t. The vector part can be written as

$$\mathbf{m}_Q(\xi) = X_Q(\xi)\hat{\mathbf{x}} + Y_Q(\xi)\hat{\mathbf{y}}, \tag{3.5}$$

where X_Q and Y_Q are related to one another through the LLG equation throughout the bulk material, and through appropriate boundary conditions at any interfaces.

---

[1] Kalinikos' choice of axes labels is a bit untraditional and hard to grasp at first. The power comes from not having to deal with the confusion that often occurs when different authors use both marked, x'y'z', and unmarked coordinate systems, xyz, and the choice of the axes in relation to the film changes between every journal article on the topic.

3.1.2 The Dynamic Demagnetization Field

As we have already accounted for the static demagnetization field by embedding it in the internal field, we need only focus on the shape of the dynamic field stemming from the dipole–dipole interaction (see 2.5.2). The general form of the effective field contribution from this interaction was given in Eq. (2.42). This result can be refined by taking the thin-film geometry into account as well as the simplifications of Maxwell's equations in the magnetostatic approximation (see 2.5.4. We follow the approach of Kalinikos[53 54], and assume that the induced field is of the same shape as $\mathbf{m}$, $\mathbf{h}_d(\mathbf{r}, t) = \mathbf{h}_Q(\xi) \cdot e^{i(\omega t - Q\zeta)}$, Maxwell's equations give

$$\nabla \cdot (\mathbf{h}_d + 4\pi \mathbf{m}) = 0, \qquad \nabla \times \mathbf{h}_d = 0, \quad \text{(inside)} \tag{3.6a}$$

$$\nabla \cdot \mathbf{h}_d = 0, \qquad \nabla \times \mathbf{h}_d = 0. \quad \text{(outside)} \tag{3.6b}$$

Because the field in Eq. (2.7) goes quickly to zero when moving away from a dipole, the dipole–dipole effective field must also decay away from the ferromagnetic film. Thus, $\lim_{\xi \to \pm\infty} \mathbf{h}_d = 0$.

Writing $\mathbf{m}$ and $\mathbf{h}_d$ in the $\xi\eta\zeta$ coordinate basis, Eq. (3.6) leads to the set of coupled differential equations

$$h_{Q,\eta} = 0, \tag{3.7a}$$

$$h_{Q,\xi} = \frac{i}{Q}\frac{dh_{Q,\zeta}}{d\xi}, \tag{3.7b}$$

$$\frac{dh_{Q,\xi}}{d\xi} - iQh_{Q,\zeta} = 4\pi \left(iQm_{Q,\zeta} - \frac{dm_{Q,\xi}}{d\xi} \right), \tag{3.7c}$$

where the first equation is obvious when considering the translational symmetry along the η-axis. Eliminating $h_{Q,\xi}$ from Eq. (3.7c) using Eq. (3.7b) gives a second order differential equation for $h_{Q,\zeta}$ that is readily solved by the use of Green's functions. Similar to Eq. (2.43), the result can be summarized as

$$\mathbf{h}_{Q,\xi\eta\zeta}(\xi) = 4\pi \int_{-\infty}^{\infty} \widehat{\mathcal{G}}(\xi - \xi') \cdot \mathbf{m}_{Q,\xi\eta\zeta}(\xi')\, d\xi', \tag{3.8}$$

where the 2nd rank tensor $\widehat{\mathcal{G}}$ is given by

$$\widehat{\mathcal{G}}(\xi - \xi') = \begin{bmatrix} G^P(\xi - \xi') - \delta(\xi - \xi') & 0 & -iG^Q(\xi - \xi') \\ 0 & 0 & 0 \\ -iG^Q(\xi - \xi') & 0 & -G^P(\xi - \xi') \end{bmatrix}. \tag{3.9}$$

with the functions G^P and G^Q are given by

$$\begin{aligned} G^P(\xi-\xi') =& \frac{Q}{2} e^{-Q|\xi-\xi'|}, && (3.10a) \\ G^Q(\xi-\xi') =& \mathrm{sgn}(\xi-\xi') \cdot G^P(\xi-\xi'). && (3.10b) \end{aligned}$$

The dipole-dipole field can be transformed into the xyz-coordinate system by using the rotation matrix from Eq. A.4

$$\begin{aligned} \mathbf{h}_Q(\xi) =& \mathbf{T} \cdot \mathbf{h}_{Q,\xi\eta\zeta}(\xi) && (3.11) \\ =& 4\pi \int_{-\infty}^{\infty} d\xi' \, \mathbf{T} \cdot \widehat{\mathcal{G}}(\xi-\xi') \cdot \mathbf{T}^{-1} \mathbf{T} \cdot \mathbf{m}_{Q,\xi\eta\zeta}(\xi') && (3.12) \\ =& 4\pi \int_{-\infty}^{\infty} d\xi' \, \widehat{\mathcal{G}}^{(xyz)}(\xi-\xi') \cdot \mathbf{m}_Q(\xi'), && (3.13) \end{aligned}$$

where the transformed $\mathcal{G}$-tensor is given by

$$\begin{aligned} \widehat{\mathcal{G}}^{(xyz)} =& \mathbf{T} \cdot \widehat{\mathcal{G}} \cdot \mathbf{T}^{-1} = \mathbf{T} \cdot \widehat{\mathcal{G}} \cdot \mathbf{T}^{T} \\ \widehat{\mathcal{G}}^{(xyz)} =& \begin{bmatrix} s_\theta^2 \mathcal{G}_{\xi\xi} - c_\varphi s_{2\theta} \mathcal{G}_{\xi\zeta} + c_\theta^2 c_\varphi^2 \mathcal{G}_{\zeta\zeta} & -s_\varphi s_\theta \mathcal{G}_{\xi\zeta} + s_\varphi c_\varphi c_\theta \mathcal{G}_{\zeta\zeta} & s_\theta c_\theta \mathcal{G}_{\xi\xi} - s_\theta c_\theta c_\varphi^2 \mathcal{G}_{\zeta\zeta} + c_\varphi \left(s_\theta^2 - c_\theta^2\right) \mathcal{G}_{\xi\zeta} \\ -s_\varphi s_\theta \mathcal{G}_{\xi\zeta} + s_\varphi c_\varphi c_\theta \mathcal{G}_{\zeta\zeta} & s_\varphi^2 \mathcal{G}_{\zeta\zeta} & -s_\varphi c_\theta \mathcal{G}_{\xi\zeta} - s_\varphi s_\theta c_\varphi \mathcal{G}_{\zeta\zeta} \\ s_\theta c_\theta \mathcal{G}_{\xi\xi} - s_\theta c_\theta c_\varphi^2 \mathcal{G}_{\zeta\zeta} + c_\varphi \left(s_\theta^2 - c_\theta^2\right) \mathcal{G}_{\xi\zeta} & -s_\varphi c_\theta \mathcal{G}_{\xi\zeta} - s_\varphi s_\theta c_\varphi \mathcal{G}_{\zeta\zeta} & c_\theta^2 \mathcal{G}_{\xi\xi} + s_{2\theta} c_\varphi \mathcal{G}_{\xi\zeta} + c_\varphi^2 s_\theta^2 \mathcal{G}_{\zeta\zeta} \end{bmatrix} && (3.14) \end{aligned}$$

where I have used the notation $s_x = \sin(x)$ and $c_x = \cos(x)$. Because $\widehat{\mathcal{G}}$ is a symmetric tensor and **T** is an affine transformation we see that $\widehat{\mathcal{G}}^{(xyz)}$ is also symmetric. Because **m** is limited to the xy plane in the linear response regime, only the upper left 2x2 part of the tensor in Eq. (3.14), given by

$$\begin{aligned} \widehat{\mathcal{G}}^{(xy)} =& \begin{pmatrix} \mathcal{G}_{xx}^{(xyz)} & \mathcal{G}_{xy}^{(xyz)} \\ \mathcal{G}_{yx}^{(xyz)} & \mathcal{G}_{yy}^{(xyz)} \end{pmatrix} \\ =& \begin{pmatrix} s_\theta^2 \mathcal{G}_{\xi\xi} - c_\varphi s_{2\theta} \mathcal{G}_{\xi\zeta} + c_\theta^2 c_\varphi^2 \mathcal{G}_{\zeta\zeta} & -s_\varphi s_\theta \mathcal{G}_{\xi\zeta} + s_\varphi c_\varphi c_\theta \mathcal{G}_{\zeta\zeta} \\ -s_\varphi s_\theta \mathcal{G}_{\xi\zeta} + s_\varphi c_\varphi c_\theta \mathcal{G}_{\zeta\zeta} & s_\varphi^2 \mathcal{G}_{\zeta\zeta} \end{pmatrix}, && (3.15) \end{aligned}$$

will enter into a linearized equation of motion.

Spin Wave Dynamics in Different Field Geometries

Taking the directional dependence of the dipole–dipole tensor in Eq. (3.15) into account, it is not surprising that the magnetization dynamics in a thin-film ferromagnet is strongly dependent on the relative orientation of the internal field $\mathbf{H}_i$ with respect to the in-plane wave propagation direction $\hat{\zeta}$. The three main geometries consists of the $\theta = 0$ geometry and the two in-plane ($\theta = \pi/2$) geometries where $\varphi = 0$ or $\varphi = \pi/2$ (see Figure 3.2).[54;58–63]

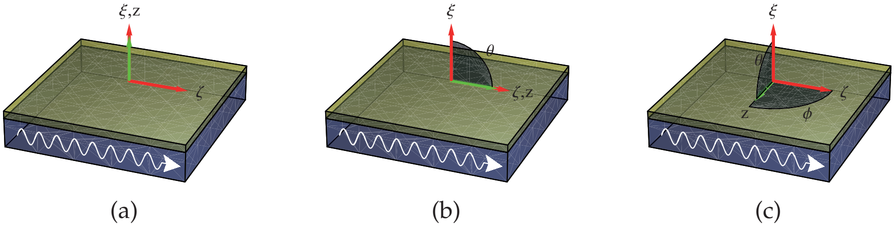

(a) (b) (c)

Figure 3.2: Internal field direction, $\hat{\mathbf{z}}$ (green arrow), in relation to the wave propagation direction $\hat{\zeta}$ and the film normal $\hat{\xi}$. The three limiting geometries are: a) $\theta = 0$; b) $\theta = \pi/2$ and $\varphi = 0$; c) $\theta = \varphi = \pi/2$.

Traditionally, these spin wave classes are characterized by the appearance of the transverse mode profiles $\mathbf{m}_Q = \mathbf{m}_Q(\xi)$ and the characteristics of the group velocity, $v_g = \partial\omega(Q)/\partial Q$, calculated from the dispersion relations. *Volume modes* are modes where $\mathbf{m}_Q(\xi)$ is spatially distributed across the entire film, while *surface modes* are modes that are localized near a film interface. *Forward* modes have positive group velocity, and *backward* modes have negative group velocity for some values of QL. Combining these traits, we arrive at the naming of the common mode geometries:

- *Forward Volume Magnetostatic Waves* (FVMSWs) appear in the perpendicular ($\theta = 0$) geometry (see Figure 3.2a).

- *Backward Volume Magnetostatic Waves* (BVMSWs) appear in the in-plane ($\theta = \pi/2$) collinear ($\varphi = 0$) geometry (see Figure 3.2b).

- *Magnetostatic Surface Waves* (MSSWs) appear in the in-plane ($\theta = \pi/2$) transverse ($\varphi = \pi/2$) geometry (see Figure 3.2c).

3.2 Interface Effects

As described in the introduction (see Sec. 1.2), when a ferromagnet is put in contact with a normal metal, angular momentum can be transferred too and from the ferromagnet. These interface effects then appear on the right hand side of the LLG equation (see Eq. (2.32)) as additional interface localized torques.

3.2.1 Spin Accumulations and Spin Transfer Torque

A build up of a non-equilibrium *spin accumulation* in the ferromagnet's adjoining normal metal can transfer angular momentum into the ferromagnet. The mechanism for the generation of the spin accumulation can for instance be the *spin Hall effect*,[64–66] where spin–orbit interactions causes a spin imbalance to develop perpendicularly to the electron current direction.

As was done by Brataas et al.[20], let us define the spin accumulation to be half the difference in chemical potential for spin up and spin down electrons in the normal metal material.

$$\mu^{(s)} = \frac{1}{2}\left(\mu^{\uparrow} - \mu^{\downarrow}\right), \tag{3.16}$$

where the exponent '(s)' is to distinguish the spin accumulation from the total chemical potential. The spin polarization axis, $\hat{\mathbf{s}}$, is used to make the spin accumulation into a vector $\boldsymbol{\mu}^{(\mathbf{s})} \equiv \mu^{(s)}\hat{\mathbf{s}}$. In the same way that the local voltage is related to the potential energy, $eV^{(c)}$ ('c' is for charge), where e is the electron charge, we can define the voltage due to the spin accumulation to be $V^{(s)} \equiv \mu^{(s)}/e = (\mu^{\uparrow} - \mu^{\downarrow})/(2e)$. The electrical potential as seen by spin up or spin down electrons is then given by $V^{\uparrow} = V^{(c)} + V^{(s)}$ and $V^{\downarrow} = V^{(c)} - V^{(s)}$.

If a spin accumulation exists in a normal metal in contact with a ferromagnet, a spin current develops across the interface, which will excert a torque on the dynamic magnetization only if it is transverse to the magnetization. The transferred spin current can thus be decomposed into two transverse parts, and written as

$$\mathbf{I}^{\mathrm{stt}} = -\frac{\hbar}{2eM_s^2}\left[2G_\perp^{(R)}\mathbf{M}\times(\mathbf{M}\times(V^{(s)}\hat{\mathbf{s}})) + 2G_\perp^{(I)}(\mathbf{M}\times(V^{(s)}\hat{\mathbf{s}}))\right], \tag{3.17}$$

where $G_\perp^{(R)}$ and $G_\perp^{(I)}$ are the real and imaginary part of the spin *mixing conductance* that describes the coupling of the spins over the interface.[23;20] It has been found that $G_\perp^{(R)} \gg G_\perp^{(L)}$.[67] As such, the following only uses the real part, denoted as $G_\perp = G_\perp^{(R)}$.

Eq. (3.17) is basicly a conductance times a directional voltage (from the spin accumulation) converted from charge current to spin angular momentum current (spin current) by the factor $\hbar/2e$. Take notice of the prefactor 2 associated with the spin mixing conductance, which stems from the fact that the spin accumulation in Eq. (3.16) is defined as half the difference in chemical potential.

With the transferred spin current density

$$\mathbf{j}^{\mathrm{stt}} \triangleq \mathbf{I}^{\mathrm{stt}}/\mathcal{A} = -\frac{\hbar}{e^2M_s^2}g_\perp\mathbf{M}\times(\mathbf{M}\times\boldsymbol{\mu}^{(\mathbf{s})}), \tag{3.18}$$

where $\mathcal{A}$ is the interface area so that $g_\perp = G_\perp/\mathcal{A}$ is the spin mixing conductance per unit area, the torque on the magnetization in the ferromagnetic insulator due to the transferred spin current becomes

$$\boldsymbol{\tau}_{\mathrm{stt}} = \gamma\delta(\xi-\xi_i)\mathbf{j}^{\mathrm{stt}} = -\frac{\gamma\hbar}{e^2M_s^2}g_\perp\delta(\xi-\xi_i)\mathbf{M}\times\left(\mathbf{M}\times\boldsymbol{\mu}^{(\mathbf{s})}\right), \tag{3.19}$$

where ξ_i is the ξ coordinate of the spin active interface.

3.2.2 Spin Pumping

It was discovered[68–72] and later quantitatively explained[22–26] that if a dynamic ferromagnetic material is put in contact with a normal metal, the magnetization dynamics will exert a torque on the spins of electrons in the immediate vicinity of the magnet. In linear response, it can be shown that the spin pumping effect is the inverse of the spin transfer torque. These are related through what is known as the Onsager reciprocity relations.[20]

Both a scattering formalism and a dynamic magnetic susceptibility formalism can be used to describe the resulting pumped spin current.[73;74]

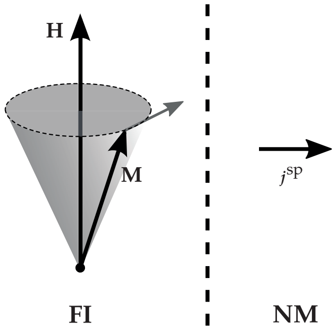

Figure 3.3: The precessing magnetization in the ferromagnetic insulator causes a spin current, $\mathbf{j}^{\text{sp}}$, to be injected into the normal att the interface.

These formalisms give the same result and are thus equivalent. As the electrons are carried away from the ferromagnet-normal metal interface, the electrons spin with respect to each other, causing them to dephase. This is seen as an overall loss of angular momentum from the ferromagnet, and we say that a spin current is pumped from the ferromagnet (see Figure 3.3). The spin current density is given by

$$\mathbf{j}^{\text{sp}} = \frac{\hbar^2}{2e^2 M_s^2} g_\perp \mathbf{M} \times \frac{\partial \mathbf{M}}{\partial t}, \tag{3.20}$$

This loss of angular momentum from the ferromagnet can be described as an extra dissipation torque acting on the magnetization. It is similar to the Gilbert term in the LLG equation (see Sec. 2.5), and is to be added to the right hand side of Eq. (2.32). The torque acting on the magnetization in a ferromagnetic insulator is due to the interfacial spin pumping, and is written as

$$\boldsymbol{\tau}_{\text{sp}} = \frac{\gamma \hbar^2}{2e^2 M_s^2} g_\perp \delta(\xi - \xi_i) \mathbf{M} \times \frac{\partial \mathbf{M}}{\partial t}, \tag{3.21}$$

where $g_\perp$ is the spin mixing conductance per area, and ξ_i is the ξ coordinate of the spin active interface.

Spin Accumulation Induced by a Pumped Spin Current

The pumped AC spin current is a 1st order quantity in the dynamic magnetization, thus proportional to $M_s \hat{\mathbf{z}} \times \frac{\partial \mathbf{m}}{\partial t}$ at the interface. The AC spin accumulation that is generated in the normal metal due to the spin pumping is thus guaranteed to lie in the xy plane. Let $\mathbf{m}_t \triangleq \mathfrak{R}\left\{ \frac{\partial \mathbf{m}}{\partial t}\Big|_{\xi=\xi_i} \right\}$ be the time derivative of the dynamic magnetization at the interface. With $m_t = |\mathbf{m}_t|$ and $\hat{\mathbf{m}}_t = \mathbf{m}_t/|\mathbf{m}_t|$, the AC spin accumulation can be written as

$$\boldsymbol{\mu}_{\mathrm{AC}}^{(s)} = \mu_{\mathrm{AC}}^{(s)} \left(\hat{\mathbf{z}} \times \hat{\mathbf{m}}_t \right), \tag{3.22}$$

where $\boldsymbol{\mu}_{\mathrm{AC}}^{(s)} = \boldsymbol{\mu}_{\mathrm{AC}}^{(s)}(\xi, \zeta, t)$.

The pumped DC spin current is proportional to $\mathbf{m} \times \frac{\partial \mathbf{m}}{\partial t}$, but in the complex notation used earlier $\dot{\mathbf{m}} = i\omega\mathbf{m}$ so that this cross product appears to zero. We must therefore be careful and calculate the physical, real spin current $\mathfrak{R}\{\mathbf{m}\} \times \frac{\partial \mathfrak{R}\{\mathbf{m}\}}{\partial t} = \mathfrak{R}\{\mathbf{m}\} \times \mathfrak{R}\{\dot{\mathbf{m}}\}$. With Eq. (3.5), we find

$$\begin{aligned} \mathfrak{R}\{\mathbf{m}\} \times \frac{\partial \mathfrak{R}\{\mathbf{m}\}}{\partial t}\bigg|_{\xi=\xi_i} &= \\ & \hat{\mathbf{z}}\frac{i}{2}\left[\mathfrak{I}\{X_Q\}\mathfrak{R}\{Y_Q\} - \mathfrak{R}\{X_Q\}\mathfrak{I}\{Y_Q\}\right]_{\xi=\xi_i} e^{-2\mathfrak{I}\{\omega\}t}\mathfrak{R}\{\omega\}, \end{aligned} \tag{3.23}$$

i.e. parallel to $\mathbf{M_0} = M_s\hat{\mathbf{z}}$, and independent of the ζ coordinate. The DC spin accumulation due to spin pumping can thus be written as

$$\boldsymbol{\mu}_{\mathrm{DC}}^{(s)} = \mu_{\mathrm{DC}}^{(s)}\hat{\mathbf{z}}, \tag{3.24}$$

where $\boldsymbol{\mu}_{\mathrm{DC}}^{(s)} = \boldsymbol{\mu}_{\mathrm{DC}}^{(s)}(\xi, t)$, and $\mu_{\mathrm{DC}}^{(s)}$ is assumed to be a second order quantity in the dynamic magnetization.

The total induced spin accumulation in the normal metal due to spin pumping from the ferromagnetic insulator becomes

$$\boldsymbol{\mu}_{\mathrm{sp}}^{(s)} = \boldsymbol{\mu}_{\mathrm{AC}}^{(s)} + \boldsymbol{\mu}_{\mathrm{DC}}^{(s)}, \tag{3.25}$$

where the total spin accumulation must be proportional to $\mathbf{M} \times \partial_t\mathbf{M}$.

3.2.3 Spin Diffusion

The spin diffusion in the normal metal follows

$$\frac{\partial \boldsymbol{\mu}_{\mathrm{sp}}^{(s)}}{\partial t} = D\nabla^2\boldsymbol{\mu}_{\mathrm{sp}}^{(s)} - \frac{\boldsymbol{\mu}_{\mathrm{sp}}^{(s)}}{\tau_{\mathrm{sf}}}, \tag{3.26}$$

where τ_{sf} is the spin flip time in the normal metal.[23] We have neglected a term corresponding to precession of the spin accumulation around the external field. The precession frequency is close to γH_e, depending on the demagnetization field. Here H_e is the applied external field. If spin flip processes are much faster than the precession period, we can neglect the left hand side as well as any precession terms, giving the simplified equation

$$\nabla^2 \boldsymbol{\mu}_{\text{sp}}^{(s)} \approx \frac{1}{D\tau_{\text{sf}}} \boldsymbol{\mu}_{\text{sp}}^{(s)} = l_{\text{sf}}^{-2} \boldsymbol{\mu}_{\text{sp}}^{(s)}, \tag{3.27}$$

where $l_{\text{sf}} \triangleq \sqrt{D\tau_{\text{sf}}}$ is the characteristic spin-flip relaxation length of the normal metal layer. Inserting the spin accumulation, to second order in the dynamic magnetization gives

$$(\nabla^2 - l_{\text{sf}}^{-2}) \boldsymbol{\mu}_{\text{sp}}^{(s)} = (\nabla^2 - l_{\text{sf}}^{-2}) \left[\mu_{\text{AC}}^{(s)} (\hat{\mathbf{z}} \times \hat{\mathbf{m}}_t) + \mu_{\text{DC}}^{(s)} \hat{\mathbf{z}} \right] = 0, \tag{3.28}$$

so that by collecting vector components and using that $\mu_{\text{AC}}^{(s)} \propto e^{-iQ\zeta}$, stemming from the dynamic magnetization's ζ-dependence, we get the two differential equations

$$\left(\frac{\partial^2}{\partial \xi^2} + \frac{\partial^2}{\partial \zeta^2} \right) \mu_{\text{AC}}^{(s)} = l_{\text{sf}}^{-2} \mu_{\text{AC}}^{(s)}, \tag{3.29a}$$

$$\frac{\partial^2}{\partial \xi^2} \mu_{\text{DC}}^{(s)} = l_{\text{sf}}^{-2} \mu_{\text{DC}}^{(s)}, \tag{3.29b}$$

which both can be written as

$$\frac{\partial^2}{\partial \xi^2} \mu_j^{(s)} = l_{\text{sf},j}^{-2} \mu_j^{(s)} \tag{3.30}$$

where the index j is either 'AC' or 'DC', with $l_{\text{sf,DC}} = l_{\text{sf}}$ and $l_{\text{sf,AC}} \triangleq l_{\text{sf}} \left(1 + l_{\text{sf}}^2 Q^2\right)^{-1/2}$, which is the effective AC spin diffusion length.

Applying Ohm's law, $\mathbf{j} = \sigma \mathbf{E}$, in the normal metal, where σ is the conductivity in the normal metal, the spin current along the ξ axis becomes

$$\mathbf{j}^{(s)}(\xi) \approx -\frac{\hbar\sigma}{2e^2} \frac{\partial \boldsymbol{\mu}_{\text{sp}}^{(s)}}{\partial \xi}. \tag{3.31}$$

This spin current must disappear at the free surface of the normal metal, so that $\mathbf{j}^{(s)}\left(\frac{L}{2}+d\right)=0$. Solving Eq. (3.30) with this boundary condition gives

$$\mu_j^{(s)}=\mu_{j,0}^{(s)}\frac{\sinh\left(\frac{1}{\lambda}\left[\xi-\left(\frac{L}{2}+d\right)\right]\right)}{\sinh\left(-\frac{d}{\lambda}\right)}, \tag{3.32}$$

where $\mu_{j,0}^{(s)}=\mu_j^{(s)}(\xi=L/2)$ is time dependent, but depends on the ζ coordinate only in the case of $j=\text{AC}$. This function must be determined from spin current conservation at the spin active interface. Combining the spin current from spin pumping (see Eq. (3.20)) with the back flowing spin current due to the spin pumping induced spin accumulation (i.e. a spin transfer, see Eq. (3.18)), the spin current balance at the interface becomes

$$\left[-\frac{\hbar^2}{2e^2M_s^2}g_\perp\mathbf{M}\times\frac{\partial\mathbf{M}}{\partial t}+\frac{\hbar}{e^2M_s^2}g_\perp\mathbf{M}\times\left(\mathbf{M}\times\boldsymbol{\mu}_{\text{sp}}^{(s)}\right)\right]_{\xi=L/2}= \\ -\frac{\hbar\sigma}{2e^2}\left.\frac{\partial\boldsymbol{\mu}_{\text{sp}}^{(s)}(\xi)}{\partial\xi}\right|_{\xi=L/2}, \tag{3.33}$$

where

$$-\frac{\hbar\sigma}{2e^2}\left.\frac{\partial\boldsymbol{\mu}_j^{(s)}}{\partial\xi}\right|_{\xi=L/2}=\frac{\hbar\sigma}{2e^2\lambda}\coth\left(\frac{d}{\lambda}\right)\mu_{j,0}^{(s)}\hat{\mathbf{s}}_i, \tag{3.34}$$

is found using Eq. (3.32).

Using the equations above and the fact that $\boldsymbol{\mu}_{\text{sp}}^{(s)}\propto\mathbf{M}\times\partial_t\mathbf{M}$, which is perpendicular to $\mathbf{M}$, it is straight forward to show that the spin transfer torque from the spin back flow has the same form as the spin pumping torque. Thus, by solving Eq. (3.33) it is found that the presence of the spin back flow from the adjacent normal metal layer renormalizes the spin mixing conductance, giving

$$\boldsymbol{\tau}_{\text{sp}}+\boldsymbol{\tau}_{\text{bf}}=\frac{\gamma\hbar^2}{2e^2M_s^2}\tilde{g}_\perp\delta\left(\xi-\frac{L}{2}\right)\mathbf{M}_0\times\frac{\partial\mathbf{m}}{\partial t}, \tag{3.35}$$

where

$$\tilde{g}_\perp\triangleq g_\perp\left\{1-\left[1+\frac{\sigma}{2g_\perp l_{\text{sf,AC}}}\coth\left(\frac{d}{l_{\text{sf,AC}}}\right)\right]^{-1}\right\}. \tag{3.36}$$

This renormalization becomes significant if the spin mixing conductance becomes large compared to $\sigma/l_{\mathrm{sf,AC}}$, and should in such cases be accounted for when estimating the spin mixing conductance from ferromagnetic resonance experiments.

3.3 LLG Boundary Conditions

Following the proceedure of Rado and Weertman[75], we integrate the equation of motion in Eq. (2.32), with the added torques from spin pumping and spin back flow, over a small pill box volume straddling one of the interfaces (one ξ_j)

$$\frac{1}{\gamma}\int_{\mathcal{V}_{\mathrm{pb}}} d\mathbf{r}\left[\frac{\partial \mathbf{m}}{\partial t} - \frac{\alpha}{M_s}\mathbf{M}\times\frac{\partial \mathbf{m}}{\partial t} + \gamma\mathbf{M}\times(\mathbf{H}_i + \mathbf{h}_d)\right] = \\ \int_{\mathcal{V}_{\mathrm{pb}}} d\mathbf{r}\left[-\mathbf{M}\times\left(\frac{2A}{M_s^2}\nabla^2\mathbf{M}\right) + \frac{\hbar^2}{2e^2M_s^2}\tilde{g}_\perp\delta(\xi-\xi_j)\mathbf{M}\times\frac{\partial \mathbf{m}}{\partial t}\right],$$

where we have used Eq. (3.2) to be able to write the time derivatives in the equation of motion using the dynamic magnetization component. Letting the thickness of the pill box go to zero, the volume integral on the left hand side will disappear, leaving only the volume integral over the torques due to the exchange interaction and the spin pumping

$$\int_{\mathcal{V}_{\mathrm{pb}}} d\mathbf{r}\left[-\mathbf{M}\times\left(\frac{2A}{M_s^2}\nabla^2\mathbf{M}\right) + \frac{\hbar^2}{2e^2M_s^2}\tilde{g}_\perp\delta(\xi-\xi_j)\mathbf{M}\times\frac{\partial \mathbf{m}}{\partial t}\right] = 0. \tag{3.37}$$

Writing out the cross product in the first term

$$\mathbf{M}\times\nabla^2\mathbf{M} = \hat{\boldsymbol{\xi}}(M_\eta\nabla^2M_\zeta - M_\zeta\nabla^2M_\eta) + \hat{\boldsymbol{\eta}}(M_\zeta\nabla^2M_\xi - M_\xi\nabla^2M_\zeta) + \\ + \hat{\boldsymbol{\zeta}}(M_\xi\nabla^2M_\eta - M_\eta\nabla^2M_\xi),$$

and applying Green's theorem[76] componentwise,

$$\int_{\mathcal{V}} dV\,\left[f\nabla^2 g - g\nabla^2 f\right] = \int_{\mathcal{S}} dS\hat{\mathbf{n}}\cdot\left[f\nabla g - g\nabla f\right], \tag{3.38}$$

the first integrand in Eq. (3.37) becomes

$$-\frac{2A}{M_s^2}\int_{\mathcal{V}_{\mathrm{pb}}} d\mathbf{r}\,\left[\mathbf{M}\times\nabla^2\mathbf{M}\right] = \int_{\mathcal{S}_{\mathrm{pb}}} dS\left[-\frac{2A}{M_s^2}\mathbf{M}\times\frac{\partial\mathbf{M}}{\partial n}\right],$$

where $d\mathbf{S} = dS\hat{\mathbf{n}}$ is the surface element vector pointing out of the pill box volume, so that $\frac{\partial \mathbf{M}}{\partial n}$ is the derivative normal to the pillbox surface. Eq. (3.37) now becomes

$$0 = -\frac{2A}{M_s^2}\int_{\mathcal{S}_{\text{pb}}} dS\, \mathbf{M} \times \frac{\partial \mathbf{M}}{\partial n} + \int_{S_{\text{lid}}} dS\, \frac{\hbar^2}{2e^2 M_s^2}\tilde{g}_\perp \left[\mathbf{M} \times \frac{\partial \mathbf{m}}{\partial t}\right]_{\xi=\xi_j},$$

where S_{sp} is the whole surface of the pillbox, whereas S_{lid} is the cross sectional surface area of the pill box at $\xi = \xi_j$. The first term gives a measure of the continuity of the magnetization across the interface. Since the magnetization is assumed to be zero outside the ferromagnet, only the pillbox lid with normal into the film will contribute. Letting the pill box thickness go to zero, we are left with

$$\int_{S_{\text{lid}}} dS \left(\pm\frac{2A}{M_s^2}\left[\mathbf{M} \times \frac{\partial \mathbf{M}}{\partial \xi}\right]_{\xi=\xi_j} + \frac{\hbar^2}{2e^2 M_s^2}\tilde{g}_\perp \left[\mathbf{M} \times \frac{\partial \mathbf{m}}{\partial t}\right]_{\xi=\xi_j} \right) = 0, \quad (3.39)$$

Assuming this holds for any pill box shape, we arrive at

$$\pm\frac{2A}{M_s^2}\left[\mathbf{M} \times \frac{\partial \mathbf{M}}{\partial \xi}\right]_{\xi=\xi_j} + \frac{\hbar^2}{2e^2 M_s^2}\tilde{g}_\perp \left[\mathbf{M} \times \frac{\partial \mathbf{m}}{\partial t}\right]_{\xi=\xi_j} = 0, \quad (3.40)$$

which is the exchange–pumping boundary condition.

3.3.1 Surface anisotropy

We choose a surface anisotropy with an easy axis pointing along the direction $\hat{\mathbf{n}}$. The free energy contribution is then given as

$$F_s = \int d\mathbf{r}\, K_s \left[1 - \left(\frac{\mathbf{M}\cdot\hat{\mathbf{n}}}{M_s}\right)^2\right] \delta\left(\xi - \xi_j\right), \quad (3.41)$$

where $K_s$is the surface anisotropy energy density of the interface, which is assumed to be a constant. By letting K_s become negative, we achieve a hard-axis/easy-plane surface anisotropy. Using Eq. (2.33) the contribution from the surface anisotropy energy to the effective field becomes

$$\mathbf{H}_s = \frac{2K_s}{M_s^2}\left(\mathbf{M}\cdot\hat{\mathbf{n}}\right)\delta\left(\xi - \xi_j\right)\hat{\mathbf{n}}. \quad (3.42)$$

Following the approach of Sec. 3.3, the total boundary condition (including exchange, spin pumping and surface anisotropy) becomes

$$\left[\pm\frac{2A}{M_s^2}\mathbf{M}\times\frac{\partial\mathbf{M}}{\partial\xi}-\frac{2K_s}{M_s^2}\left(\mathbf{M}\cdot\hat{\mathbf{n}}\right)\left(\mathbf{M}\times\hat{\mathbf{n}}\right)+\frac{\hbar^2}{2e^2M_s^2}\tilde{g}_\perp\mathbf{M}\times\frac{\partial\mathbf{m}}{\partial t}\right]_{\xi=\xi_j}=0\,. \tag{3.43}$$

Because the surface anisotropy depends on the relative orientation of $\mathbf{M}$ and $\hat{\mathbf{n}}$, the components X_Q and Y_Q in $\mathbf{m}$ will experience different boundary conditions in certain geometries. This was explored in more detail in the scientific papers contained within this thesis. The approach and the results are reiterated over in the next chapter.

4 *Summary of Scientific Papers*

This chapter goes into some of the details of Paper I through IV,[77–80] with one section per paper. Due to the similarity of the formalism used in the first three papers, most of the details is presented in Sec. 4.1.

The fourth paper is related to work I did in the beginning of my time as a Ph.D. student, back when I was collaborating with Erik Wahlström. It was on a different topic than the main work described in this thesis and therefore only a brief summary is given in Sec. 4.4.

4.1 Spin-pumping and Enhanced Gilbert Damping in Thin Magnetic Insulator Films

At the time we started working on Paper I,[77] the experimental demonstration that spin transfer and spin pumping could be as effective in magnetic insulators as in metallic ferromagnetic systems were rather surprising.[30] Because of the low intrinsic damping found in ferromagnetic insulators such as YIG, the prospect of utilizing spin pumping and spin transfer in such systems resulted in frenetic activity within the community.[30;81–86;67;87–89]

When a ferromagnetic insulator is brought in contact with a normal metal the magnetization dynamics of the ferromagnet induces spin pumping of angular momentum into the intinerant electron system of the normal metal. It was experimentally observed that spin pumping in such a system was dependent on the system geometry, field configuration (see Sec. 3.1) and the excited mode profiles of the spin waves in the system.[81;83;84;67;88;89] Sandweg et al.[83] demonstrated that the dissipation was larger for modes localized at the ferromagnetic insulator–normal metal interface.

Our goal was to combine the lessons learned from older research on the topic of spin wave dynamics (see Sec. 3.1.2) with the new observations of spin pumping in such systems. As stated in Paper I,[77] we wanted to present a coherent theoretical picture of the experimental findings at the time.

4.1.1 Solution Method

In Paper I we solved the linearized LLG equation in a ferromagnetic insulator–normal metal bilayer system. The interface was assumed to be spin active through the spin pumping effect. We added the spin pumping torque of Eq. (3.21) to the right side of the LLG equation (see Eq. (2.32). The effects of the spin back flow from the normal metal was not included, and we assumed that the normal metal would act as a perfect spin sink.

We assumed that the magnetization was close to saturation, M_s, and precessing around the equilibrium direction of the internal field, $\mathbf{H}_i$, (see Sec. 3.1). Using that $|\mathbf{m}| \ll M_s$, the equation of motion was linearized in the dynamic magnetization, giving

$$\left[i\frac{\omega}{\omega_M}\begin{pmatrix} \alpha & -1 \\ 1 & \alpha \end{pmatrix} + \mathbf{I}\left(\frac{\omega_H}{\omega_M} + 8\pi\frac{\gamma^2 A}{\omega_M^2}\left[Q^2 - \frac{d^2}{d\xi^2} \right] \right) \right] \mathbf{m}_Q(\xi) = \int_{-\frac{L}{2}}^{\frac{L}{2}} d\xi' \,\widehat{\mathcal{G}}^{(xy)}(\xi - \xi')\mathbf{m}_Q(\xi'), \quad (4.1)$$

where $\mathbf{m}_Q$ is described in Sec. 3.1.1, $\mathbf{I}$ is the unit matrix, $\omega_M = 4\pi\gamma M_s$, $\omega_H = \gamma H_i$, and $\widehat{\mathcal{G}}^{(xy)}$ is the dipole–dipole interaction tensor described in Sec. 3.1.2.

When QL is large, the exchange interaction dominates over the dipole–dipole interactions, such that the right hand side of Eq. (4.1) can be neglected, and the bulk equation of motion turns into a simple eigenvalue problem. Because the identity matrix of the second term commutes with the time evolution matrix, $\left(\begin{smallmatrix} i\alpha & -i \\ i & i\alpha \end{smallmatrix}\right)^{-1}$, the eigenvectors are given by $(1\ {-i})^T$ and $(1\ i)^T$, provided that $\alpha \ll 1$. These are circularly polarized eigenvectors, with the corresponding eigenvalues $i\alpha \pm 1$. The total eigenfrequency of the exchange dominated spin wave problem is then determined by exchange operator.

When the dipole–dipole interactions are important, the problem becomes much more complicated. It is easy to see that the time evolution matrix described above does not commute with the dipole–dipole tensor $\widehat{\mathcal{G}}^{(xy)}$. In this situation the modes are not likely to be circularly polarized. Because the bulk equation still describes a precessing motion around the equilibrium direction, the dynamic magnetization must be elliptically polarized.

However, these results are only valid when ignoring the boundary conditions imposed by the film geometry. To solve the thin film problem the boundary conditions in Eq. (3.43) must be solved simultaneously with Eq. (4.1). Choosing the surface anisotropy axis in Eq. (3.41) to be the thin film's normal axis, i.e. $\hat{\mathbf{n}} = \hat{\boldsymbol{\xi}}$, and linearizing Eq. (3.43), we found that the linearized boundary condition at the spin-active interface was given by

$$\left(L\frac{\partial}{\partial\xi} + i\omega\chi + \frac{LK_s}{A}\cos(2\theta) \right) m_{Q,x}(\xi) \bigg|_{\xi=\frac{L}{2}} = 0, \tag{4.2a}$$

$$\left(L\frac{\partial}{\partial\xi} + i\omega\chi + \frac{LK_s}{A}\cos^2(\theta) \right) m_{Q,y}(\xi) \bigg|_{\xi=\frac{L}{2}} = 0, \tag{4.2b}$$

where $\chi = L\hbar g_\perp / 4Ae^2$. For simplicy we assumed that the substrate interface (the spin-inactive interface) had no surface anisotropy, so that this boundary condition was simply $\partial_\xi \mathbf{m}_Q(\xi = -L/2) = 0$.

There are two challenges introduced by these boundary conditions. Firstly, the surface anisotropy breaks the symmetry between the x and y components, unless $\theta = 0$ (perpendicular field geometry). Secondly, and most importantly, the system eigenfrequency, ω, appears in the boundary conditions because of the spin pumping effect. This equation system can be solved when there is no spin pumping (i.e. $g_\perp = 0$) by expanding $\mathbf{m}_Q(\xi)$ into the eigenfunctions of the exchange operator (the second term in Eq. (4.1)).[54] The eigenvalue problem corresponding to the exchange operator forms a 2-dimensional Sturm Liouville problem[90] ensuring that there exists a complete set of eigenfunctions. However, when $g_\perp > 0$ and the eigenvalue appears in the boundary conditions such expansions are not possible anymore.

We opted to first solve the equation system in the limit of $QL \ll 1$. In this limit, only the δ-function in $\widehat{\mathcal{G}}_{\xi\xi}$ (see Eq. (3.9)) is important, which corresponds with the existence of a dynamic demagnetization field across the film thickness. This demagnetization field is similar to the static demagnetization field that is baked into the internal field $\mathbf{H}_i$.

Because of the exchange operators, the eigenvectors become transverse standing waves across the film thickness

$$\mathbf{m}_Q = \mathbf{m}_{Q,xy} \left(e^{ik\xi} + e^{-ik\xi + \varphi} \right), \tag{4.3}$$

where $\mathbf{m}_{Q,xy}$ is some, in general, elliptically polarized coefficient vector. Furthermore, φ is trivially determined by the substrate boundary condition.

If there is no surface anisotropy at the spin-active interface, then the boundary conditions in Eq. (4.2) reduces to the equation

$$kL \tan(kL) = i\omega\chi. \tag{4.4}$$

Eq. (4.3) inserted into Eq. (4.1) gives the equation

$$\begin{aligned} \frac{\omega}{\omega_M} = \mp \sqrt{\left(\frac{\omega_H}{\omega_M} + \frac{A}{2\pi M_s^2} k^2 \right) \left(\frac{\omega_H}{\omega_M} + \frac{A}{2\pi M_s^2} k^2 + \sin^2\theta \right)} + \\ + i\alpha \left(\frac{\omega_H}{\omega_M} + \frac{A}{2\pi M_s^2} k^2 + \frac{\sin^2\theta}{2} \right), \end{aligned} \tag{4.5}$$

which together with Eq. (4.4) forms a system of two equations for ω and k.

Solving this system in the weak pumping limit, i.e. $\omega\chi \ll 1$, the frequency dependent imaginary parts of k^2 are found to renormalize the Gilbert damping, $\alpha \to \alpha + \Delta\alpha$. As expected, the ground state macrospin mode with $k \approx 0$ reproduces the result of Tserkovnyak et al.[23] with

$$\Delta\alpha = \frac{\gamma\hbar^2 g_\perp}{2LM_s e^2}, \tag{4.6}$$

while the higher lying *volume modes*, characterized by their n internal nodes across the film thickness, were shown to exhibit twice the renormalization of the Gilbert damping. This was one of the major new results of Paper I.

To model the problem with easy axis surface anisotropy, $K_s > 0$, we introduced two wave numbers, k_x and k_y, one for each component of $\mathbf{m}_Q$. With this ansatz the boundary conditions became

$$k_x L \tan(k_x L) = i\omega\chi + \frac{LK_s}{A}\cos(2\theta), \tag{4.7a}$$

$$k_y L \tan\left(k_y L\right) = i\omega\chi + \frac{LK_s}{A}\cos^2(\theta). \tag{4.7b}$$

where we further assumed that we had an in-plane applied field. Only the macrospin mode is significantly changed by the addition of the surface anisotropy. It is transformed into a surface mode localized at the spin-active interface. By solving Eqs. (4.7) together with the bulk equation of motion it was possible to calculate the renormalization of the Gilbert damping in the weak pumping limit. We found that for large values of LK_s/A the renormalization for the surface mode was

$$\Delta\alpha_{n=0} = \frac{\gamma\hbar K_s}{4\pi M_s A}\frac{h}{e^2}g_\perp\frac{\omega_H}{\omega_M}\left[\frac{\omega_H}{\omega_M} + \frac{1}{2} - \frac{K_s^2}{4\pi M_s^2 A}\right]^{-1}, \tag{4.8}$$

which was the second major new result of Paper I.

4.1.2 Numerical Calculations for Intermediate values of QL

We developed a numerical code for calculating the Gilbert damping renormalizations for the transverse modes at intermediate in-plane wavenumbers, QL. I will in the following illustrate how Eq. (4.1) and Eq. (4.2) can be shaped into a matrix eigenvalue problem through discretization using finite difference methods. Let $\mathbf{m}_{Q,d}$ be a one dimensional column vector of height $2n$ where the first n rows correspond to $X_Q(\xi)$ and rows $n+1$ through $2n$ correspond to $Y_Q(\xi)$ of Eq. (3.5) evaluated at the discretized points $\xi_i = -L/2 + (i-1)\Delta L$ with $i = 1, 2, ..., n$ and $\Delta L = L/(n-1)$.

Discretized boundary conditions

We employed the pumping-exchange boundary condition (see Eq.(4.2)) at the upper interface ($i = n$), and the pure-exchange boundary condition at the lower interface ($i = 1$). For each component of $\mathbf{m}_Q$ the boundary conditions can be written as

$$b_1^l m_1 + b_2^l m_2 + \dots + b_n^l m_n = 0 \tag{4.9a}$$

$$b_1^u m_1 + b_2^u m_2 + \dots + b_n^u m_n = 0, \tag{4.9b}$$

where m_i is either $X_Q(\xi_i)$ or $Y_Q(\xi_i)$, and b_i^l are the discretization coefficients for the substrate side (spin in-active interface) and b_i^u are the discretization coefficients for the normal metal (spin-active) interface for the corresponding component of $\mathbf{m}_Q$. If a first or second derivative is approximated with a finite difference stencil using $N+1$ nodes, the truncation error scale like $\mathcal{O}\left(\Delta L^N\right)$ for central difference stencils and like $\mathcal{O}\left(\Delta L^{N-1}\right)$ for skew stencils.[91;92] By choosing skew stencils for the derivatives in the boundary conditions in Eq. (4.2) the first $N+1$ coefficients in the vector $\mathbf{b}^l$ becomes nonzero while the last $N+1$ coefficients in the vector $\mathbf{b}^u$ are nonzero.[1]

Solving the equation set in Eq. (4.9b) for the two boundary points m_1 and m_n, we have

$$\begin{pmatrix} m_1 \\ m_n \end{pmatrix} = \begin{pmatrix} b_1^l & b_n^l \\ b_1^u & b_n^u \end{pmatrix}^{-1} \cdot \begin{pmatrix} -\mathbf{b}_{2;n-1}^l \cdot \mathbf{m}_{2;n-1} \\ -\mathbf{b}_{2;n-1}^u \cdot \mathbf{m}_{2;n-1} \end{pmatrix}, \tag{4.10}$$

where $\mathbf{m}_{2;n-1}$ is the discretized vector of a component of $\mathbf{m}_Q(\xi_i)$ evaluated at the discretized points $i = 2, 3, \dots, n-1$, and $\mathbf{b}_{2;n-1}^{l,u}$ is the corresponding coefficients from the boundary conditions. The boundary condition on one side of the film will not include the other interface point unless $n = N+1$ exactly. Generally, we are going to need to choose $n \gg N$ so that we can safely assume that $b_n^l = b_1^u = 0$. Our equation for m_1 and m_n is then simplified to

$$\begin{pmatrix} m_1 \\ m_n \end{pmatrix} = \begin{pmatrix} \frac{1}{b_1^l} & 0 \\ 0 & \frac{1}{b_n^u} \end{pmatrix} \cdot \begin{pmatrix} -\mathbf{b}_{2;n-1}^l \cdot \mathbf{m}_{2;n-1} \\ -\mathbf{b}_{2;n-1}^u \cdot \mathbf{m}_{2;n-1} \end{pmatrix}. \tag{4.11}$$

From Eq. (4.2) we find that

$$\frac{1}{b_n^u} = \frac{1}{c\frac{L}{\Delta L} + d + i\omega\chi}, \tag{4.12}$$

---

[1] It is also possible to use $N+1$ nodes for the central difference stencil and $N+2$ nodes for the skew stencils.

where c is a coefficient stemming from the discretization of the first derivative in the boundary condition, and $d = LK_s/A$ is a dimensionless "pinning" parameter due to the surface anisotropy at the interface. Expanding this expression to second order in the small quantity $\Delta L/L$, we find

$$\frac{1}{b_n^u} = \frac{1}{c}\frac{\Delta L}{L} - \frac{d + i\omega\chi}{c^2}\left(\frac{\Delta L}{L}\right)^2 + \mathcal{O}\left(\frac{\Delta L}{L}\right)^3, \tag{4.13}$$

which has a term linear in the eigenfrequency ω. This equation also shows that our method can not be used with a discretization scheme using less than $3 + 2 = 5$ nodes, which ensures that the skew stencils are of the same order in ΔL as the equation above. For the discretization of the bulk equation we must therefore choose a 4th order method (see the discussion above concerning central difference stencils).

Finite Difference Stencils

The 4th order central difference stencils with truncation error $\mathcal{O}\left(\Delta L^4\right)$ are given by

$$\frac{\partial f(\xi_i)}{\partial \xi} \approx \frac{f_{i+2} + 8f_{i+1} - 8f_{i-1} - f_{i-2}}{12\Delta L}, \tag{4.14a}$$

$$\frac{\partial^2 f(\xi_i)}{\partial \xi^2} \approx \frac{-f_{i+2} + 16f_{i+1} - 30f_i + 16f_{i-1} - f_{i-2}}{12\Delta L^2}, \tag{4.14b}$$

which can be found by Taylor expanding $f(\xi_j)$ for the five points centered around ξ_i up to fourth order in $\Delta L/L$ and solving the equation set for the first 4 derivatives $f', f'', f^{(3)}$ and $f^{(4)}$.[91]

The second derivative in the linearized LLG equation (see Eq.(4.1)) can now be represented by a sparse band matrix, but some extra care is needed for the endpoints: we either have to include ghost points outside the domain, or use increasingly skew stencils when approaching the edges. These stencils have truncation error $\mathcal{O}\left(\Delta L^3\right)$ and can be found in a similar manner to the central difference stencils described above.

The totally skew stencils employed in solving the discretized boundary condition, are

$$\frac{\partial f(\xi_1)}{\partial \xi} \approx \frac{-25f_1 + 48f_2 - 36f_3 + 16f_4 - 3f_5}{12\Delta L}, \tag{4.15a}$$

$$\frac{\partial f(\xi_n)}{\partial \xi} \approx \frac{3f_{n-4} - 16f_{n-3} + 36f_{n-2} - 48f_{n-1} + 25f_n}{12\Delta L}, \tag{4.15b}$$

which were found in a similar manner to the central difference stencils above.

Convolution Quadrature and The dipole–dipole Tensor

A convolution integral of the form

$$y(x) = \int_{-a}^{b} f(x-x')g(x')\,dx' \tag{4.16}$$

can be discretized into a sum

$$y_i = y(x_i) \approx \Delta L \cdot \sum_{j=1}^{n} f(x_i - x_j) \cdot w_j g(x_j), \tag{4.17}$$

where w_j are the quadrature's weighting coefficients, which are chosen to be some 4th order extended formula e.g. the extended Simpson's rule.[92] The function evaluations of f becomes

$$f(x_i - x_j) = f((i-j)\cdot \Delta L), \tag{4.18}$$

Thus, with $i, j = 1, 2, ..., n$, the function f will be evaluated at $2n-1$ points to get the whole $y(x_i)$ vector. The convolution quadrature now looks like a vector product between two vectors:

$$\begin{aligned} y_i =& \Delta L \cdot \begin{pmatrix} f_{i-1} & f_{i-2} & \cdots & f_{i-n} \end{pmatrix} \cdot \begin{pmatrix} w_1 g_1 \\ w_2 g_2 \\ \vdots \\ w_n g_n \end{pmatrix} \\ =& = \Delta L \cdot \begin{pmatrix} w_1 f_{i-1} & w_2 f_{i-2} & \cdots & w_n f_{i-n} \end{pmatrix} \cdot \begin{pmatrix} g_1 \\ g_2 \\ \vdots \\ g_n \end{pmatrix} \end{aligned}$$

$$y_i = \Delta L \begin{pmatrix} f_{i-1} & f_{i-2} & \cdots & f_{i-n} \end{pmatrix} \cdot \begin{pmatrix} w_1 & 0 & \cdots & 0 \\ 0 & w_2 & \cdots & 0 \\ \vdots & \vdots & \ddots & \vdots \\ 0 & 0 & \cdots & w_n \end{pmatrix} \cdot \begin{pmatrix} g_1 \\ g_2 \\ \vdots \\ g_n \end{pmatrix}. \tag{4.19}$$

Hence, the whole discretized convolution integral, $\mathbf{y}_i$, can be written as

$$\mathbf{y}_i = \Delta L \cdot \begin{pmatrix} f_0 & f_{-1} & \cdots & f_{1-n} \\ f_1 & f_0 & \cdots & f_{2-n} \\ \vdots & \vdots & \ddots & \vdots \\ f_{n-1} & f_{n-2} & \cdots & f_0 \end{pmatrix} \cdot \begin{pmatrix} w_1 & 0 & \cdots & 0 \\ 0 & w_2 & \cdots & 0 \\ \vdots & \vdots & \ddots & \vdots \\ 0 & 0 & \cdots & w_n \end{pmatrix} \cdot \begin{pmatrix} g_1 \\ g_2 \\ \vdots \\ g_n \end{pmatrix}. \tag{4.20}$$

This relation allows us to write the dipole–dipole integral as a $2n \times 2n$ matrix operator acting on the magnetization vector $\mathbf{m}_{Q,d}$. The four $n \times n$ sub-blocks of this operator correspond to each of the four tensor elements $\widehat{\mathcal{G}}_{i,\cdot}$

With the dipole–dipole convolution integral as a matrix operator it is easy to see that the discretized version of the linearized bulk LLG equation (4.1) becomes a matrix eigenvalue problem. The next hurdle to tackle was how to embed the ω dependent spin pumping boundary conditions within this eigenvalue formulation.

Reduction of the System Matrices Using Boundary Conditions

We are were now in a position to reduce our $2n \times 2n$ matrix eigenvalue problem to a $(2n-4) \times (2n-4)$ eigenvalue problem by using our solved boundary condition (see Eq. (4.11)).

All terms from Eq. (4.1) that are independent of ω can be represented by one large system matrix, given by

$$\mathbf{S}^{\text{bulk}} = \Delta L \begin{pmatrix} \mathbf{G}_{xx} \cdot \mathbf{W} & \mathbf{G}_{xy} \cdot \mathbf{W} \\ \mathbf{G}_{xy} \cdot \mathbf{W} & \mathbf{G}_{yy} \cdot \mathbf{W} \end{pmatrix} - \left(\frac{\omega_H}{\omega_M} + 8\pi \frac{\gamma^2 A}{\omega_M^2} Q^2 \right) \mathbf{I}_{2n} + 8\pi \frac{\gamma^2 A}{\omega_M^2} \mathbf{X}_{2n}, \tag{4.21}$$

where $\Delta L \mathbf{G}_{ij} \cdot \mathbf{W}$ represents $n \times n$ sub blocks of the total dipole–dipole convolution matrix, with $\mathbf{W}$ being the diagonal quadrature weighting matrix; $\mathbf{I}_{2n}$ is a $2n \times 2n$ identity matrix and $\mathbf{X}_{2n}$ is the transverse derivative band matrix.

For each of the four $n \times n$ sub-blocks in $\mathbf{S}^{\mathrm{bulk}}$ we must eliminate the top and bottom rows so that we do not overdetermine our problem. This is because we have two boundary conditions for each component that we discretized and solved for the edge points in the previous section. We are now left with 4 sub blocks of size $(n-2) \times n$. The leftmost and rightmost column of these sub blocks can be eliminated using our solved boundary conditions from Eq. (4.11).

This can best described as taking an outer product between the outer columns of each sub block of $\mathbf{S}^{\mathrm{bulk}}$ with the corresponding coefficient vector in the solved boundary condition and adding this to the internal $(n-2) \times (n-2)$ part of the block. The reduced system matrix' sub blocks $\mathbf{S}^*$ become

$$\mathbf{S}^* = \mathbf{S}^{\mathrm{bulk}}_{2;n-1,2;n-1} + \mathbf{S}^{\mathrm{bulk}}_{2;n-1,1} \otimes \left(-\frac{\mathbf{b}^l_{2;n-1}}{b^l_1} \right) + \mathbf{S}^{\mathrm{bulk}}_{2;n-1,n} \otimes \left(-\frac{\mathbf{b}^u_{2;n-1}}{b^u_n} \right) \tag{4.22}$$

where $\mathbf{S}^{\mathrm{bulk}}_{i,j}$ is the ith row and jth column of $\mathbf{S}^{\mathrm{bulk}}$, and the notation $\mathbf{S}^{\mathrm{bulk}}_{i_{min};i_{max},j}$ corresponds to picking out the rows from i_{min} to i_{max} of the jth column vector.

So far, we have reduced our system matrix's size from $2n \times 2n$ down to $(2n-4) \times (2n-4)$ by embedding the boundary conditions in the interior points. In the process we introduced terms proportional to ω into the internals of $\mathbf{S}^*$ from the exchange-pumping boundary condition. We now split the reduced system matrix into two parts, letting $\mathbf{S}^* = \mathbf{S} + \frac{\omega}{\omega_M}\mathbf{P}$, so that our discretized equation of motion with embedded boundary conditions become

$$\mathbf{S} \cdot \mathbf{m}^*_{Q,d} = \frac{\omega}{\omega_M}(\mathbf{D} - \mathbf{P}) \cdot \mathbf{m}^*_{Q,d}, \tag{4.23}$$

which is a $(2n-4) \times (2n-4)$ complex eigenvalue problem over the interior points of the domain, ξ_i for $i = 2, 3, ..., n-1$, and where $\mathbf{D}$ is the discretized version of the time evolution matrix, $\left(\begin{smallmatrix} i\alpha & -i \\ i & i\alpha \end{smallmatrix}\right)$. $\mathbf{m}^*_{Q,d}$ is the reduced column vector corresponding to the interior points. The Gilbert damping renormalization can now be found for each eigenvector by comparing $\Im\{\omega\}$ as obtained by solving (4.23) for both the cases $g_\perp = 0$ and $g_\perp \neq 0$.

4.2 Spin Waves In Ferromagnetic Insulators Coupled via a Normal Metal

In Paper II[78] the formalism of Paper I (see Sec. 4.1) was extended to a trilayer system where a normal metal of thickness d_N was sandwitched inbetween two ferromagnetic insulator layers of thicknesses L_1 and L_2.

The equation of motion is the same as Eq. (4.1), except the dipole–dipole interaction integral where the integration was extended to encompass both insulator films. This can be viewed as each film having a dipole self energy as well as interlayer dipole energy. The linearized equation of motion for the trilayer system becomes

$$\left[i\frac{\omega}{\omega_M}\begin{pmatrix}\alpha & -1\\ 1 & \alpha\end{pmatrix} + \mathbf{I}\left(\frac{\omega_H}{\omega_M} + 8\pi\frac{\gamma^2 A}{\omega_M^2}\left[Q^2 - \frac{d^2}{d\xi^2}\right]\right)\right]\mathbf{m}_{i,Q}(\xi) = \sum_{i=1}^{2}\int_{-\infty}^{\infty} d\xi' \,\widehat{\mathcal{G}}^{(xy)}(\xi - \xi')\mathbf{m}_{i,Q}(\xi'), \quad (4.24)$$

where the dynamic magnetization vector has acquired an additional index, i, indicating which film we are looking at; and the integration has been extended to infinity. This works if $m_{1,Q} = 0$ in film 2, and vice versa.

With a trilayer system, we had to account for the spin pumping happening at each FI | NM interface as well as the spin transfer from the spin pumping induced spin accumulation in the NM layer. Because the spin accumulation depends on the dynamics at both FI | NM interfaces, the effect of the spin back flow presented in Sec. 3.2.3 is too simplistic for this system. The spin accumulation becomes

$$\boldsymbol{\mu}_Q = -\frac{\hbar}{2}\mathbf{M}_s \times \left\{[\mathbf{m}_Q(\xi_1) + \mathbf{m}_Q(\xi_2)]\Gamma_1(\xi) - [\mathbf{m}_Q(\xi_1) - \mathbf{m}_Q(\xi_2)]\Gamma_2(\xi)\right\}, \quad (4.25)$$

where ξ_i is the location of the FI | NM interfaces, and where $\Gamma_i(\xi)$ describes the shape of the spin accumulation across the interface.

In the case of equal thickness of the two FI films, $L_1 = L_2 = L$, the 4 spin-active boundary conditions can be solved in a manner similar to the method described in Sec. 4.1.1. The result is that the renormalization of the Gilbert damping is dependent on the symmetry of magnetization in the two films; the dynamic magnetization in the two FI films can couple either *acoustically* (symmetric about the NM) or *optically* (antisymmetric about the NM). In Paper II[78] this is described as a renormalization of the χ parameter, but to stay true to Sec. 4.1.1, it might be better to view it as a renormalization of the mixing conductance. The result was a scaling of the results found in the bilayer system in Paper I, $\Delta\alpha \to \Delta\alpha r_\nu$, where the scaling r_ν is given by

$$r_\mathrm{A} = \left\{1 - \left[1 + \frac{2g_\perp l_\mathrm{sf}}{\sigma} \tanh\left(\frac{d_N}{2l_\mathrm{sf}}\right)\right]^{-1}\right\}, \tag{4.26a}$$

$$r_\mathrm{O} = \left\{1 - \left[1 + \frac{2g_\perp l_\mathrm{sf}}{\sigma} \coth\left(\frac{d_N}{2l_\mathrm{sf}}\right)\right]^{-1}\right\}, \tag{4.26b}$$

for the acoustic and optical modes respectively. These two differ significantly when the NM thickness, d_N, becomes comparable to the spin diffusion length, l_sf. In that case the tanh goes to zero, while the coth blows up. The result is that the spin pumping for the acoustic mode is completely quenched while the optical modes starts acting like two independent bilayer systems in contact with perfect spin sinks.

For unequal thicknesses of the two FI films, $L_1 \neq L_2$, the results are more complicated. In the article we discuss the slow relaxation case, which can be summarized as.: The uniform mode splits into acoustic and optical configurations as before, but the renormalization of the Gilbert damping becomes

$$\Delta\alpha_A = \frac{\gamma\hbar^2 g_\perp}{2M_s e^2} \frac{d_N}{2l_\mathrm{sf}} \frac{\sigma}{g_\perp l_\mathrm{sf}} \frac{1}{L_1 + L_2}, \tag{4.27a}$$

$$\Delta\alpha_O = \frac{\gamma\hbar^2 g_\perp}{2M_s e^2} \frac{1}{2} \left(\frac{1}{L_1} + \frac{1}{L_2}\right). \tag{4.27b}$$

For the higher excited volume modes the transverse wave numbers in the two films can either be integer multiples of one another or not. The latter decouples the two films, so that half the pumped spin current is returned to the original location. This causes the volume modes to experience half the damping renormalization of that of a bilayer film in contact with a perfect spin sink. The first case causes the renormalization to be twice that given in Eq. (4.27b).

By investigating the presence of surface anisotropy in the unequal thickness scenario, we found that the double film surface mode is robust to the thickness variations of the two FI films. This is because in each film the length scale is given by A/K_s, which determines the effective volume of the magnetization dynamics.

4.2.1 Updating the Numerical Code for Trilayers

The main principle behind the numerical code is much the same as it was for the bilayer system in Paper I, albeit more complicated and harder to debug. The ξ axis is discretized into n_1 points in the first FI layer and n_2 points in the second FI layer. This defines the point spacings $\Delta L_i = L_i/(n_i - 1)$ in the two films. The total magnetization vector is discretized into a $2(n_1 + n_2)$ sized column vector, schematically described as $\mathbf{m} = \begin{pmatrix} \mathbf{X}_1 & \mathbf{X}_2 & \mathbf{Y}_1 & \mathbf{Y}_2 \end{pmatrix}^T$. X_i and Y_i are the x and y components of the dynamic magnetization in layer i.

The four boundary conditions, per magnetization component, can be written in a discretized form similar to the formalism used in Sec. 4.1.2 (see Eq. (4.9b))

$$\mathbf{b}^{1,l} \cdot \mathbf{m}_1 = 0, \tag{4.28a}$$

$$\mathbf{b}^{1,u} \cdot \mathbf{m}_1 + \mathbf{a}^{2\to 1} \cdot \mathbf{m}_2 = 0, \tag{4.28b}$$

$$\mathbf{b}^{2,l} \cdot \mathbf{m}_2 + \mathbf{a}^{1\to 2} \cdot \mathbf{m}_1 = 0, \tag{4.28c}$$

$$\mathbf{b}^{2,u} \cdot \mathbf{m}_2 = 0, \tag{4.28d}$$

where the **b** vectors stem from the *local* surface torque, while the **a** vectors represent the interlayer coupling torque originating from the opposite film. The $\mathbf{m}_i$ vector is the discretized column vector of either the x or y component. Because both the spin pumping torque and the spin transfer torque only act at the interface points the exterior parts are zero, $\mathbf{a}^{1\to 2}_{1;n1-1} = \mathbf{a}^{2\to 1}_{2;n2} = 0$. Thus, I rename the important coefficients $a^{1\to 2} \triangleq a^{1\to 2}_{n_1}$ and $a^{2\to 1} \triangleq a^{2\to 1}_{1}$. These are related to the spin accumulation distribution functions $\Gamma_1(\xi)$ and $\Gamma_2(\xi)$ in Eq. (4.25).

Solving the equation system for the edge points m_1, m_{n_1}, m_{n_1+1} and

$m_{n_1+n_2}$, we found

$$\begin{pmatrix} m_1 \\ m_{n_1} \\ m_{n_1+1} \\ m_{n_1+n_2} \end{pmatrix} = - \begin{pmatrix} \frac{1}{b_1^{1,l}} \mathbf{b}_{2;n_1-1}^{1,l} \cdot \mathbf{m}_{2;n_1-1} \\ \frac{b_1^{2,l}}{b_{n_1}^{1,u} b_1^{2,l} - a^{1\to 2} a^{2\to 1}} \mathbf{b}_{2;n_1-1}^{1,u} \cdot \mathbf{m}_{2;n_1-1} \\ \frac{-a^{1\to 2}}{b_{n_1}^{1,u} b_1^{2,l} - a^{1\to 2} a^{2\to 1}} \mathbf{b}_{2;n_1-1}^{1,u} \cdot \mathbf{m}_{2;n_1-1} \\ 0 \end{pmatrix} + \\ - \begin{pmatrix} 0 \\ \frac{-a^{2\to 1}}{b_{n_1}^{1,u} b_1^{2,l} - a^{1\to 2} a^{2\to 1}} \mathbf{b}_{2;n_2-1}^{2,l} \cdot \mathbf{m}_{n_1+2;n_1+n_2-1} \\ \frac{b_{n_1}^{1,u}}{b_{n_1}^{1,u} b_1^{2,l} - a^{1\to 2} a^{2\to 1}} \mathbf{b}_{2;n_2-1}^{2,l} \cdot \mathbf{m}_{n_1+2;n_1+n_2-1} \\ \frac{1}{b_{n_2}^{2,u}} \mathbf{b}_{2;n_2-1}^{2,u} \cdot \mathbf{m}_{n_1+2;n_1+n_2-1} \end{pmatrix}. \tag{4.29}$$

This solution enables the reduction of the system from a $2(n_1+n_2) \times 2(n_1+n_2)$ sized system and down to a $(2(n_1+n_2)-8) \times (2(n_1+n_2)-8)$ sized complex eigenvalue problem, much the same as in the bilayer case. When calculating the system matrix operator for the trilayer system, one has to make sure that the dipole–dipole integral is written correctly such that the moment interdistances take the NM thickness, d_N, into account.

4.3 Spin Pumping, Dissipation, and Direct and Alternating Inverse Spin Hall Effects in Magnetic Insulator-Normal Metal Bilayers

Paper III[79] contains a more rigorous and extended calculation for the FI | NM bilayer system: i) There were many permutations of the field configuration and surface anisotropy types that were left unexplored in Paper I,[77]; ii) we wanted to include the effects of a non-equilibrium spin accumulation in the normal metal, in that the back flow of spin angular momentum from the normal metal into the ferromagnetic insulator renormalizes the spin mixing conductance. (see Sec. 3.2.3); iii) measures for the AC and DC inverse spin Hall effects were also presented, which are related to the energy in the ferromagnet.

One of the things I wanted to remedy was that the dual wave number approach described in Sec. 4.1.1 (see Eq. (4.7)) served nicely as a first approximation, but it causes the calculated eigenmodes to slightly violate the bulk equation of motion if the pinning parameter, $d = LK_s/A$, becomes large in the in-plane geometry. The LLG equation demands precession, so that the two components, $X_Q(\xi)$ and $Y_Q(\xi)$ must have nodes at the exact same coordinates within the film. If the boundary conditions differ for the x and y component of $\mathbf{m}_Q$, the magnetization must have one dominant wavenumber in the bulk region, and then bend exponentially close to the interface to match the boundary conditions. This is easiest to show in the $QL \ll 1$ limit, when considering that the square of the dispersion relation

$$\Big(\frac{\omega}{\omega_M}\Big)^2 = \Big(\frac{\omega_H}{\omega_M} + \lambda_{\text{ex}}^2 k^2 + i\alpha\frac{\omega}{\omega_M}\Big)\Big(\frac{\omega_H}{\omega_M} + \lambda_{\text{ex}}^2 k^2 + \sin^2\theta + i\alpha\frac{\omega}{\omega_M}\Big), \tag{4.30}$$

where $\lambda_{\text{ex}} = \sqrt{8\pi\gamma^2 A/\omega_M^2}$, has a nontrivial degeneracy

$$\begin{aligned}\Big(\frac{\omega_H}{\omega_M} + \lambda_{\text{ex}}^2 k^2 + i\alpha\frac{\omega}{\omega_M}\Big)\Big(\frac{\omega_H}{\omega_M} + \lambda_{\text{ex}}^2 k^2 + \sin^2\theta + i\alpha\frac{\omega}{\omega_M}\Big) =\\ \Big(\frac{\omega_H}{\omega_M} + \lambda_{\text{ex}}^2 (i\kappa)^2 + i\alpha\frac{\omega}{\omega_M}\Big)\Big(\frac{\omega_H}{\omega_M} + \lambda_{\text{ex}}^2 (i\kappa)^2 + \sin^2\theta + i\alpha\frac{\omega}{\omega_M}\Big),\end{aligned} \tag{4.31}$$

given by

$$\lambda_{\text{ex}}^2 \kappa^2 = \sin^2\theta + \lambda_{\text{ex}}^2 k^2 + 2\frac{\omega_H}{\omega_M} \pm i2\alpha\omega(k)/\omega_M. \tag{4.32}$$

This makes it possible to write the dynamic magnetization as a sum of both a transverse standing wave term (oscillatory) and an exponential term. It is this exponential term that allows the magnetization components to bend in opposite directions to meet the restrictions posed by the surface anisotropy.

With this new form of the magnetization we were able to reduce the four boundary conditions down to one generic equation. This boundary condition can then be used for calculating the Gilbert damping renormalization in the weak pumping limit. With this we reproduced the unpinned, $d = 0$, results from Paper I as well as explored how surface anisotropies of different types influence the modes in the different field geometries. The main conclusions that were drawn were:

- An easy plane surface anisotropy causes a strongly localized surface wave to appear in the FVMSW geometry, which has a high renormalization of the Gilbert damping. Because of the perpendicular geometry, the DC spin accumulation does not induce an ISHE voltage in the normal metal, but the AC voltage exists and should be detectable.

- An easy axis surface anisotropy causes a localized surface wave to appear in the in-plane geometries. It is similar to the easy-plane result above, with the exception that the effective pinning parameter is smaller. This case is the one we explored with the two-wavenumber model in Paper I.

- All other modes are quenched to varying degrees by surface anisotropies.

4.4 Training and recovery behaviors of exchange bias in spin valves at high field sweep rates

Paper IV[80] is based on magnetoresistive measurements on a metallic spin valve structure performed while doing external magnetic field sweeps. The spin valve structure used a FeMn antiferromagnetic layer to pin the magnetization of the Co layer through the exchange bias effect.[93;16;94]

The exchange bias effect is an interface effect between an antiferromagnetic and a ferromagnet, where the uncompensated moments at the boundary pins the ferromagnets equilibrium direction to that of the antiferromagnet. The effect occurs for material combinations where the critical temperature of the antiferromagnet, the Néel temperature, is lower than the Curie temperature of the ferromagnet,[16] and the structure is cooled from above the Néel temperature in the presence of an applied external field. The antiferromagnet aligns itself with the ferromagnet during the cooling process due to the exchange interaction at the interface. If the antiferromagnet has a strong enough anisotropy, then it maintains its original alignment even during external field sweeps. The rigidity of the antiferromagnet causes a shift of the hysteresis loop of the ferromagnet, in that the antiferromagnet creates a biasing field through the exchange interaction.

The measurements in Paper IV were conducted by high sweep rate cycling of an externally applied magnetic field, while at the same time measuring the magnetoresistance of the spin valve. The magnetic field was ramped with a sawtooth shape, to produce a linear sweep rate. The repeated sweeps caused the coercive field of the spin valve to diminish for each cycle. This tendency is shown in the article to fit nicely to a the logarithm of the sweep number, n.

By performing N sweeps, then turning off the applied magnetic field for a stop time t, before continuing with additional sweeps to check the recovery rate. A quick recovery in the millisecond range of the exchange bias strength was observed. This recovery was shown to be the quickest for the highest sweep rate.

A Coordinate Transformations

The transformation for vectors from the $\xi\eta\zeta$ film coordinate system to the internal field xyz coordinate system described in Section 3.1 is given by an affine transformation matrix $\mathbf{T}$,

$$\mathbf{f}_{(xyz)} = \mathbf{T} \cdot \mathbf{f}_{(\xi\eta\zeta)}, \tag{A.1}$$

for some arbitrary vector $\mathbf{f}$. $\mathbf{T}$ is given by the concatenated rotation matrices

$$\mathbf{T} = \mathbf{R}_2 \cdot \mathbf{R}_1,$$

where $\mathbf{R}_1$ is a rotation ϕ around the ξ-axis, and $\mathbf{R}_2$ is a rotation $\theta - \frac{\pi}{2}$ around the new η-axis/y-axis. Hence

$$\mathbf{R}_1 = \begin{pmatrix} 1 & 0 & 0 \\ 0 & \cos\phi & -\sin\phi \\ 0 & \sin\phi & \cos\phi \end{pmatrix}, \tag{A.2}$$

$$\mathbf{R}_2 = \begin{pmatrix} \cos(\theta - \frac{\pi}{2}) & 0 & \sin(\theta - \frac{\pi}{2}) \\ 0 & 1 & 0 \\ -\sin(\theta - \frac{\pi}{2}) & 0 & \cos(\theta - \frac{\pi}{2}) \end{pmatrix} = \begin{pmatrix} \sin\theta & 0 & -\cos\theta \\ 0 & 1 & 0 \\ \cos\theta & 0 & \sin\theta \end{pmatrix}, \tag{A.3}$$

so that

$$\begin{aligned} \mathbf{T} &= \begin{pmatrix} \sin\theta & 0 & -\cos\theta \\ 0 & 1 & 0 \\ \cos\theta & 0 & \sin\theta \end{pmatrix} \begin{pmatrix} 1 & 0 & 0 \\ 0 & \cos\phi & -\sin\phi \\ 0 & \sin\phi & \cos\phi \end{pmatrix} \\ &= \begin{pmatrix} \sin\theta & -\cos\theta\sin\phi & -\cos\theta\cos\phi \\ 0 & \cos\phi & -\sin\phi \\ \cos\theta & \sin\theta\sin\phi & \sin\theta\cos\phi \end{pmatrix}. \end{aligned} \tag{A.4}$$

This transformation matrix consists of orthogonal transformations, so that the inverse transformation, transforming $xyz \rightarrow \xi\eta\zeta$, is just the transpose of $\mathbf{T}$

$$\mathbf{T}^{-1} = \mathbf{T}^{T} = \begin{pmatrix} \sin\theta & 0 & \cos\theta \\ -\cos\theta\sin\phi & \cos\phi & \sin\theta\sin\phi \\ -\cos\theta\cos\phi & -\sin\phi & \sin\theta\cos\phi \end{pmatrix}. \tag{A.5}$$

Bibliography

[1] Magne Saxegaard. *Scanning tunneling microscopy based point-contact measurements of nanoscale magnetic systems*. PhD thesis, Norwegian University of Science and Technology, 2010.

[2] John D. Jackson. *Classical Electrodynamics*. Wiley, 3rd edition, August 1998. ISBN 978-0471309321.

[3] The Story of the Intel® 4004. `http://www.intel.com/museum/archives/4004.htm`, . Accessed: 2017-04-08.

[4] G.E. Moore. Cramming more components onto integrated circuits. *Electronics*, 38(8):114–117, 1965.

[5] G.E. Moore. Cramming more components onto integrated circuits. *Proceedings of the IEEE*, 86(1):82–85, Jan 1998. doi: 10.1109/JPROC.1998.658762.

[6] G.E. Moore. Progress in digital integrated electronics. In *Electron Devices Meeting, 1975 International*, volume 21, pages 11–13, 1975.

[7] International Solid-State Circuits Conference (ISSCC) 2017 Trends. `http://isscc.org/doc/2017/ISSCC2017_TechTrends.pdf`. Accessed: 2017-04-25.

[8] Intel® 14nm Technology. `http://www.intel.com/content/www/us/en/silicon-innovations/intel-14nm-technology.html`, . Accessed: 2017-04-25.

[9] A. Pais. George Uhlenbeck and the Discovery of Electron Spin. *Physics Today*, (42):34–40, Dec 1989. doi: 10.1063/1.881186.

[10] Walther Gerlach and Otto Stern. Der experimentelle nachweis der richtungsquantelung im magnetfeld. *Zeitschrift für Physik*, 9(1):349–352, 1922. ISSN 0044-3328. doi: 10.1007/BF01326983.

[11] W. Heisenberg. Mehrkörperproblem und resonanz in der quantenmechanik. *Zeitschrift für Physik*, 38(6):411–426, 1926. doi: 10.1007/BF01397160.

[12] P. A. M. Dirac. On the theory of quantum mechanics. *Proceedings of the Royal Society of London. Series A, Containing Papers of a Mathematical and Physical Character*, 112(762):661–677, 1926. ISSN 09501207.

[13] M. N. Baibich, J. M. Broto, A. Fert, F. Nguyen Van Dau, F. Petroff, P. Etienne, G. Creuzet, A. Friederich, and J. Chazelas. Giant magnetoresistance of (001)fe/(001)cr magnetic superlattices. *Phys. Rev. Lett.*, 61:2472–2475, Nov 1988. doi: 10.1103/PhysRevLett.61.2472.

[14] G. Binasch, P. Grünberg, F. Saurenbach, and W. Zinn. Enhanced magnetoresistance in layered magnetic structures with antiferromagnetic interlayer exchange. *Phys. Rev. B*, 39:4828–4830, Mar 1989. doi: 10.1103/PhysRevB.39.4828.

[15] Sarah M Thompson. The discovery, development and future of gmr: The nobel prize 2007. *Journal of Physics D: Applied Physics*, 41(9): 093001, 2008.

[16] J Nogués and Ivan K Schuller. Exchange bias. *Journal of Magnetism and Magnetic Materials*, 192(2):203 – 232, 1999. doi: 10.1016/S0304-8853(98)00266-2.

[17] M. Julliere. Tunneling between ferromagnetic films. *Physics Letters A*, 54(3):225 – 226, 1975. ISSN 0375-9601. doi: 10.1016/0375-9601(75)90174-7.

[18] JC Slonczewski. Current-driven excitation of magnetic multilayers. *J. Magn. Magn. Mater.*, 159(1-2):L1–L7, Jun 1996. ISSN 0304-8853.

[19] L Berger. Emission of spin waves by a magnetic multilayer traversed by a current. *Physical Review B*, 54(13):9353–9358, Oct 1 1996. ISSN 0163-1829.

[20] A. Brataas, Y. Tserkovnyak, G.E.W. Bauer, and P.J. Kelly. Spin pumping and spin transfer. In S. Maekawa, S.O. Valenzuela, E. Saitoh, and T. Kimura, editors, *Spin Current*. Oxford University Press, 2012. ISBN 978-0199600380.

[21] D.C. Ralph and M.D. Stiles. Spin transfer torques. *J. Magn. Magn. Mater.*, 320(7):1190 – 1216, 2008. ISSN 0304-8853. doi: DOI:10.1016/j.jmmm.2007.12.019.

[22] Yaroslav Tserkovnyak, Arne Brataas, and Gerrit E. W. Bauer. Spin pumping and magnetization dynamics in metallic multilayers. *Phys. Rev. B*, 66:224403, Dec 2002. doi: 10.1103/PhysRevB.66.224403.

[23] Yaroslav Tserkovnyak, Arne Brataas, and Gerrit E. W. Bauer. Enhanced gilbert damping in thin ferromagnetic films. *Phys. Rev. Lett.*, 88:117601, Feb 2002. doi: 10.1103/PhysRevLett.88.117601.

[24] Arne Brataas, Yaroslav Tserkovnyak, Gerrit E. W. Bauer, and Bertrand I. Halperin. Spin battery operated by ferromagnetic resonance. *Phys. Rev. B*, 66:060404, Aug 2002. doi: 10.1103/PhysRevB.66.060404.

[25] Yaroslav Tserkovnyak, Arne Brataas, Gerrit E. W. Bauer, and Bertrand I. Halperin. Nonlocal magnetization dynamics in ferromagnetic heterostructures. *Rev. Mod. Phys.*, 77(4):1375–1421, Dec 2005. doi: 10.1103/RevModPhys.77.1375.

[26] A. Brataas, A. D. Kent, and H. Ohno. Current-induced torques in magnetic materials. *Nat. Mater.*, 11:372, 2012.

[27] A. V. Chumak, V. I. Vasyuchka, A. A. Serga, and B. Hillebrands. Magnon spintronics. *Nat Phys*, 11(6):453–461, Jun 2015. Review.

[28] V V Kruglyak, S O Demokritov, and D Grundler. Magnonics. *Journal of Physics D: Applied Physics*, 43(26):264001, 2010.

[29] B. Lenk, H. Ulrichs, F. Garbs, and M. Münzenberg. The building blocks of magnonics. *Physics Reports*, 507(4–5):107 – 136, 2011. ISSN 0370-1573. doi: 10.1016/j.physrep.2011.06.003.

[30] Y. Kajiwara, K. Harii, S. Takahashi, J. Ohe, K. Uchida, M. Mizuguchi, H. Umezawa, H. Kawai, K. Ando, K. Takanashi, S. Maekawa, and E. Saitoh. Transmission of electrical signals by spin-wave interconversion in a magnetic insulator. *Nature*, 464(7286):262–266, Mar 2010. ISSN 0028-0836. doi: 10.1038/nature08876.

[31] David J. Griffiths. *Introduction to Electrodynamics*. Pearson Prentice Hall, 3rd edition, 1999. ISBN 978-0138053260.

[32] W. Greiner, L. Neise, and H. Stöcker. *Thermodynamics and Statistical Mechanics*. Classical Theoretical Physics. Springer, 1st edition, 2000. ISBN 978-0387942995.

[33] David J. Griffiths. *Introduction to Quantum Mechanics*. Pearson Prentice Hall, 2nd edition, 2005. ISBN 978-1107179868.

[34] Stephen Blundell. *Magnetism in Condensed Matter (Oxford Master Series in Physics)*. Oxford University Press, 1st edition, Dec 2001. ISBN 978-0198505914.

[35] S. Elliot. *The Physics and Chemistry of Solids*. Wiley, 1st edition, 2006. ISBN 978-0471981954.

[36] Pierre Weiss. La variation du ferromagnétisme avec la température. *Comptes Rendus*, 143:1136, 1906.

[37] W. Heisenberg. Zur theorie der magnetostriktion und der magnetisierungskurve. *Zeitschrift für Physik*, 69(5):287–297, 1931. doi: 10.1007/BF01391350.

[38] M. A. Ruderman and C. Kittel. Indirect exchange coupling of nuclear magnetic moments by conduction electrons. *Phys. Rev.*, 96:99–102, Oct 1954. doi: 10.1103/PhysRev.96.99.

[39] Tadao Kasuya. A theory of metallic ferro- and antiferromagnetism on zener's model. *Progress of Theoretical Physics*, 16(1):45, 1956. doi: 10.1143/PTP.16.45.

[40] Clarence Zener. Interaction between the *d*-shells in the transition metals. ii. ferromagnetic compounds of manganese with perovskite

structure. *Phys. Rev.*, 82:403–405, May 1951. doi: 10.1103/PhysRev.82.403.

[41] H.A Kramers. L'interaction entre les atomes magnétogènes dans un cristal paramagnétique. *Physica*, 1(1):182 – 192, 1934. doi: 10.1016/S0031-8914(34)90023-9.

[42] P. W. Anderson. Antiferromagnetism. theory of superexchange interaction. *Phys. Rev.*, 79:350–356, Jul 1950. doi: 10.1103/PhysRev.79.350.

[43] J.H. Van Vleck. Recent developments in the theory of antiferromagnetism. *J. Phys. Radium*, (12):262 – 274, 1951. doi: 10.1051/jphysrad:01951001203026200.

[44] M.A. Gilleo. Superexchange interaction in ferrimagnetic garnets and spinels which contain randomly incomplete linkages. *Journal of Physics and Chemistry of Solids*, 13(1):33 – 39, 1960.

[45] M.A. Gilleo. Chapter 1 ferromagnetic insulators: Garnets. *Handbook of Ferromagnetic Materials*, 2:1 – 53, 1980. ISSN 1574-9304. doi: 10.1016/S1574-9304(05)80102-6.

[46] S. Geller and M.A. Gilleo. The crystal structure and ferrimagnetism of yttrium-iron garnet, Y3Fe2(FeO4)3. *Journal of Physics and Chemistry of Solids*, 3(1):30 – 36, 1957.

[47] C. Barry Carter and M. Grant Norton. *Using Magnetic Fields and Storing Data*, pages 617–639. Springer New York, New York, NY, 2013. ISBN 978-1-4614-3523-5. doi: 10.1007/978-1-4614-3523-5_33.

[48] Elmer E. Anderson. Molecular field model and the magnetization of yig. *Phys. Rev.*, 134:A1581–A1585, Jun 1964. doi: 10.1103/PhysRev.134.A1581.

[49] D.D. Stancil and Anil Prabhakar. *Spin Waves: Theory and Applications*. Springer, 2009.

[50] L.D. Landau and E.M. Lifshitz. On the theory of the dispersion of magnetic permeability in ferromagnetic bodies. *Phys. Z. Sowjetunion*, 8(153), 1935.

[51] T.L. Gilbert. Armour research foundation project no. a059. *unpublished*, 1956.

[52] T.L. Gilbert. A phenomenological theory of damping in ferromagnetic materials. *IEEE Trans. Magn.*, 40(3443), 2004.

[53] B A Kalinikos. Spectrum and linear excitation of spin waves in ferromagnetic films. *Sov. Phys. J.*, 24:719–731, 1981.

[54] B A Kalinikos and A N Slavin. Theory of dipole-exchange spin wave spectrum for ferromagnetic films with mixed exchange boundary conditions. *Journal of Physics C: Solid State Physics*, 19(35):7013, 1986.

[55] Christian Bayer, Joerg Jorzick, Sergej O. Demokritov, Andrei N. Slavin, Konstantin Y. Guslienko, Dmitry V. Berkov, Natalia L. Gorn, Mikhail P. Kostylev, and Burkard Hillebrands. Spin-wave excitations in finite rectangular elements. In *Spin Dynamics in Confined Magnetic Structures III*, volume 101 of *Topics in Applied Physics*, pages 57–103. Springer-Verlag Berlin, 2006.

[56] L.D. Landau and E.M. Lifshitz. *Electrodynamics of Continious Media*. Pergamon Press, 1960.

[57] Vladimir Cherepanov, Igor Kolokolov, and Victor L'vov. The saga of yig: Spectra, thermodynamics, interaction and relaxation of magnons in a complex magnet. *Physics Reports*, 229(3):81 – 144, 1993. doi: 10.1016/0370-1573(93)90107-O.

[58] J. R. Eshbach and R. W. Damon. Surface magnetostatic modes and surface spin waves. *Phys. Rev.*, 118:1208–1210, Jun 1960. doi: 10.1103/PhysRev.118.1208.

[59] R.W. Damon and J.R. Eshbach. Magnetostatic modes of a ferromagnet slab. *J. Phys. Chem. Solids*, 19(3-4):308 – 320, 1961. doi: DOI:10.1016/0022-3697(61)90041-5.

[60] R.C. Moul and M.G. Cottam. Theory of spin waves and response functions for heisenberg ferromagnetic films. *Journal of Physics C: Solid State Physics*, 16(7):1307, 1983.

[61] H. Puszkarski. Surface modes in magnetic thin films and in spin wave resonance. *IEEE Trans. Magn.*, 9(1):22–27, 1973. ISSN 0018-9464. doi: 10.1109/TMAG.1973.1067561.

[62] R. E. De Wames and T. Wolfram. Dipole-exchange spin waves in ferromagnetic films. *J. Appl. Phys.*, 41(3):987–993, 1970. doi: 10.1063/1.1659049.

[63] A A Serga, A V Chumak, and B Hillebrands. Yig magnonics. *J. Phys. D: Appl. Phys.*, 43(26):264002, 2010.

[64] J. E. Hirsch. Spin hall effect. *Phys. Rev. Lett.*, 83:1834–1837, Aug 1999. doi: 10.1103/PhysRevLett.83.1834.

[65] Shufeng Zhang. Spin hall effect in the presence of spin diffusion. *Phys. Rev. Lett.*, 85:393–396, Jul 2000. doi: 10.1103/PhysRevLett.85.393.

[66] Jairo Sinova, Sergio O. Valenzuela, J. Wunderlich, C. H. Back, and T. Jungwirth. Spin hall effects. *Rev. Mod. Phys.*, 87:1213–1260, Oct 2015. doi: 10.1103/RevModPhys.87.1213.

[67] X Jia, K Liu, Xie K, and G. E. W. B. Bauer. Spin transfer torque on magnetic insulators. *EPL*, 96:17005, 2011.

[68] P. Monod, H. Hurdequint, A. Janossy, J. Obert, and J. Chaumont. Giant electron spin-resonance transmission in cu ion implanted with mn. *Phys. Rev. Lett.*, 29:1327–1330, Nov 1972. doi: 10.1103/PhysRevLett.29.1327.

[69] R. H. Silsbee, A. Janossy, and P. Monod. Coupling between ferromagnetic and conduction-spin-resonance modes at a ferromagnetic normal-metal interface. *Phys. Rev. B*, 19:4382–4399, May 1979. doi: 10.1103/PhysRevB.19.4382.

[70] A. Janossy and P. Monod. Spin waves for single electrons in paramagnetic metals. *Phys. Rev. Lett.*, 37:612–615, Sep 1976. doi: 10.1103/PhysRevLett.37.612.

[71] Shigemi Mizukami, Yasuo Ando, and Terunobu Miyazaki. The study on ferromagnetic resonance linewidth for nm/80nife/nm (nm= cu, ta, pd and pt) films. *Japanese journal of applied physics*, 40(2R):580, 2001.

[72] R. Urban, G. Woltersdorf, and B. Heinrich. Gilbert damping in single and multilayer ultrathin films: Role of interfaces in nonlocal spin dynamics. *Phys. Rev. Lett.*, 87:217204, Nov 2001. doi: 10.1103/PhysRevLett.87.217204.

[73] E. Šimánek and B. Heinrich. Gilbert damping in magnetic multilayers. *Phys. Rev. B*, 67:144418, Apr 2003. doi: 10.1103/PhysRevB.67.144418.

[74] A. Brataas, Y. Tserkovnyak, and G.E.W. Bauer. Scattering theory of gilbert damping. *Phys. Rev. Lett.*, 101(3):037207, Jul 2008. doi: 10.1103/PhysRevLett.101.037207.

[75] G.T. Rado and J.R. Weertman. Spin-wave resonance in a ferromagnetic metal. *J. Phys. Chem. Solids*, 11(3-4):315–333, 1959. ISSN 0022-3697. doi: 10.1016/0022-3697(59)90233-1.

[76] R.A. Adams. *Calculus: A Complete Course*. Prentice Hall, 8th edition, 2013. ISBN 978-0321781079.

[77] André Kapelrud and Arne Brataas. Spin pumping and enhanced gilbert damping in thin magnetic insulator films. *Phys. Rev. Lett.*, 111:097602, Aug 2013. doi: 10.1103/PhysRevLett.111.097602.

[78] Hans Skarsvåg, André Kapelrud, and Arne Brataas. Spin waves in ferromagnetic insulators coupled via a normal metal. *Phys. Rev. B*, 90:094418, Sep 2014. doi: 10.1103/PhysRevB.90.094418.

[79] A. Kapelrud and A. Brataas. Spin pumping, dissipation, and direct and alternating inverse spin hall effects in magnetic-insulator/normal-metal bilayers. *Phys. Rev. B*, 95:214413, Jun 2017. doi: 10.1103/PhysRevB.95.214413.

[80] D.Z. Yang, A. Kapelrud, M. Saxegaard, and E. Wahlström. Training and recovery behaviors of exchange bias in feni/cu/co/femn spin

valves at high field sweep rates. *Journal of Magnetism and Magnetic Materials*, 324(19):3223 – 3226, 2012. ISSN 0304-8853. doi: 10.1016/j.jmmm.2012.05.002.

[81] B. Heinrich, C. Burrowes, E. Montoya, B. Kardasz, E. Girt, Young-Yeal Song, Yiyan Sun, and Mingzhong Wu. Spin pumping at the magnetic insulator (yig)/normal metal (au) interfaces. *Phys. Rev. Lett.*, 107:066604, Aug 2011. doi: 10.1103/PhysRevLett.107.066604.

[82] C. Burrowes, B. Heinrich, B. Kardasz, E. A. Montoya, E. Girt, Yiyan Sun, Young-Yeal Song, and Mingzhong Wu. Enhanced spin pumping at yttrium iron garnet/au interfaces. *Appl. Phys. Lett.*, 100(9):092403, 2012. doi: 10.1063/1.3690918.

[83] C. W. Sandweg, Y. Kajiwara, K. Ando, E. Saitoh, and B. Hillebrands. Enhancement of the spin pumping efficiency by spin-wave mode selection. *Appl. Phys. Lett.*, 97(252504), August 2010.

[84] C. W. Sandweg, Y. Kajiwara, A. V. Chumak, A. A. Serga, V. I. Vasyuchka, M. B. Jungfleisch, E. Saitoh, and B. Hillebrands. Spin pumping by parametrically excited exchange magnons. *Phys. Rev. Lett.*, 106:216601, May 2011. doi: 10.1103/PhysRevLett.106.216601.

[85] L. H. Vilela-Leao, C. Salvador, A. Azevedo, and S. M. Rezende. Unidirectional anisotropy in the spin pumping voltage in yttrium iron garnet/platinum bilayers. *Appl. Phys. Lett.*, 99(10):102505, 2011. doi: 10.1063/1.3631683.

[86] S. M. Rezende, R. L. Rodriguez-Suarez, M. M. Soares, L. H. Vilela-Leao, D. Ley Dominguez, and A. Azevedo. Enhanced spin pumping damping in yttrium iron garnet/pt bilayers. *Appl. Phys. Lett.*, 102(1): 012402, 2013. doi: 10.1063/1.4773993.

[87] Jiang Xiao and Gerrit E. W. Bauer. Spin-wave excitation in magnetic insulators by spin-transfer torque. *Phys. Rev. Lett.*, 108:217204, May 2012. doi: 10.1103/PhysRevLett.108.217204.

[88] M. B. Jungfleisch, V. Lauer, R. Neb, A. V. Chumak, and B. Hillebrands. Optimization of the yttrium iron garnet/platinum interface for spin

pumping-based applications. *Appl. Phys. Lett.*, 103(2):022411, 2013. doi: 10.1063/1.4813315.

[89] Z. Qiu, K. Ando, K. Uchida, Y. Kajiwara, R. Takahashi, H. Nakayama, T. An, Y. Fujikawa, and E. Saitoh. Spin mixing conductance at a well-controlled platinum/yttrium iron garnet interface. *Applied Physics Letters*, 103(9):092404, 2013. doi: 10.1063/1.4819460.

[90] E.C. Titchmarsh. *Eigenfunction Expansions Assosciated with Second-Order Differential Equations*. Oxford at the Clarendon Press, 2nd edition, 1962.

[91] J.H. Mathews and K.K. Fink. *Numerical Methods Using Matlab*. Prentice Hall, 4th edition, 2004. ISBN 978-0130652485.

[92] W.H. Press, S.A. Teukolsky, W.T. Vetterling, and B.P. Flannery. *Numerical Recipies*. Cambridge University Press, 3rd edition, 2007.

[93] W. H. Meiklejohn and C. P. Bean. New magnetic anisotropy. *Phys. Rev.*, 102:1413–1414, Jun 1956. doi: 10.1103/PhysRev.102.1413.

[94] A.E. Berkowitz and Kentaro Takano. Exchange anisotropy — a review. *Journal of Magnetism and Magnetic Materials*, 200(1–3):552 – 570, 1999. doi: 10.1016/S0304-8853(99)00453-9.

Part II

Papers

Paper 1

Spin Pumping and Enhanced Gilbert Damping in Thin Magnetic Insulator Films

Phys. Rev. Lett. 111, 097602 (2013) - Published August 27, 2013

Spin Pumping and Enhanced Gilbert Damping in Thin Magnetic Insulator Films

André Kapelrud and Arne Brataas

Department of Physics, Norwegian University of Science and Technology, NO-7491 Trondheim, Norway

(Received 20 March 2013; published 27 August 2013; publisher error corrected 5 September 2013)

Precessing magnetization in a thin-film magnetic insulator pumps spins into adjacent metals; however, this phenomenon is not quantitatively understood. We present a theory for the dependence of spin pumping on the transverse mode number and in-plane wave vector. For long-wavelength spin waves, the enhanced Gilbert damping for the transverse mode volume waves is twice that of the macrospin mode, and for surface modes, the enhancement can be ten or more times stronger. Spin pumping is negligible for short-wavelength exchange spin waves. We corroborate our analytical theory with numerical calculations in agreement with recent experimental results.

DOI: 10.1103/PhysRevLett.111.097602 PACS numbers: 76.50.+g, 75.30.Ds, 75.70.−i, 75.76.+j

Metallic spintronics have been tremendously successful in creating devices that both fulfill significant market needs and challenge our understanding of spin transport in materials. Topics that are currently of great interest are spin transfer and spin pumping [1–3], spin Hall effects [4], and combinations thereof for use in nonvolatile memory, oscillator circuits, and spin wave logic devices. A recent experimental demonstration showing that spin transfer and spin pumping can be as effective in magnetic insulators as in metallic ferromagnetic systems was surprising and has initiated a new field of inquiry [5].

In magnetic insulators, no moving charges are present, and in some cases, the dissipative losses associated with the magnetization dynamics are exceptionally low. Nevertheless, when a magnetic insulator is placed in contact with a normal metal, magnetization dynamics induce spin pumping, which in turn causes angular momentum to be dumped to the metal's itinerant electron system. Because of this nonlocal interaction, the magnetization losses become enhanced. Careful experimental investigations of spin pumping and the associated enhanced magnetization dissipation were recently performed, demonstrating that the dynamic coupling between the magnetization dynamics in magnetic insulators and spin currents in adjacent normal metals is strong. Importantly, in magnetic insulators, an exceptionally low intrinsic damping combined with good material control has enabled the study of spin pumping for a much larger range of wave vectors than has previously been obtained in metallic ferromagnets [5–14].

In thin-film ferromagnets, the magnetization dynamics are strongly affected by the long-range dipolar interaction, which has both static and spatiotemporal contributions. This yields different types of spin waves. When the in-plane wavelength is comparable to the film thickness or greater, the long-range dipolar interaction causes the separation of the spin-wave modes into three classes depending on the relative orientation of the applied external field, in relation to the film normal, and the spin-wave propagation direction [15–20]. These spin waves are classified according to their dispersion and transverse magnetization distribution as forward volume magnetostatic spin waves (FVMSWs) when the external field is out of plane, backward volume magnetostatic spin waves (BVMSWs) when the external field is in-plane and along the direction of propagation, and magnetostatic surface waves (MSSWs) when the external field is in-plane but perpendicular to the direction of propagation. In volume waves, the magnetic excitation is spatially distributed across the entire film, while surface modes are localized near one of the surfaces. "Backward" waves have a frequency dispersion with a negative group velocity for some wavelengths. While these spin waves have been studied in great detail over the last decades, the effect of an adjacent normal metal on these waves has only recently been investigated.

Experimentally, it has been observed that spin pumping differs for FVMSWs, BVMSWs, and MSSWs and that it depends on the spin-wave wavelength [6,8,9,12–14]. Recent experiments [8] have demonstrated that the magnetization dissipation is larger for surface spin waves in which the excitation amplitude is localized at the magnetic insulator–normal-metal interface. To utilize spin pumping from thin-film magnetic insulators into adjacent normal metals, a coherent theoretical picture of these experimental findings must be developed and understood, which is the aim of our work.

In this Letter, we present a theory for energy dissipation from spin-wave excitations in a ferromagnetic insulator (FI) thin film via spin pumping when the ferromagnetic insulator layer is in contact with a normal metal (NM). To this end, consider a thin-film magnetic insulator of thickness L on an insulating substrate with a normal metal capping (see Figure 1). We consider a normal metal such as Pt at equilibrium, where there is rapid spin relaxation and no back flow of spin currents to the magnetic insulator. The normal metal is then a perfect spin sink and remains in equilibrium even though spins are pumped into it.

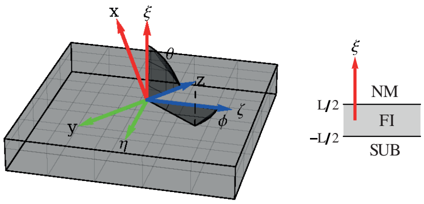

(a) (b)

FIG. 1 (color online). (a) A thin-film magnetic insulator of thickness L in its coordinate system; ξ is the normal axis, the infinite $\eta\zeta$ plane is coplanar with the interfaces, and the spin waves propagate along the ζ axis. The internal field and saturation magnetization are along the z axis. The y axis is always kept in-plane, and the x axis is selected such that the x, y, and z axes form a right-handed coordinate system. (b) A cross section showing the material stack.

The magnetization dynamics are described by the Landau-Lifshitz-Gilbert (LLG) equation [21] with a torque originating from the FI-NM interfacial spin pumping [22]

$$\dot{\mathbf{M}} = -\gamma \mathbf{M}\times\mathbf{H}_{\text{eff}} + \frac{\alpha}{M_S}\mathbf{M}\times\dot{\mathbf{M}} + \boldsymbol{\tau}_{\text{sp}}, \tag{1}$$

where α is the Gilbert damping coefficient, M_S is the saturation magnetization, γ is the gyromagnetic ratio, $\mathbf{H}_{\text{eff}}$ is the effective field including the external field, exchange energy, surface anisotropy energy, and static and dynamic demagnetization fields.

Spin pumping through interfaces between magnetic insulators and normal metals gives rise to a spin-pumping induced torque that is described as [2]

$$\boldsymbol{\tau}_{\text{sp}} = \frac{\gamma\hbar^2}{2e^2M_S^2}g_\perp\delta\left(\xi-\frac{L}{2}\right)\mathbf{M}\times\dot{\mathbf{M}}, \tag{2}$$

where $g_\perp$ is the transverse spin ("mixing") conductance per unit area at the FI-NM interface, and e is the electron charge. We disregard the imaginary part of the mixing conductance because this part has been found to be small at FI-NM interfaces [12]. In addition, the imaginary part is qualitatively less important and only renormalizes the gyromagnetic ratio.

Assuming only uniform magnetic excitations, "macrospin" excitations, the effect of spin pumping on the magnetization dissipation is well known [2,3]. Spin pumping leads to enhanced Gilbert damping, $\alpha \to \alpha + \Delta\alpha_{\text{macro}}$, which is proportional to the FI-NM cross section because more spin current is then pumped out, but inversely proportional to the volume of the ferromagnet that controls the total magnetic moment,

$$\Delta\alpha_{\text{macro}} = \frac{\gamma\hbar}{4\pi L M_S}\frac{h}{e^2}g_\perp. \tag{3}$$

Thus, the enhanced Gilbert damping due to spin pumping is inversely proportional to the film thickness L and is important for thin-film ferromagnets. However, a "macrospin" excitation, or the ferromagnetic resonance (FMR) mode, is only one out of many types of magnetic excitations in thin films. The effect of spin pumping on the other modes is not known, and we provide the first analytical results for this important question, which is further supported and complemented by numerical calculations.

We consider weak magnetic excitations around a homogenous magnetic ground state pointing along the direction of the internal field $\mathbf{H}_i = H_i\hat{\mathbf{z}}$, which is the combination of the external applied field and the static demagnetizing field [19]. We may then expand $\mathbf{M} = M_S\hat{\mathbf{z}} + \mathbf{m}_{Q,xy}(\xi)e^{i(\omega t - Q\zeta)}$, where $\mathbf{m}_{Q,xy}\cdot\hat{\mathbf{z}} = 0$, $|\mathbf{m}_{Q,xy}| \ll M_S$, and Q is the in-plane wave number in the ζ direction. The angle θ between the film normal and $\hat{\mathbf{z}}$ and the in-plane projected angle ϕ between $\hat{\mathbf{z}}$ and $\hat{\boldsymbol{\zeta}}$ are shown in Figure 1.

Following the linearization approach of the LLG equation (1) as in Ref. [19], we arrive at a two-dimensional integro-differential equation of the dynamic magnetization (in the xy plane) in the film's transverse coordinate ξ,

$$\left\{i\frac{\omega}{\omega_M}\begin{pmatrix}\alpha & -1\\ 1 & \alpha\end{pmatrix} + \mathbb{1}\left(\frac{\omega_H}{\omega_M}+8\pi\frac{\gamma^2A}{\omega_M^2}\left[Q^2-\frac{d^2}{d\xi^2}\right]\right)\right\}\mathbf{m}_{Q,xy}(\xi) = \int_{-(L/2)}^{L/2} d\xi'\hat{\mathcal{G}}_{xy}(\xi-\xi')\mathbf{m}_{Q,xy}(\xi'), \tag{4}$$

where ω is the spin-wave eigenfrequency, A is the exchange stiffness, $\omega_H = \gamma H_i$, $\omega_M = 4\pi\gamma M_S$, and $\hat{\mathcal{G}}_{xy}$ is the dipole-dipole field interaction tensor, which fulfills the boundary conditions resulting from Maxwell's equations (see Ref. [23]).

The eigensystem must be supplemented by boundary conditions that account for spin pumping and surface anisotropy. These boundary conditions are obtained by integrating Eq. (1) over the interface [24] and expanding to the lowest order in the dynamic magnetization. When an out-of-plane easy axis surface anisotropy is present, the boundary conditions are

$$\left(L\frac{\partial}{\partial\xi} + i\omega\chi + \frac{LK_s}{A}\cos(2\theta)\right)m_{Q,x}(\xi)|_{\xi=L/2} = 0, \tag{5a}$$

$$\left(L\frac{\partial}{\partial\xi} + i\omega\chi + \frac{LK_s}{A}\cos^2(\theta)\right)m_{Q,y}(\xi)|_{\xi=L/2} = 0, \tag{5b}$$

where K_s is the surface anisotropy energy with units $\text{erg}\,\text{cm}^{-2}$ and $\chi = L\hbar^2 g_\perp/4Ae^2$ is a parameter relating the exchange stiffness and the spin mixing conductance ($[\chi] = \text{s}$). The boundary condition at the magnetic insulator–substrate interface might also be affected by surface anisotropy. Since our focus is on spin pumping at the other surface, we disregard this complication as a first approximation and set $\chi \to 0$ at $\xi = -L/2$.

A mathematical challenge induced by spin pumping arises because the second term in the linearized boundary condition (5) is proportional to the eigenvalue ω such that the eigenfunctions cannot simply be expanded in the set of eigenfunctions obtained when there is no spin-pumping or dipolar interaction. Instead, we follow an alternative analytical route for small and large wave vectors. Furthermore, we numerically determine the eigenmodes with a custom-tailored technique, where we discretize the differential equation (4), include the spin-pumping boundary conditions (5), and transform the resulting equations into an eigenvalue problem in ω [25].

Let us now outline how we obtain analytical results for small $QL \ll 1$ and large $QL \gg 1$ wave vectors. First, we consider the case of vanishing surface anisotropy and compute the renormalization of the Gilbert damping for the resulting modes. Next, we demonstrate that the surface anisotropy creates a surface wave with a comparably large enhancement of the Gilbert component.

When $QL \ll 1$, the convolution integral on the right-hand side of Eq. (4) only contains the homogeneous demagnetization field. The magnetization is then a transverse standing wave $\mathbf{m}_{Q,xy}(e^{ik\xi} + e^{-ik\xi+\phi})$, where k is a transverse wave number, ϕ is a phase determined by the boundary condition at the lower interface, and the two-dimensional coefficient vector $\mathbf{m}_{Q,xy}$ allows for elliptical polarization in the xy plane.

By employing exchange-only boundary conditions [24] at the lower interface and using Eq. (5) with $K_s = 0$ on the upper interface, the transverse wave number k is determined by $kL \tan kL = i\omega\chi$. Together with the bulk dispersion relation $\omega = \omega(k)$, calculated from Eq. (4), this expression allows us to calculate the magnetic excitation dispersion relation parameterized by the film thickness, the Gilbert damping α, and the transverse conductance $g_\perp$.

When spin pumping is weak, $\omega\chi$ is small, and the solutions of the transcendental equation can be expanded around the solutions obtained when there is no spin pumping, $kL = n\pi$, where n is an integer. When $n \neq 0$, we expand to first order in kL and obtain $kL \approx n\pi + i\omega\chi/(n\pi)$. When $n = 0$, we must perform a second-order expansion in terms of kL around 0, which results in $(kL)^2 \approx i\omega\chi$. Using these relations in turn to eliminate k from the bulk dispersion relation while maintaining our linear approximation in small terms and solving for ω, we obtain complex eigenvalues, where the imaginary part is proportional to a renormalized Gilbert damping parameter, $\alpha^* = \alpha + \Delta\alpha$. When $n = 0$, our results agree with the spin-pumping enhanced Gilbert damping of the macrospin (FMR) mode derived in Ref. [2] [see Eq. (3)], $\Delta\alpha_0 = \Delta\alpha_{\text{macro}}$. When $n \neq 0$, we compute

$$\Delta\alpha_n = 2\Delta\alpha_{\text{macro}}. \tag{6}$$

These new results indicate that *all* higher transverse volume modes have an enhanced magnetization dissipation that is twice that of the macrospin mode. Thus, counterintuitively, with the exception of the macrospin mode, increasingly higher-order standing-wave transverse spin-wave modes have precisely the same enhanced Gilbert damping.

Next, let us discuss spin pumping for surface waves induced by the presence of surface anisotropy. When $K_s \neq 0$, the lowest volume excitation mode develops into a spatially localized surface wave. Expanding the expression for the localized wave to the highest order in LK_s/A, we determine after some algebra that the resulting enhancement of the Gilbert damping is

$$\Delta\alpha_{n=0} = \frac{\gamma\hbar K_s}{4\pi M_s A}\frac{h}{e^2}g_\perp\frac{\omega_H}{\omega_M}\left[\frac{\omega_H}{\omega_M} + \frac{1}{2} - \frac{K_s^2}{4\pi M_s^2 A}\right]^{-1}. \tag{7}$$

Comparing Eqs. (7) and (6), we see that for large surface anisotropy $LK_s/A \gg 1$, the spin-pumping-induced enhanced Gilbert damping is independent of L. This result occurs because a large surface anisotropy induces a surface wave with a decay length A/K_s, which replaces the actual physical thickness L as the effective thickness of the magnetic excitations, i.e., for surface waves $L \rightarrow A/K_s$ in the expression for the enhanced Gilbert damping of Eq. (3). This replacement implies that the enhanced Gilbert damping is much larger for surface waves because the effective magnetic volume decreases. For typical values of A and K_s, we obtain an effective length $A/K_s \sim 10$ nm. Compared with the film thicknesses used in recent experiments, this value corresponds to a tenfold or greater increase in the enhancement of the Gilbert damping. In contrast, for the volume modes ($n \neq 0$), we note from Eq. (5) that the dynamic magnetization will decrease at the FI-NM interface due to the surface anisotropy; hence, $\Delta\alpha$ decreases compared with the results of Eq. (6).

Finally, we can also demonstrate that for large wave vectors $QL \gg 1$, the excitation energy mostly arises from the in-plane (longitudinal) magnetization texture gradient. Consequently, spin pumping, which pumps energy out of the magnetic system due to the transverse gradient of the magnetization texture, is much less effective and decays as $1/(QL)^2$ with respect to Eq. (3).

To complement our analytical study, we numerically computed the eigenfrequencies $\omega_n(Q)$. The energy is determined by the real part of $\omega_n(Q)$, while $\text{Im}\,\omega_n(Q)$ determines the dissipation rate and hence the spin-pumping contribution. Recent experiments [6,11,13,14] on controlling and optimizing the ferrimagnetic insulator yttrium iron garnet (YIG) have estimated that the mixing conductances of both YIG-Au and YIG-Pt bilayers are in the range of $g_\perp h/e^2 \sim 0.02$–3.43×10^{15} cm^{-2}. We use $g_\perp h/e^2 = 1.2 \times 10^{14}$ cm^{-2} from Ref. [6] in this work. All of our results can be linearly rescaled with other values of the mixing conductance. In the following section, we also use $A = 2.9 \times 10^{-8}$ erg/cm, $K_s = 0.05$ erg/cm^2, $L = 100$ nm, $4\pi M_S = 1750$ G, and $\alpha = 3 \times 10^{-4}$.

To distinguish the spin-pumping contribution $\Delta\alpha$ from the magnetization dissipation due to intrinsic Gilbert damping α, we first compute the eigenvalues, ω_d, with

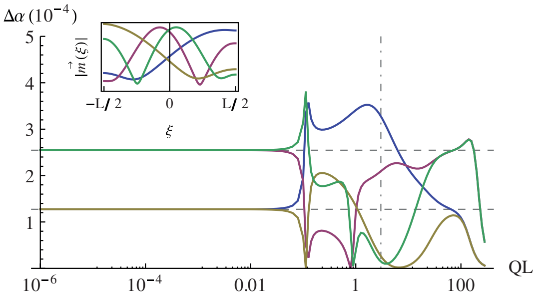

FIG. 2 (color online). $\Delta\alpha$ versus wave vector for the MSSW geometry ($\theta = \phi = \pi/2$) for the four lowest eigenvalues. Inset: magnitudes of eigenvectors (in arbitrary units) across the film at $QL = 1.5$.

intrinsic Gilbert damping, $\alpha \neq 0$, and no spin pumping, $g_\perp = 0$. Second, we compute the eigenvalues $\omega_{\rm sp}$ with dissipation arising from spin pumping only, $\alpha = 0$ and $g_\perp \neq 0$. Because $\mathrm{Im}\omega_d \propto \alpha$, we define a measure of the spin-pumping-induced effective Gilbert damping as $\Delta\alpha = \alpha\, \mathrm{Im}\omega_{\rm sp}/\mathrm{Im}\omega_d$.

We first consider the case of no surface anisotropy. Figure 2 shows the spin-pumping-enhanced Gilbert damping $\Delta\alpha$ as a function of the product of the in-plane wave vector and the film thickness QL in the MSSW geometry. In the long-wavelength limit, $QL \ll 1$, the numerical result agrees precisely with our analytical results of Eq. (5). The enhanced Gilbert damping of all higher transverse modes is exactly twice that of the macrospin mode. In the dipole-exchange regime, for intermediate values of QL, the dipolar interaction causes a small asymmetry in the eigenvectors for positive and negative eigenfrequencies because modes traveling in opposite directions have different magnitudes of precession near the FI-NM interface [26], and spin pumping from these modes therefore differ. This phenomenon also explains why the enhanced damping, $\Delta\alpha$, splits into different branches in this regime, as shown in Fig. 2. For exchange spin waves, $QL \gg 1$, the exchange interaction dominates the dipolar interaction and removes mode asymmetries. We also see that $\Delta\alpha \to 0$ for large QL, in accordance with our analytical theory.

Figure 3 shows $\Delta\alpha$ for the BVMSW geometry. The eight first modes are presented; however, as no substantial asymmetry exists between eigenmodes traveling in different directions, the modes have the same pairwise renormalization of α. This symmetry occurs because the direction of the internal field coincides with the direction of propagation. As in the previous case, the dipolar interaction causes a slight shift in the eigenvectors in the intermediate QL regime, thereby altering $\Delta\alpha$ from that of Eq. (5).

Figure 4 shows $\Delta\alpha$ for the MSSW geometry but with surface anisotropy at the FI-NM interface. As expected from our analytical results, surface anisotropy induces two localized surface modes with a tenfold larger enhancement of $\Delta\alpha$ compared with the volume modes. The horizontal dashed line in Figure 4 indicates the analytical result for the enhanced Gilbert damping of the $n \neq 0$ modes when $K_s = 0$. For the volume modes, it is clear that the eigenvectors have a lower magnitude closer to the FI-NM interface and that $\Delta\alpha$ is lower compared with the case of $K_s = 0$, which is consistent with our analytical analysis.

Our results also agree with recent experiments. Sandweg *et al.* [8] found that spin pumping is significantly higher for surface spin waves compared with volume spin-wave modes. In addition, in Ref. [9], exchange waves were observed to be less efficient at pumping spins than dipolar spin waves, which is consistent with our results. Furthermore, our results are consistent with the theoretical finding that spin-transfer torques preferentially excite surface spin waves with a critical current inversely proportional to the penetration depth [27].

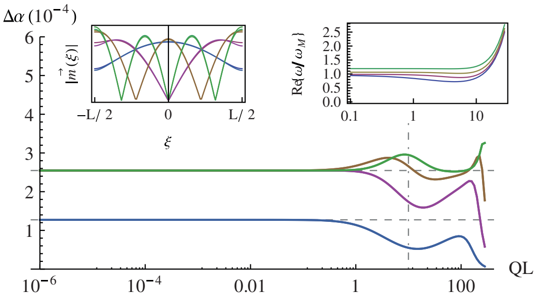

FIG. 3 (color online). $\Delta\alpha$ versus wave vector for the BVMSW geometry ($\theta = \pi/2$ and $\phi = 0$). Left inset: Magnitude of eigenvectors (in arbitrary units) across the film when $QL = 1.5$. Right inset: the real part of the dispersion relation for the same modes.

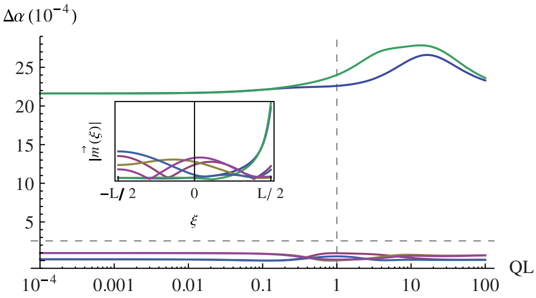

FIG. 4 (color online). $\Delta\alpha$ versus wave vector for the MSSW geometry ($\theta = \phi = \pi/2$) with surface anisotropy added at the interface. Inset: magnitudes of eigenvectors (in arbitrary units) across the film.

In conclusion, we have analyzed how spin pumping causes a wave-vector-dependent enhancement of the Gilbert damping in thin magnetic insulators in contact with normal metals. In the long-wavelength limit, our analytical results demonstrate that the enhancement of the Gilbert damping for all higher-order volumetric modes is twice as large as that of a macrospin excitation. Importantly, surface anisotropy-pinned modes have a Gilbert renormalization that is significantly and linearly enhanced by the ratio LK_s/A.

A. Kapelrud would like to thank G. E. W. Bauer for his hospitality at TU Delft. This work was supported by EU-ICT-7 Contract No. 257159 “MACALO.”

[1] A. Brataas, A. D. Kent, and H. Ohno, Nat. Mater. **11**, 372 (2012).
[2] Y. Tserkovnyak, A. Brataas, and G. E. W. Bauer, Phys. Rev. Lett. **88**, 117601 (2002).
[3] Y. Tserkovnyak, A. Brataas, G. E. W. Bauer, and B. I. Halperin, Rev. Mod. Phys. **77**, 1375 (2005).
[4] T. Jungwirth, J. Wunderlich, and K. Olejnik, Nat. Mater. **11**, 382 (2012).
[5] Y. Kajiwara, K. Harii, S. Takahashi, J. Ohe, K. Uchida, M. Mizuguchi, H. Umezawa, H. Kawai, K. Ando, K. Takanasahi, S. Maekawa, and E. Saitoh, Nature (London) **464**, 262 (2010).
[6] B. Heinrich, C. Burrowes, E. Montoya, B. Kardasz, E. Girt, Y.-Y. Song, Y. Sun, and M. Wu, Phys. Rev. Lett. **107**, 066604 (2011).
[7] C. Burrowes, B. Heinrich, B. Kardasz, E. A. Montoya, E. Girt, Y. Sun, Y.-Y. Song, and M. Wu, Appl. Phys. Lett. **100**, 092403 (2012).
[8] C. W. Sandweg, Y. Kajiwara, K. Ando, E. Saitoh, and B. Hillebrands, Appl. Phys. Lett. **97**, 252504 (2010).
[9] C. W. Sandweg, Y. Kajiwara, A. V. Chumak, A. A. Serga, V. I. Vasyuchka, M. B. Jungfleisch, E. Saitoh, and B. Hillebrands, Phys. Rev. Lett. **106**, 216601 (2011).
[10] L. H. Vilela-Leao, A. A. C. Salvador, and S. M. Rezende, Appl. Phys. Lett. **99**, 102505 (2011).
[11] S. M. Rezende, R. L. Rodriguez-Suarez, M. M. Soares, L. H. Vilela-Leao, D. L. Dominguez, and A. Azevedo, Appl. Phys. Lett. **102**, 012402 (2013).
[12] X. Jia, K. Liu, X. K, and G. E. W. B. Bauer, Europhys. Lett. **96**, 17005 (2011).
[13] M. B. Jungfleisch, V. Lauer, R. Neb, A. V. Chumak, and B. Hillebrands, arXiv:1302.6697.
[14] Z. Qiu, K. Ando, K. Uchida, Y. Kajiwara, R. Takahashi, T. An, Y. Fujikawa, and E. Saitoh, arXiv:1302.7091.
[15] J. R. Eshbach and R. W. Damon, Phys. Rev. **118**, 1208 (1960).
[16] R. Damon and J. Eshbach, J. Phys. Chem. Solids **19**, 308 (1961).
[17] H. Puszkarski, IEEE Trans. Magn. **9**, 22 (1973).
[18] R. E. D. Wames and T. Wolfram, J. Appl. Phys. **41**, 987 (1970).
[19] B. A. Kalinikos and A. N. Slavin, J. Phys. C **19**, 7013 (1986).
[20] A. Serga, A. Chumak, and B. Hillebrands, J. Phys. D **43**, 264002 (2010).
[21] T. Gilbert, Phys. Rev. **100**, 1243 (1955); currently this reference is available only in print format.
[22] Gaussian (cgs) units are employed throughout.
[23] B. A. Kalinikos, Sov. Phys. J. **24**, 718 (1981).
[24] G. Rado and J. Weertman, J. Phys. Chem. Solids **11**, 315 (1959).
[25] A. Kapelrud and A. Brataas (unpublished).
[26] Z. Wang, Y. Sun, M. Wu, V. Tiberkevich, and A. Slavin, Phys. Rev. Lett. **107**, 146602 (2011).
[27] J. Xiao and G. E. W. Bauer, Phys. Rev. Lett. **108**, 217204 (2012).

Paper 2

Spin waves in ferromagnetic insulators coupled via a normal metal

Phys. Rev. B 90, 094418 (2014) - Published September 26, 2014

PHYSICAL REVIEW B **90**, 094418 (2014)

Spin waves in ferromagnetic insulators coupled via a normal metal

Hans Skarsvåg,[*] André Kapelrud, and Arne Brataas
Department of Physics, Norwegian University of Science and Technology, NO-7491 Trondheim, Norway

(Received 2 July 2014; published 26 September 2014)

Herein, we study spin-wave dispersion and dissipation in a ferromagnetic insulator–normal metal–ferromagnetic insulator system. Long-range dynamic coupling because of spin pumping and spin transfer lead to collective magnetic excitations in the two thin-film ferromagnets. In addition, the dynamic dipolar field contributes to the interlayer coupling. By solving the Landau-Lifshitz-Gilbert-Slonczewski equation for macrospin excitations and the exchange-dipole volume as well as surface spin waves, we compute the effect of the dynamic coupling on the resonance frequencies and linewidths of the various modes. The long-wavelength modes may couple acoustically or optically. In the absence of spin-memory loss in the normal metal, the spin-pumping-induced Gilbert damping enhancement of the acoustic mode vanishes, whereas the optical mode acquires a significant Gilbert damping enhancement, comparable to that of a system attached to a perfect spin sink. The dynamic coupling is reduced for short-wavelength spin waves, and there is no synchronization. For intermediate wavelengths, the coupling can be increased by the dipolar field such that the modes in the two ferromagnetic insulators can couple despite possible small frequency asymmetries. The surface waves induced by an easy-axis surface anisotropy exhibit much greater Gilbert damping enhancement. These modes also may acoustically or optically couple, but they are unaffected by thickness asymmetries.

DOI: 10.1103/PhysRevB.90.094418 PACS number(s): 76.50.+g, 75.30.Ds, 75.70.−i, 75.76.+j

I. INTRODUCTION

The dynamic magnetic properties of thin-film ferromagnets have been extensively studied for several decades [1,2]. Thin-film ferromagnets exhibit a rich variety of spin-wave modes because of the intricate interplay among the exchange and dipole interactions and the material anisotropies. In ferromagnetic insulators (FIs), these modes are especially visible; the absence of disturbing electric currents leads to a clear separation of the magnetic behavior. Furthermore, the dissipation rates in insulators are orders of magnitude lower than those in their metallic counterparts; these low dissipation rates enable superior control of traveling spin waves and facilitate the design of magnonic devices [3]. In spintronics, there has long been considerable interest in giant magnetoresistance, spin-transfer torques, and spin pumping in hybrid systems of normal metals and metallic ferromagnets (MFs) [4–7]. The experimental demonstration that spin transfer and spin pumping are also active in normal metals in contact with insulating ferromagnets has generated a renewed interest in and refocused attention on insulating ferromagnets, of which yttrium iron garnet (YIG) continues to be the prime example [8–19]. In ferromagnetic insulators, current-induced spin-transfer torques from a neighboring normal metal (NM) that exhibits out-of-equilibrium spin accumulation may manipulate the magnetization of the insulator and excite spin waves [8,20,21,22]. The out-of-equilibrium spin accumulation of the normal metal may be induced via the spin Hall effect or by currents passing through other adjacent conducting ferromagnets. Conversely, excited spin waves pump spins into adjacent NMs, and this spin current may be measured in terms of the inverse spin Hall voltages or by other conducting ferromagnets [8–14]. The magnetic state may also be measured via the spin Hall magnetoresistance [16–19,24,25]. Because of these developments, magnetic information in ferromagnetic insulators may be electrically injected, manipulated, and detected. Importantly, an FI-based spintronic device may efficiently transport electric information carried by spin waves over long distances [15] without any excessive heating. The spin-wave decay length can be as long as centimeters in YIG films [23]. These properties make FI-NM systems ideal devices for the exploration of novel spintronic phenomena and possibly also important for future spintronic applications. Magnonic devices also offer advantages such as rapid spin-wave propagation, frequencies ranging from GHz to THz, and the feasibility of creating spin-wave logic devices and magnonic crystals with tailored spin-wave dispersions [26]. To utilize the desirable properties of FI-NM systems, such as the exceptionally low magnetization-damping rate of FIs, it is necessary to understand how the magnetization dynamics couple to spin transport in adjacent normal metals. The effective damping of the uniform magnetic mode of a thin-film FI is known to significantly increase when the FI is placed in contact with an NM. This damping enhancement is caused by the loss of angular momentum through spin pumping [27–31]. Recent theoretical work has also predicted the manner in which the Gilbert damping for other spin-wave modes should become renormalized [32]. For long-wavelength spin waves, the Gilbert damping enhancement is twice as large for transverse volume waves as for the macrospin mode, and for surface modes, the enhancement can be ten times stronger or more. Spin pumping has been demonstrated, both experimentally [9] and theoretically [32], to be suppressed for short-wavelength exchange spin waves. A natural next step is to investigate the magnetization dynamics of more complicated FI-NM heterostructures. In ferromagnetic metals, it is known that spin pumping and spin-transfer torques generate a long-range dynamic interaction between magnetic films separated by normal-metal layers [33]. The effect of this long-range dynamic interaction on homogeneous macrospin excitations can be measured by ferromagnetic resonance. The

---

[*] hans.skarsvag@ntnu.no

combined effects of spin pumping and spin-transfer torque lead to an appreciable increase in the resonant linewidth when the resonance fields of the two films are far apart and to a dramatic narrowing of the linewidth when the resonant fields approach each other [33]. This behavior occurs because the excitations in the two films couple acoustically (in phase) or optically (out of phase). We will demonstrate that similar, though richer because of the complex magnetic modes, phenomena exist in magnetic insulators. In the present paper, we investigate the magnetization dynamics in a thin-film stack consisting of two FIs that are in contact via an NM. The macrospin dynamics in a similar system with metallic ferromagnets have been studied both theoretically and experimentally [33]. We expand on that work by focusing on inhomogeneous magnetization excitations in FIs. For long-wavelength spin waves traveling in-plane in a ferromagnetic thin film, the frequency as a function of the in-plane wave number Q strongly depends on the direction of the external magnetic field with respect to the propagation direction. If the external field is in-plane and the spin waves are traveling parallel to this direction, the waves have a negative group velocity. Because the magnetization precession amplitudes are usually evenly distributed across the film in this geometry, these modes are known as backward volume magnetostatic spin waves (BVMSW). Similarly, spin waves that correspond to out-of-plane external fields are known as forward volume magnetostatic spin waves (FVMSW); i.e., the group velocity is positive, and the precession amplitudes are evenly distributed across the film. When the external field is in-plane and perpendicular to the propagation direction, the precession amplitudes of the spin waves become inhomogeneous across the film, experiencing localization to one of the interfaces. These spin waves are thus known as magnetostatic surface spin waves (MSSW) [34,35]. When two ferromagnetic films are coupled via a normal metal, the spin waves in the two films become coupled through two different mechanisms. First, the dynamic, nonlocal dipole-dipole interaction causes an interlayer coupling to arise that is independent of the properties of the normal metal. This coupling is weaker for larger thicknesses of the normal metal. Second, spin pumping from one ferromagnetic insulator induces a spin accumulation in the normal metal, which in turn gives rise to a spin-transfer torque on the other ferromagnetic insulator, and vice versa. In contrast to the static exchange coupling [36], this dynamic coupling is rather long-ranged and is limited only by the spin-diffusion length. This type of coupling is known to strongly couple the macrospin modes. When two ferromagnetic films become coupled, the characterization of the spin waves in terms of FVMSW, BVMSW, and MSSW still holds, but the dispersion relations are modified. It is also clear that the damping renormalization caused by spin pumping into the NM may differ greatly from that in a simpler FI|N bilayer system. To understand this phenomenon, we perform a detailed analytical and numerical analysis of a trilayer system, with the hope that our findings may be used as a guide for experimentalists. This paper is organized as follows. Section II introduces the model. The details of the dynamic dipolar field are discussed, and the boundary conditions associated with spin pumping and spin transfer at the FI|N interfaces are calculated. Section III provides the analytical solutions of these equations in the long-wavelength regime dominated by the dynamic coupling attributable to spin pumping and spin transfer. To create a more complete picture of the dynamic behavior of this system, we perform a numerical analysis for the entire spin-wave spectrum of this system, which is presented in Sec. IV. We conclude our work in Sec. V.

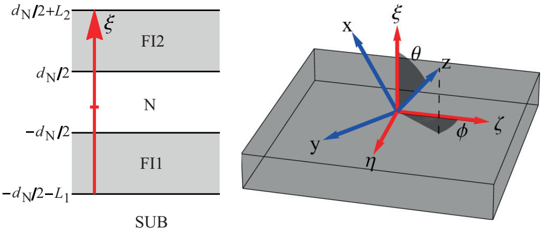

(a) (b)

FIG. 1. (Color online) (a) A cross section of the FI1|N|FI2 heterostructure. The ferromagnetic insulators FI1 and FI2 are in contact via the normal metal N. The transverse coordinate ξ is indicated along with the thicknesses L_1, d_N, and L_2 of FI1, N, and FI2, respectively. (b) The coordinate system of the internal field (blue) with respect to the coordinate system of the FI1| N|FI2 structure (red). θ denotes the angle between the film normal and the internal field, and ϕ is the angle between the in-plane component of the magnetic field and the in-plane wave vector.

II. EQUATIONS OF MOTION

Consider a thin-film heterostructure composed of two ferromagnetic insulators (FI1 and FI2) that are in electrical contact via an NM layer. The ferromagnetic insulators FI1 and FI2 may have different thicknesses and material properties. We denote the thicknesses by L_1, d_N, and L_2 for the FI1, NM, and FI2 layers, respectively [see Fig. 1(a)]. The in-plane coordinates are ζ,η, and the transverse coordinate is ξ [see Fig. 1(b)]. We will first discuss the magnetization dynamics in isolated FIs and will then incorporate the spin-memory losses and the coupling between the FIs via spin currents passing through the NM.

A. Magnetization dynamics in isolated FIs

The magnetization dynamics in the ferromagnetic insulators can be described using the Landau-Lifshitz-Gilbert (LLG) equation,

$$\dot{\mathbf{M}}_i = -\gamma \mathbf{M}_i \times \mathbf{H}_{\text{eff}} + \alpha \mathbf{M}_i \times \dot{\mathbf{M}}_i, \tag{1}$$

where $\mathbf{M}_i$ is the unit vector in the direction of the magnetization in layer $i = 1,2$, γ is the gyromagnetic ratio, α is the dimensionless damping parameter, and $\mathbf{H}_{\text{eff}}$ is the space-time-dependent effective magnetic field. The effective magnetic field is

$$\mathbf{H}_{\text{eff}} = \mathbf{H}_{\text{int}} + \mathbf{h}_{\text{ex}} + \mathbf{h}_{\text{d}} + \mathbf{h}_{\text{surface}}, \tag{2}$$

where $\mathbf{H}_{\text{int}}$ is the internal field attributable to an external magnetic field and the static demagnetization field, $\mathbf{h}_{\text{ex}} = 2A\nabla^2\mathbf{M}/M_S$ is the exchange field (A is the exchange constant),

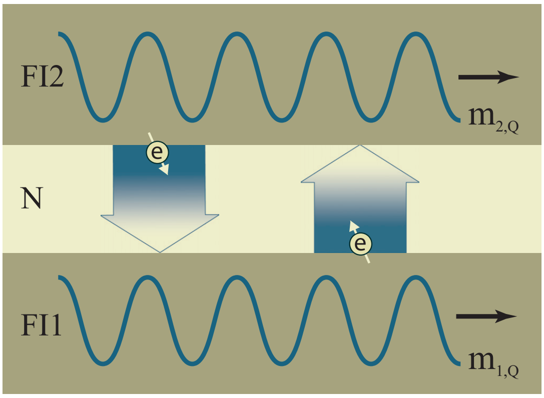

FIG. 2. (Color online) Two coupled spin waves with amplitude $\mathbf{m}_{1Q}$ in ferromagnet FI1 and amplitude $\mathbf{m}_{2Q}$ in ferromagnet FI2. The spin waves inject a spin current into the normal metal (NM) via spin pumping. In the NM, the spins diffuse and partially relax, inducing a spin accumulation therein. In turn, the spin accumulation causes spin-transfer torques to arise on FI1 and FI2. The combined effect of spin transfer and spin pumping leads to a dynamic exchange coupling that, together with the dynamic demagnetization field, couples the spin waves in the two FIs.

$\mathbf{h}_{\mathrm{d}}$ is the dynamic demagnetization field, and

$$\mathbf{h}_{\mathrm{surface}} = \frac{2K_S}{M_S}(\mathbf{M}_i \cdot \hat{\mathbf{n}})\delta(\xi - \xi_i)\hat{\mathbf{n}} \tag{3}$$

is the surface anisotropy field located at the FI|N interfaces. In this work, $\mathbf{h}_{\mathrm{surface}}$ is assumed to exist only at the FI|N interfaces and not at the interfaces between the FIs and the substrate or vacuum. It is straightforward to generalize the discussion to include these surface anisotropies as well. We consider two scenarios: one with an surface anisotropy ($K_S \neq 0$) and one with no surface anisotropy ($K_S = 0$). Note that a negative value of $K_S \sim -0.03\ \mathrm{erg/cm^2}$, which implies an easy-plane surface anisotropy, has also been observed for sputtered YIG|Au bilayers [37]. In general, the effective field $\mathbf{H}_{\mathrm{eff}}$ may differ in the two FIs. We assume the two FIs consist of the same material and consider external fields that are either in-plane or out-of-plane. Furthermore, we consider devices in which the internal magnetic fields in the two FI layers are aligned and of equal magnitude. In equilibrium, the magnetization inside the FIs is oriented along the internal magnetic field, $\mathbf{M}_i = \mathbf{M}_0$. In the linear response regime, $\mathbf{M}_i = \mathbf{M}_0 + \mathbf{m}_i$, where the first-order correction $\mathbf{m}_i$ is small and perpendicular to $\mathbf{M}_0$. The magnetization vanishes outside of the FIs. Because the system is translationally invariant in the η and ζ directions, we may, without loss of generality, assume that $\mathbf{m}$ consists of plane waves traveling in the ζ direction (see Fig. 2),

$$\mathbf{m}_i(\zeta,\eta,\xi) = \mathbf{m}_{iQ}(\xi)e^{i(\omega t - Q\zeta)}. \tag{4}$$

Linearizing Maxwell's equations in $\mathbf{m}_i$ implies that the dynamic dipolar field must be of the same form,

$$\mathbf{h}_{\mathrm{d}}(\zeta,\eta,\xi) = \mathbf{h}_{\mathrm{d}Q}(\xi)e^{i(\omega t - Q\zeta)}. \tag{5}$$

Furthermore, the total dipolar field (the sum of the static and the dynamic dipolar fields) must satisfy Maxwell's equations, which, in the magnetostatic limit, are

$$\nabla \cdot (\mathbf{h}_{\mathrm{d}} + 4\pi M_S \mathbf{m}) = 0, \tag{6a}$$

$$\nabla \times \mathbf{h}_{\mathrm{d}} = 0, \tag{6b}$$

with the boundary equations

$$(\mathbf{h}_{\mathrm{d}} + 4\pi M_S \mathbf{m})_{\perp,\mathrm{in}} = (\mathbf{h}_{\mathrm{d}})_{\perp,\mathrm{out}}, \tag{7a}$$

$$(\mathbf{h}_{\mathrm{d}})_{\parallel,\mathrm{in}} = (\mathbf{h}_{\mathrm{d}})_{\parallel,\mathrm{out}}, \tag{7b}$$

where the subscript in (out) denotes the value on the FI (NM, vacuum or substrate) side of the FI interface and $\perp$ ($\parallel$) denotes the component(s) perpendicular (parallel) to the FI-NM interfaces. Solving Maxwell's equations (6) with the boundary conditions of Eq. (7) yields [34]

$$\mathbf{h}_{\mathrm{d}Q}(\xi) = 4\pi M_S \int d\xi' \hat{G}(\xi - \xi')\mathbf{m}_Q(\xi'), \tag{8}$$

where $\hat{G}(\mathbf{r} - \mathbf{r}')$ is a 3×3 matrix acting on $\mathbf{m}$ in the (η,ζ,ξ) basis,

$$\hat{G}(\xi) = \begin{pmatrix} G^{\mathrm{P}}(\xi) - \delta(\xi) & 0 & -iG^{\mathrm{Q}}(\xi) \\ 0 & 0 & 0 \\ -iG^{\mathrm{Q}}(\xi) & 0 & -G^{\mathrm{P}}(\xi) \end{pmatrix}. \tag{9}$$

Here, $G^{\mathrm{P}}(\xi) = Qe^{-Q|\xi|}/2$, and $G^{\mathrm{Q}}(\xi) = -\mathrm{sgn}(\xi)G^{\mathrm{P}}$. Note that the dynamic dipolar field of Eq. (8) accounts for both the interlayer and intralayer dipole-dipole couplings because the magnetization varies across the two magnetic insulator bilayers and vanishes outside these materials. It is now convenient to perform a transformation from the ζ-η-ξ coordinate system defined by the sample geometry to the x-y-z coordinate system defined by the internal field [see Fig. 1(b)]. In the linear response regime, the dynamic magnetization $\mathbf{m}_i$ lies in the x-y plane, and the linearized equations of motion become [34]

$$\left\{ i\omega \begin{pmatrix} \alpha & -1 \\ 1 & \alpha \end{pmatrix} + \mathbb{1}\left(\omega_H + \frac{2A}{M_S}\left[Q^2 - \frac{\mathrm{d}^2}{\mathrm{d}\xi^2}\right]\right)\right\} \mathbf{m}_{iQxy}(\xi)$$

$$= \sum_{i=1}^{2} \int d\xi' \hat{\mathcal{G}}_{xy}(\xi - \xi')\mathbf{m}_{iQxy}(\xi'). \tag{10}$$

Here, $\mathbf{m}_{iQxy} = (m_{iQx}, m_{iQy})$ is the Fourier transform of the dynamic component of the magnetization in the x-y plane and $\hat{\mathcal{G}}_{xy}(\xi)$ is the 2×2 matrix that results from rotating $\hat{G}(\xi)$ into the x-y-z coordinate system (see Appendix A), considering only the xx, xy, yx, and yy components.

B. Boundary conditions and spin accumulation

The linearized equations of motion (10) must be supplemented with boundary conditions for the dynamic magnetization at the FI|N interfaces. A precessing magnetization at the FI|N boundaries injects a spin-polarized current, $\mathbf{j}^{\mathrm{SP}}$, into the NM, an effect known as *spin pumping* [8,29–31]. The emitted spin currents at the lower and upper interfaces ($i = 1,2$) in units of charge current per area are

$$\mathbf{j}_i^{\mathrm{SP}} = \frac{\hbar}{e} g_\perp \mathbf{M}_i \times \dot{\mathbf{M}}_i \bigg|_{\xi=\xi_i}, \tag{11}$$

where $\xi_i = \mp d_{\mathrm{N}}/2$ at the lower and upper interfaces, respectively, and $g_\perp$ is the real part of the transverse spin-mixing conductance per unit area [38]. We disregard the imaginary part of the spin-mixing conductance because it has been found to be small at FI|N interfaces [39]. The reciprocal effect of spin pumping is spin transfer into the FIs because of a spin accumulation $\boldsymbol{\mu}_S$ in the NM. In the normal metal at the lower and upper interfaces ($i = 1,2$), the associated spin-accumulation-induced spin current is

$$\mathbf{j}_i^{\mathrm{ST}} = -\frac{1}{e} g_\perp \mathbf{M}_i \times (\mathbf{M}_i \times \boldsymbol{\mu}_S) \bigg|_{\xi=\xi_i}. \tag{12}$$

The signs of the pumped and spin-accumulation-induced spin currents in Eqs. (11) and (12) were chosen such that they are positive when there is a flow of spins from the NM toward the FIs. The pumped and spin-accumulation-induced spin currents of Eqs. (11) and (12) lead to magnetic torques acting on the FI interfaces. The torques that correspond to the spin pumping and spin transfer localized at the FI|N interfaces are

$$\boldsymbol{\tau}_i^{\mathrm{SP}} = \frac{\gamma \hbar^2}{2e^2 M_S} g_\perp \delta(\xi - \xi_i) \mathbf{M}_i \times \dot{\mathbf{M}}_i, \tag{13a}$$

$$\boldsymbol{\tau}_i^{\mathrm{ST}} = -\frac{\gamma \hbar}{2e^2 M_S} g_\perp \mathbf{M}_i \times (\mathbf{M}_i \times \boldsymbol{\mu}_S) \delta(\xi - \xi_i), \tag{13b}$$

respectively. In the presence of spin currents to and from the normal metal, the magnetization dynamics in the FIs is then governed by the modified Landau-Lifshitz-Gilbert-Slonczewski (LLGS) equation,

$$\dot{\mathbf{M}} = -\gamma \mathbf{M}_i \times \mathbf{H}_{\mathrm{eff}} + \alpha \mathbf{M}_i \times \dot{\mathbf{M}}_i + \sum_{i=1,2} \boldsymbol{\tau}_i^{\mathrm{SP}} + \boldsymbol{\tau}_i^{\mathrm{ST}}. \tag{14}$$

By integrating Eq. (14) over the FI|N interfaces and the interfaces between the FI and vacuum/substrate, we find that $\mathbf{m}_i$ must satisfy the boundary conditions [21,32]

$$\left(\pm L_i \frac{d\mathbf{m}_i}{d\xi} + \chi_i \left[\dot{\mathbf{m}}_i - \frac{1}{\hbar} \mathbf{M}_0 \times \boldsymbol{\mu} \right] + \frac{L_i K_S}{A} \cos(2\theta) \mathbf{m}_i \right)_x \bigg|_{\xi=\mp d_{\mathrm{N}}/2} = 0, \tag{15a}$$

$$\left(\pm L_i \frac{d\mathbf{m}_i}{d\xi} + \chi_i \left[\dot{\mathbf{m}}_i - \frac{1}{\hbar} \mathbf{M}_0 \times \boldsymbol{\mu} \right] + \frac{L_i K_s}{A} \cos^2(\theta) \mathbf{m}_i \right)_y \bigg|_{\xi=\mp d_{\mathrm{N}}/2} = 0, \tag{15b}$$

$$\frac{d\mathbf{m}_1}{d\xi} \bigg|_{\xi=-d_{\mathrm{N}}/2-L_1} = 0, \quad \frac{d\mathbf{m}_2}{d\xi} \bigg|_{\xi=d_{\mathrm{N}}/2+L_2} = 0. \tag{15c}$$

Here, we have introduced the time scale $\chi_i = L_i \hbar^2 g_\perp / 4Ae^2$. The subscripts x and y in Eqs. (15a) and (15b) denote the x and y components, respectively. In our expressions for the boundary conditions (15), we have also accounted for the possibility of a surface anisotropy arising from the effective field described by Eq. (3), where $K_S > 0$ indicates an easy-axis surface anisotropy (EASA). The boundary conditions of Eq. (15), in combination with the transport equations in the NM, which we will discuss next, determine the spin accumulation in the NM and the subsequent torques caused by spin transfer. In the normal metal, the spins diffuse, creating a spatially dependent spin-accumulation potential $\boldsymbol{\mu}_Q$, and they relax on the spin-diffusion length scale l_{sf}. The spin accumulation for an FI|N|FI system has been calculated in the macrospin model [40]. The result of this calculation can be directly generalized to the present situation of spatially inhomogeneous spin waves by replacing the macrospin magnetization in each layer with the interface magnetization and substituting the spin-diffusion length with a wave-vector-dependent effective spin-diffusion length $l_{\mathrm{sf}} \to \tilde{l}_{\mathrm{sf}}(Q)$ such that

$$\boldsymbol{\mu}_Q = -\frac{\hbar}{2} \mathbf{M}_0 \times \{ [\dot{\mathbf{m}}_Q(\xi_1) + \dot{\mathbf{m}}_Q(\xi_2)] \Gamma_1(\xi) - [\dot{\mathbf{m}}_Q(\xi_1) - \dot{\mathbf{m}}_Q(\xi_2)] \Gamma_2(\xi) \}. \tag{16}$$

See Appendix B for the details of the functions Γ_1 and Γ_2. The effective spin-diffusion length is determined by Fourier-transforming the spin-diffusion equation (see Appendix C):

$$\tilde{l}_{\mathrm{sf}} = l_{\mathrm{sf}} / \sqrt{1 + (Q l_{\mathrm{sf}})^2}. \tag{17}$$

We thus have all the necessary equations to describe the linear response dynamics of spin waves in the FI1| N|FI2 system. We now provide analytical solutions of the spin-wave modes in the long-wavelength limit and then complement these solutions with an extensive numerical analysis that is valid for any wavelength.

III. ANALYTIC SOLUTIONS FOR THE SPIN WAVE SPECTRUM

The effect that the exchange and dipolar fields have on the spin-wave spectrum depends on the in-plane wave number Q. When $QL_i \ll 1$, the dipolar field dominates over the exchange field. In the opposite regime, when $QL_i \gg 1$, the exchange field dominates over the dipolar field. The intermediate regime is the dipole-exchange regime. Another length scale is set by the spin-diffusion length. When $Ql_{\mathrm{sf}} \gg 1$, the effective spin-relaxation length $\tilde{l}_{\mathrm{sf}}$ of Eq. (17) becomes small, and the NM acts as a perfect spin sink. In this case, only the relatively short-ranged dipolar field couples the FIs. We therefore focus our attention on the dipole-dominated regime, in which the interchange of spin information between the two FIs remains active. In the limit $QL_i \ll 1$, the magnetization is homogeneous in the in-plane direction. We may then use the ansatz that the deviation from equilibrium is a sum of transverse traveling waves. Using the boundary conditions on the outer boundaries of the stack, Eq. (15c), we find

$$\mathbf{m}_{iQxy}(\xi) = \begin{pmatrix} X_i \\ Y_i \end{pmatrix} \cos\left\{k_i\left[\xi \pm \left(L_i + \frac{d_\mathrm{N}}{2}\right)\right]\right\}, \tag{18}$$

where $i = 1$ when ξ is inside FI1 and $i = 2$ when ξ is inside FI2. k_1 and k_2 are the out-of-plane wave vectors of the lower and upper films, respectively. The eigenfrequencies of Eq. (10) depend on k_i. To first order in the damping parameter α, we have

$$\omega(k_i) = \omega_M\left[\pm\sqrt{\left(\frac{\omega_H}{\omega_M} + \frac{A}{2\pi M_S^2}k_i^2\right)\left(\frac{\omega_H}{\omega_M} + \frac{A}{2\pi M_S^2}k_i^2 + \sin^2\theta\right)} + i\alpha\left(\frac{\omega_H}{\omega_M} + \frac{A}{2\pi M_S^2}k_i^2 + \frac{1}{2}\sin^2\theta\right)\right]. \tag{19}$$

We can, without loss of generality, consider only those frequencies that have a positive real part. The eigenfrequency ω is a characteristic feature of the entire system, so we must require $\omega(k_1) = \omega(k_2)$, which implies that $k_1 = \pm k_2$. We will discuss the cases of symmetric ($L_1 = L_2$) and asymmetric ($L_1 \neq L_2$) geometries separately.

A. Symmetric FI films without surface anisotropy

Consider a symmetric system in which the FIs are of identical thickness and material properties. We assume that the effect of surface anisotropy is negligible, which is the case for thin films and/or weak surface anisotropy energies such that $|K_S|L/A \ll 1$, where $L = L_1 = L_2$. The other two boundary conditions, (15a) and (15b), couple the amplitude vectors $(X_1 \quad Y_1)^\mathrm{T}$ and $(X_2 \quad Y_2)^\mathrm{T}$ of Eq. (18). A nontrivial solution implies that the determinant containing the coefficients of the resulting 4×4 matrix equation vanishes. Solving the secular equation, we find the following constraints on k,

$$i\chi_\mathrm{A}\omega_\mathrm{A} = kL\tan(kL), \tag{20a}$$

$$i\chi_\mathrm{O}\omega_\mathrm{O} = kL\tan(kL), \tag{20b}$$

where

$$\chi_\mathrm{A} = \chi\left(1 - \left[1 + \frac{2g_\perp l_\mathrm{sf}}{\sigma}\tanh(d_\mathrm{N}/2l_\mathrm{sf})\right]^{-1}\right), \tag{21a}$$

$$\chi_\mathrm{O} = \chi\left(1 - \left[1 + \frac{2g_\perp l_\mathrm{sf}}{\sigma}\coth(d_\mathrm{N}/2l_\mathrm{sf})\right]^{-1}\right), \tag{21b}$$

and $\chi = L\hbar^2 g_\perp/4Ae^2$. The two solutions correspond to a symmetric mode (acoustic) and an antisymmetric mode (optical). This result can be understood in terms of the eigenvectors that correspond to the eigenvalues of Eqs. (20), which are $\mathbf{m}_1 = +\mathbf{m}_2$ and $\mathbf{m}_1 = -\mathbf{m}_2$ for the acoustic and optical modes, respectively. Typically, because spin pumping only weakly affects the magnetization dynamics, the time scale χ that is proportional to the mixing conductance $g_\perp$ is much smaller than the FMR precession period. In this limit, $kL\tan(kL) \ll 1$. This result allows us to expand the secular equations (20) around $kL = n\pi$, where n is an integral number, which yields

$$i\chi_\nu\omega_{\nu,n} \approx (kL + \pi n)kL, \tag{22}$$

where $\nu = \mathrm{A,O}$. This result can be reinserted into the bulk dispersion relation of Eq. (19), from which we can determine the renormalization of the Gilbert damping coefficient attributable to spin pumping, $\Delta\alpha$. We define

$$\Delta\alpha = \alpha(\mathrm{Im}[\omega^{(\mathrm{SP})}] - \mathrm{Im}[\omega^{(0)}])/\mathrm{Im}[\omega^{(0)}] \tag{23}$$

as a measure of the spin-pumping-enhanced Gilbert damping, where $\omega^{(0)}$ and $\omega^{(\mathrm{SP})}$ are the frequencies of the same system without and with spin pumping, respectively. Similar to the case of a single-layer ferromagnetic insulator [32], we find that all higher transverse volume modes exhibit an enhanced magnetization dissipation that is twice that of the macrospin mode. The enhancement of the Gilbert damping for the macrospin mode ($n = 0$) is

$$\Delta\alpha_{\nu,\mathrm{macro}} = \frac{\gamma\hbar^2 g_\perp}{2LM_S e^2}\frac{\chi_\nu}{\chi}, \tag{24}$$

and for the other modes, we obtain

$$\Delta\alpha_{\nu,n\neq 0} = 2\Delta\alpha_{\nu,\mathrm{macro}}. \tag{25}$$

Compared with single-FI systems, the additional feature of systems with two FIs is that the spin-pumping-enhanced Gilbert damping differs significantly between the acoustic and optical modes via the mode-dependent ratio χ_ν/χ. This phenomenon has been explored both experimentally and theoretically in Ref. [33] for the macrospin modes $n = 0$ when there is no loss of spin transfer between the FIs, $l_\mathrm{sf} \to \infty$. Our results represented by Eqs. (24) and (25) are generalizations of these results for the case of other transverse volume modes and account for spin-memory loss. Furthermore, in Sec. IV, we present the numerical results for the various spin-wave modes when the in-plane momentum Q is finite. When the NM is a perfect spin sink, there is no transfer of spins between the two FIs, and we recover the result for a single FI|N system with vanishing back flow, $\chi_\nu \to \chi$ [32]. Naturally, in this case, the FI| N|FI system acts as two independent FI|N systems with respect to magnetization dissipation. The dynamic interlayer dipole coupling is negligible in the limit that is considered in this section ($QL \ll 1$). In the opposite regime, when the NM film is much thinner than the spin-diffusion length and the spin conductivity of the NM is sufficiently large such that $g_\perp d_\mathrm{N}/\sigma \ll 1$, then $\chi_\mathrm{A} \to 0$ and $\chi_\mathrm{O} \to \chi$. This result implies that for the optical mode, the damping is the same as for a single FI in contact with a perfect spin sink, even though the spin-diffusion length is very large. The reason for this phenomenon is that when the optical mode is excited, the magnetizations of the two films oscillate out of phase such that one layer acts as a perfect spin sink for the other layer. By contrast, there is no enhancement of the Gilbert damping coefficient for the acoustic mode; when the film is very thin and the magnetizations of the two layers are in phase, there is no net spin flow or loss in the NM film and no spin-transfer-induced losses in the ferromagnets. Finally, when the NM is a poor conductor despite exhibiting low spin-memory loss such that $g_\perp d_N/\sigma \gg (l_{sf}/d_N) \gg 1$, then $\chi_\nu \to 0$ because there is no exchange of spin information. For the macrospin modes in the absence of spin-memory loss, these results are in exact agreement with Ref. [33]. Beyond these results, we find that regardless of how much spin memory is lost, it is also the case that in trilayer systems, all higher transverse modes experience a doubling of the spin-pumping-induced damping. Furthermore, these modes can still be classified as optical and acoustic modes with different damping coefficients.

B. Symmetric films with surface anisotropy

Magnetic surface anisotropy is important when the spin-orbit interaction at the interfaces is strong. In this case, the excited mode with the lowest energy becomes inhomogeneous in the transverse direction. We first consider the FVMSW geometry before discussing the general case. A finite K_S introduces new terms into the boundary condition (15). For the ansatz

$$\mathbf{m}_{iQxy}(\xi) = \begin{pmatrix} X_i \cos[k\xi \pm k(L + d_N/2)] \\ Y_i \cos[k\xi \pm k(L + d_N/2)] \end{pmatrix}, \tag{26}$$

the boundary equation (15b) is satisfied, and Eqs. (15a) and (15b) yield

$$i\chi_\nu\omega_\nu + \frac{LK_S}{A} = kL\tan(kL)\,, \tag{27a}$$

$$i\chi_\nu\omega_\nu + \frac{LK_S}{A} = kL\tan(kL)\,, \tag{27b}$$

where ν continues to denote an acoustic (A) or optical (O) mode, $\nu = \mathrm{A,O}$. Depending on the sign of K_S and the angle θ, the resulting solutions for k can become complex, which implies that the modes are evanescent. For a negative anisotropy constant and a thick FIs $-LK_S/A \gg 1$, we find that $\kappa = ik = -K_S/A - i\chi_\nu\omega_\nu/L$, such that

$$\mathbf{m}_{iQxy}(\xi) = \begin{pmatrix} X_i \cosh[\kappa\xi \pm \kappa(L + d_N/2)] \\ Y_i \cosh[\kappa\xi \pm \kappa(L + d_N/2)] \end{pmatrix}. \tag{28}$$

The dynamic part of the magnetization is exponentially localized at the FI|N surfaces. Following the same procedure as in Sec. III A for the $K_S = 0$ case, we insert this solution into the dispersion relation (19) and extract the renormalization of the effective Gilbert damping:

$$\Delta\alpha_\nu^{\mathrm{SA,FVMSW}} = \frac{\gamma\hbar^2 g_\perp}{2LM_S e^2}\frac{\chi_\nu}{\chi}2\frac{K_S L}{A}. \tag{29}$$

This Gilbert damping enhancement may become orders of magnitude larger than the $\Delta\alpha_{\mathrm{macro}}$ of Eq. (24). For thick films, $\Delta\alpha_{\mathrm{macro}} \sim L^{-1}$, whereas $\Delta\alpha_\nu^{\mathrm{SA,FVMSW}}$ reaches a constant value that is inversely proportional to the localization length at the FI|N interface. Note that for large surface anisotropy, the equilibrium magnetization is no longer oriented along the external field, and Eq. (29) for $\Delta\alpha$ becomes invalid. For in-plane field geometries (BVMSW and MSSW), an easy axis surface anisotropy ($K_S > 0$) leads to a similar localization. For in-plane static magnetization, only one of the two dynamic components points out-of-plane, thereby introducing an asymmetry between the two components in the boundary conditions. Thus, the ansatz of Eq. (26) has to be modified, resulting in a surface localization that is governed by the length scale A/K_S but with a geometric renormalization that is attributable to the component asymmetry. This aspect has been treated in Refs. [22,41] for a FI|N bilayer system. For $\mathbf{m}_1 = \pm\mathbf{m}_2$, the boundary conditions (15) take the same form as the corresponding equations for the bilayer, except for a renormalized factor $\chi \to \chi_\nu$. The effective mode-dependent damping that is induced by spin pumping for any geometry and an arbitrary value of K_S is then

$$\Delta\alpha_\nu^{\mathrm{SA}} = \frac{\chi_\nu}{\chi}\Delta\alpha^{\mathrm{FI|N(spin\ sink)}}. \tag{30}$$

In this way, this result for $\Delta\alpha$ is considered relative to the equivalent FI|N(spin sink) bilayer system. Thus, the effect of the coupling of the layers is clearly evident in the renormalization factor χ_ν/χ, where $\chi = \mathrm{A,O}$ [see Eq. (21)].

Exciting the acoustic modes require a torque which acts symmetrically on the two layers. This can be achieved with a radio strip antenna. Conversely, excitation of the optical modes require an antisymmetric torque. We suggest that this can be achieved by the use of spin torque FMR (ST-FMR), where an ac spin current is induced via the spin Hall effect, by applying an ac charge current. The resulting spin Hall induced torque acts with opposite sign on the two layers [40]. By letting a strip of the NM spacer consist of a high spin Hall angle NM (e.g., Pt or Ta), finite Q optical modes can be excited.

C. Asymmetric FI films

Let us now consider an asymmetric system in which $L_1 \neq L_2$. In this configuration, we will first consider $K_S = 0$, but we will also comment on the case of a finite K_S at the end of the section. Because the analytical expressions for the eigenfrequencies and damping coefficients are lengthy, we focus on the most interesting case: that in which the spin-relaxation rate is slow. As in the case of the symmetric films, the dispersion relation of Eq. (10) dictates that the wave numbers in the two layers must be the same. To satisfy the boundary equations (15), we construct the ansatz

$$\mathbf{m}_{iQxy}(\xi) = \begin{pmatrix} X_i \cos[k\xi \pm k(L + d_N/2)] \\ Y_i \cos[k\xi \pm k(L + d_N/2)] \end{pmatrix}. \tag{31}$$

The difference between this ansatz and that for the symmetric case represented by Eq. (26) is that the magnitudes of the amplitudes, X_i and Y_i, of the two layers, $i = 1,2$, that appear in Eq. (31) no longer have to be equal to each other. When the two ferromagnets FI(L_1) and FI(L_2) are completely disconnected, the transverse wave vectors must be equivalent to standing waves, $q_{n,1} = \pi n/L_1$ and $q_{m,2} = \pi m/L_2$ in the two films, respectively, where n and m may be any integral numbers. Because spin pumping is weak, the eigenfrequencies of the coupled system are close to the eigenfrequencies of the isolated FIs. This finding implies that the wave vector k of the coupled system is close to either $q_{n,1}$ or $q_{m,2}$. The solutions of the linearized equations of motion are then

$$k = k_{n,1} = q_{n,1} + \delta k_{n,1} \quad \text{or} \tag{32a}$$

$$k = k_{m,2} = q_{m,2} + \delta k_{m,2}, \tag{32b}$$

where $\delta k_{n,1}$ and $\delta k_{m,2}$ are small corrections attributable to spin pumping and spin transfer, respectively. Here, the indices 1 and 2 represent the different modes rather than the layers. However, one should still expect that mode 1 (2) is predominantly localized in film 1 (2). In this manner, we map the solutions of the wave vectors in the coupled system to the solutions of the wave vectors in the isolated FIs. Next, we will present solutions that correspond to the $q_{n,1}$ of Eq. (32a). The other family of solutions, corresponding to $q_{m,2}$, is determined by interchanging $L_1 \leftrightarrow L_2$ and making the replacement $n \to m$. Inserting Eq. (32a) into the boundary conditions of Eq. (15) and linearizing the resulting expression in the weak spin-pumping-induced coupling, we find, for the macrospin modes,

$$i\omega\tilde{\chi}^{\mathrm{A,O}}_{1,\mathrm{macro}} = (L_1 \delta k_{0,1})^2, \tag{33}$$

where

$$\tilde{\chi}^{\mathrm{A}}_{1,\mathrm{macro}} \approx \frac{1}{2}\frac{d_{\mathrm{N}}}{l_{\mathrm{sf}}}\frac{\sigma}{g_\perp l_{\mathrm{sf}}}\frac{L_1}{L_1+L_2}\chi_1, \tag{34a}$$

$$\tilde{\chi}^{\mathrm{O}}_{1,\mathrm{macro}} \approx \frac{1}{2}\frac{L_1+L_2}{L_2}\chi_1. \tag{34b}$$

Here, $\chi_1 = L_1\hbar^2 g_\perp/4Ae^2$. Inserting this parameter into the dispersion relation of Eq. (19), we obtain the following damping renormalizations:

$$\Delta\alpha^{\mathrm{A}}_{\mathrm{macro}} = \frac{\gamma\hbar^2 g_\perp}{2M_S e^2}\frac{1}{2}\frac{d_{\mathrm{N}}}{l_{\mathrm{sf}}}\frac{\sigma}{g_\perp l_{\mathrm{sf}}}\frac{1}{L_1+L_2}, \tag{35a}$$

$$\Delta\alpha^{\mathrm{O}}_{\mathrm{macro}} = \frac{\gamma\hbar^2 g_\perp}{2M_S e^2}\frac{1}{2}\left(\frac{1}{L_1}+\frac{1}{L_2}\right). \tag{35b}$$

These two solutions correspond to an acoustic mode and an optical mode, respectively. The corresponding eigenvectors are $\mathbf{m}_1 = \mathbf{m}_2$ for the acoustic mode and $L_1\mathbf{m}_1 = -L_2\mathbf{m}_2$ for the optical mode. As in the symmetric case, the damping enhancement of the acoustic mode vanishes in the thin-NM limit. In this limit, the behavior of the acoustic mode resembles that of a single FI of thickness $L_1 + L_2$. The total thickness determines the leading-order contribution of the damping renormalization. The optical mode, however, experiences substantial damping enhancement. For this mode, the damping renormalization is the average of two separate FIs that are in contact with a perfect spin sink. The cause of this result is as follows. When there is no spin-memory loss in the NM, half of the spins that are pumped out from one side return and rectify half of the angular-momentum loss attributable to spin pumping. Because the magnetization precessions of the two films are completely out of phase, the other half of the spin current causes a dissipative torque on the opposite layer. In effect, spin pumping leads to a loss of angular momentum, and the net sum of the spin pumping across the NM and the back flow is zero. The total dissipation is not affected by spin transfer, and thus, the result resembles a system in which the NM is a perfect spin sink. For the higher excited transverse modes, there are two scenarios, which we treat separately. (I) The allowed wave number for one layer matches a wave number for the other layer. Then, for some integer $n > 0$, $q_{n,1} = q_{m,2}$ for some integer m. In this case, we expect a coupling of the two layers. (II) The allowed wave number for one layer does not match any of the wave numbers for the other layer, and thus, for some integer $n > 0$, we have $q_{n,1} \neq q_{m,2}$ for all integers m. We then expect that the two layers will not couple. (I) In this case, we find two solutions that correspond to acoustic and optical modes. These modes behave very much like the macrospin modes; however, as in the symmetric case, the damping renormalization is greater by a factor of 2:

$$\Delta\alpha^{\mathrm{A,O}}_{n\neq 0} = 2\Delta\alpha^{\mathrm{A,O}}_{\mathrm{macro}}, \qquad \text{case I.} \tag{36}$$

The eigenvectors of these coupled modes have the same form as for the macrospin modes, such that $\mathbf{m}_1 = \mathbf{m}_2$ and $L_1\mathbf{m}_1 = -L_2\mathbf{m}_2$ for the acoustic and optical modes, respectively. (II) In this case, the two layers are completely decoupled. To the leading order in $d_{\mathrm{N}}/l_{\mathrm{sf}}$, we find

$$\Delta\alpha_{n\neq 0} = \frac{\gamma\hbar^2 g_\perp}{2L_1 M_S e^2}, \qquad \text{case II,} \tag{37}$$

for all modes that correspond to excitations in FI1. The damping renormalization is thus half that of the FI(L_1)|N($l_{\mathrm{sf}} = 0$) system [32]. This result can be explained by the zero loss of spin memory in the NM. Although half of the spins are lost to the static FI2, half of the spins return and rectify half of the dissipation attributable to spin pumping. The amplitudes of these modes are strongly suppressed in FI2 (or FI1, upon the interchange of FI1 $\leftrightarrow$ FI2), such that $|\mathbf{m}_2|/|\mathbf{m}_1| \sim \omega\chi_2$. Finally, let us discuss the case in which surface anisotropy is present. In the limit $|K_S|L_i/A \gg 1$, the excitation energies of the surface modes are independent of the FI thicknesses. However, the surface modes do not behave like the macrospin modes for the asymmetric stack. The excitation volume of these modes is determined by the decay length A/K_S in accordance with Eq. (28). This finding is in contrast to the result for the macrospin modes, where the excitation volume spans the entire FI. Thus, the surface modes couple in the same manner as in the symmetric case. When the surface anisotropy can be well controlled experimentally, the coupling of the surface modes becomes robust to thickness variations. When surface anisotropy is present, the higher excited transverse modes have thickness-dependent frequencies; i.e., these modes behave similarly to the $n > 0$ modes in the $K_S = 0$ case.

IV. NUMERICAL RESULTS

When the spin-wave wavelength becomes comparable to the film thickness, the dipolar field becomes a complicated function of the wavelength. We study the properties of the system in this regime by numerically solving the linearized equations of motion (10) with the boundary conditions (15). We use the method presented in Ref. [32], which solves the spin-wave excitation spectrum for an FI|N system, and extend this approach to the present trilayer system. The physical parameters used in the numerical calculations are listed in Table I. We investigate two geometries: (I) the BVMSW geometry, in which the spin wave propagates parallel to the external field, and (II) the MSSW geometry, in which the spin

TABLE I. Physical parameters used in the numerical calculations.

Constant	Value	Units
$g_\perp$	3.4×10^{15}[a]	$\mathrm{cm}^{-2}\, e^2/h$
σ	5.4×10^{17}[b]	s^{-1}
$4\pi M_S$	1750[c]	G
A	3.7×10^{-7}[c]	erg/cm
H_{int}	$0.58 \times 4\pi M_S$	
α	3×10^{-4}[c]	
K_S	0, 0.05[d]	$\mathrm{erg/cm}^2$

[a] Reference [42].
[b] Reference [43].
[c] Reference [35].
[d] Reported to be in the range of 0.1–0.01 $\mathrm{erg/cm}^2$ in Ref. [21].

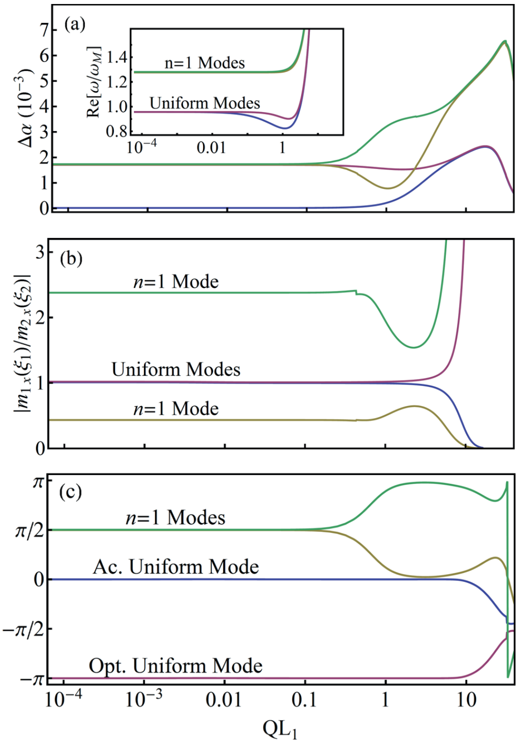

FIG. 3. (Color online) FI(100 nm)|N(50 nm)|FI(101 nm): (a) Spin-pumping-enhanced Gilbert damping $\Delta\alpha$ as a function of QL_1 of the uniform modes and the $n = 1$ modes; inset shows the corresponding dispersion relation; (b) relative phase; and (c) amplitude between the out-of-plane magnetizations along x at the edges of FI1|N and FI2|N; the apparent discontinuity in the green line in (c) results from defining the phase over the interval from $-\pi$ to π.

wave propagates perpendicular to the external field. To calculate the renormalization of the Gilbert damping, we perform one computation without spin pumping and one computation with spin pumping, in which the intrinsic Gilbert damping is excluded. Numerically, the renormalization can then be determined by calculating $\Delta\alpha = \alpha \mathrm{Im}[\omega^{(\mathrm{SP})}]_{\alpha=0}/\mathrm{Im}[\omega^{(0)}]$, where $\omega^{(0)}$ is the eigenfrequency obtained for the computation without spin pumping and $\omega^{(\mathrm{SP})}$ is the frequency obtained for the computation with spin pumping [32].

A. BVMSW

Let us first discuss the BVMSW geometry. The coupling of the uniform modes in the two films is robust; it is not sensitive to possible thickness asymmetries. In contrast, at $Q = 0$, the sensitivity to the ratio between the thickness and the rather weak dynamic coupling attributable to spin pumping implies that the coupling of the higher transverse modes in the two bilayers is fragile. Small asymmetries in the thicknesses destroy the coupling. This effect can best be observed through the renormalization of the damping. However, we will demonstrate that a finite wave number Q can compensate for this effect such that the higher transverse modes also become coupled. To explicitly demonstrate this result, we numerically compute the real and imaginary parts of the eigenfrequencies of a slightly asymmetric system, FI(100 nm)|N(50 nm)|FI(101 nm) with $l_{\mathrm{sf}} = 350$ nm. The asymmetry between the thicknesses of the ferromagnetic insulators is only 1%. The surface anisotropy is considered to be small compared with the ratio L_i/A, and we set $K_S = 0$. In Fig. 3, the numerical results for the effective Gilbert damping, the dispersion of the modes, and the relative phase and amplitude between the magnetizations in the two FIs are presented. As observed in the relative phase results depicted in Fig. 3(c), the two uniform modes in widely separated FIs split into an acoustic mode and an optical mode when the bilayers are coupled via spin pumping and spin transfer. Figure 3(a) also demonstrates that the acoustic mode has a very low renormalization of the Gilbert damping compared with the optical mode. Furthermore, there is no phase difference between the two modes with a transverse node ($n = 1$) in Fig. 3(a), which indicates that the modes are decoupled. These $n = 1$ modes are strongly localized in one of the two films; see Fig. 3(b). For small QL_1, Fig. 3(a) demonstrates that these modes have approximately the same renormalization as the optical mode, which is in agreement with the analytical results. Because the magnetization in the layer with the smallest amplitude is only a response to the spin current from the other layer, the phase difference is $\pi/2$ [Fig. 3(b)]. When Q increases, the dipolar and exchange interactions become more significant. The interlayer coupling is then no longer attributable only to spin pumping but is also caused by the long-range dipole-dipole interaction. This additional contribution to the coupling is sufficient to synchronize the $n = 1$ modes. The relative amplitude between the two layers then becomes closer to 1 [see Fig. 3(b)]. Again, we obtain an acoustic mode and an optical $n = 1$ mode, which can be observed from the phase difference between the two layers in Fig. 3(c). Comparing this system to a system without spin pumping shows that the synchronization results primarily from dipolar coupling (see Appendix D). The elements of the dipole tensor in Eq. (8) exhibit a maximum at $Q = 1/|\xi - \xi'|$. This result implies that the interlayer coupling should be maximal at $Q \sim 1/d_{\mathrm{N}}$. This results agrees well with the synchronization at $QL_1 \gtrsim 1$. The dipole coupling becomes weaker for larger Q, and the modes rapidly decouple because of the reduced spin-pumping coupling, which can be attributed to a decrease in the effective spin-diffusion length. In the large QL_1 limit, the exchange interaction becomes dominant. At large Q, the frequency is dominated by the exchange energy, such that $\omega \sim \omega_M (Ql_{\text{ex}})^2$. Spin pumping is proportional to the frequency; thus, there is a frequency at which the spin pumping term becomes the dominant term in the boundary conditions of Eqs. (15). Spin pumping is then no longer purely dissipative but also contributes a surface pinning term to the energy. Thus, the dynamic part of the magnetization is forced to zero at the FI|N boundaries, causing the renormalization from the spin pumping to vanish for large QL_1. We also note that the dispersion relation depicted in the inset of Fig. 3(a) reveals that the acoustic mode (blue line) exhibits a dip in energy at lower QL_1 than does the optical mode (red line). We suggest that this feature can be understood as follows: The shift in the position of the energy dip can be interpreted as an increase in the effective FI thickness for the acoustic mode with respect to that for the optical mode. When $\tilde{l}_{\text{sf}}$ is larger than the NM thickness, the uniform mode behaves as if the NM were absent and the two films were joined. This result indicates that the dispersion relation for the acoustic mode exhibits frequency behavior as a function of $Q\tilde{L}/2$, where the effective total thickness of the film is $\tilde{L} = L_1 + L_2$. The optical mode, however, "sees" the NM and thus behaves as if $\tilde{L} = L_1$. Consequently, the dip in the dispersion occurs at lower QL_1 for the acoustic mode than for the optical mode.

B. MSSW

Finally, let us study the dynamic coupling of magnetostatic surface spin waves (MSSWs). We now consider a perfectly symmetric system, FI(1000 nm)|N(200 nm)|FI(1000 nm), with $l_{\text{sf}} = 350$ nm. For such thick films, surface anisotropies may play an important role. We therefore discuss a case in which we include a surface anisotropy of $K_S = 0.05\ \text{erg/cm}^2$. According to the analytical result presented in Sec. III A the lowest-energy modes with $QL_1 \ll 1$ are exponentially localized at the FI|N surfaces. The $n \neq 0$ modes are not as strongly affected by the surface anisotropy, and the surface characteristics are only moderately altered [32]. We now compute the eigenfrequencies, ω, as a function of the wave vector in the range $10^{-4} < QL_1 < 10^3$. In Fig. 4(a), we present the real part of the frequency for the six lowest-energy modes with a positive real part, and in Fig. 4(b), we present the corresponding renormalizations of the Gilbert damping for the four lowest-energy modes. The dispersion relations indicate that the mode pairs that are degenerate at $QL_1 \ll 1$ rapidly split in energy when QL_1 approaches 10^{-2}. Strong anticrossings can be observed between the $n = 1$ and $n = 2$ modes. Such anticrossings are also present between the surface mode and the $n = 1$ mode; they are almost too strong to be recognized as anticrossings. The enhanced damping renormalizations exhibit very different behavior for the different modes. We recognize the large-$\Delta\alpha$ mode of one pair as the surface optical mode and the low-$\Delta\alpha$ mode as the volume $n = 1$ acoustic mode. Without EASA, the anticrossings in Fig. 4(a) would become crossings. The lowest-energy modes at $QL_1 \ll 1$ would then cut straight through the other modes. In the case considered here, this behavior is now observed only as steep lines at $QL_1 \sim 0.05$ and at $QL_1 \sim 0.5$. The difference in the energies of the surface modes at $QL_1 \sim 1$ results from the difference in the dipolar interaction between layers [see Eq. (8)]. When Q is increased, the effective spin-diffusion length decreases [see Eq. (17)], which reduces the spin-pumping-induced coupling between the modes at large Q. When $QL_1 \sim 100$, the coupling becomes so weak that the two FIs decouple. This phenomenon can be observed from the behavior of $\Delta\alpha$ in Fig. 4(b), where the damping of the acoustic modes become the same as for the optical modes. In the MSSW geometry, an isolated FI has magnetostatic waves that are localized near one of the two surfaces, depending on the direction of propagation with respect to the internal field [35]. Asymmetries in the excitation volume are therefore also expected for the trilayer in this geometry. In Fig. 5, we present the eigenvectors of the surface modes as functions of the transverse coordinate ξ for increasing values of the wave vector Q. At $QL_1 = 0.5$, the modes have already begun to exhibit some asymmetry. Note that the renormalization of the damping observed in Fig. 4(b) is approximately one order of magnitude larger than the intrinsic Gilbert damping for the optical mode and that the damping of any one mode may vary by several orders of magnitude as a function of QL_1 [32]. Therefore, these effects should be experimentally observable. The greatest damping occurs when

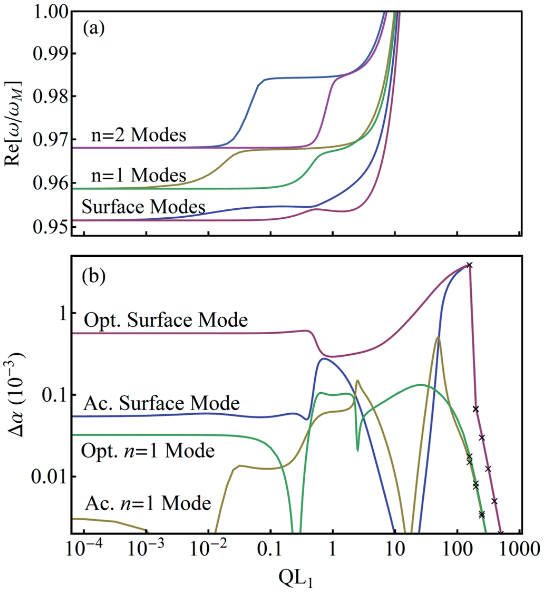

FIG. 4. (Color online) FI(1000 nm)|N(200 nm)|FI(1000 nm), $l_{\text{sf}} = 350$ nm, $K_S = 0.05\ \text{erg/cm}^2$: (a) The dispersion relation as a function of QL_1 for the six lowest positive-real-part modes. (b) The renormalization of the damping attributable to spin pumping for the four lowest modes with frequencies with positive real parts as a function of QL_1. At large QL_1, the computation becomes increasingly demanding, and the point density of the plot becomes sparse. We have therefore individually marked the plotted points in this region.

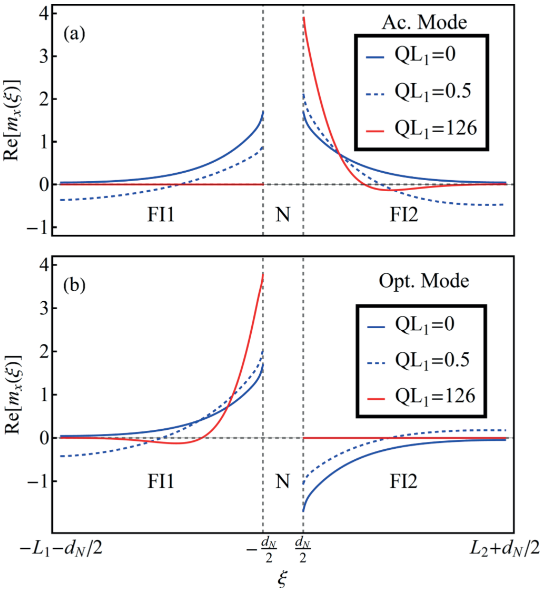

FIG. 5. (Color online) FI(1000 nm)|N(200 nm)|FI(1000 nm), $l_{\mathrm{sf}} = 350$ nm, $K_S = 0.05$ erg/cm^2: (a) and (b) present the real parts of the x components of the out-of-equilibrium magnetization vectors for the acoustic and optical surface modes, respectively, for several values of QL_1. For values of $QL_1 \gtrsim 1$, the modes decouple and become localized in one of the two layers. For large values of $QL_1 \sim 100$, the two modes are strongly localized at one of the two FI|N interfaces, which correspond to the peaks in the damping that are apparent in Fig. 4(b).

the two layers are completely decoupled; see Figs. 4(b) and 5. Because the damping of the optical mode is equivalent to that of a system with a perfect spin sink, one might expect that the greatest damping should occur for this mode. However, the large localization, which is achieved only at large QL_1, in combination with the vanishing of the effective spin-diffusion length, leads to damping that is much greater than that of the synchronized optical mode.

V. CONCLUSIONS

We investigated the dynamic coupling of spin-wave excitations, which are present in single FI thin films, primarily through spin pumping and spin transfer but also through the dynamic demagnetization field created when two FI thin films are in contact via an NM layer. Because of this coupling, the modes are split into acoustical and optical excitations. When the NM is thin compared with l_{sf}, the renormalization of the Gilbert damping vanishes for the acoustic modes, whereas for the optical modes, the renormalization is equally as large as for a single-FI|N system in which the NM is a perfect spin sink. A spin wave pumps a spatially dependent spin current that is determined by the wave number Q. When the wavelength $2\pi/Q$ is on the order of, or smaller than, the spin diffusion length, spin currents of opposite sign diffuse into each other and partially cancel each other out. Consequently, the spin-memory loss is greater for short-wavelength spin currents. This phenomenon leads to an effective spin-diffusion length in the NM that decreases for increasing values of Q. Thus, the dynamic coupling strength is reduced for short-wavelength spin waves. At some critical value of Q, the coupling becomes so weak that the acoustic- and optical-mode configurations are lost in favor of modes that are localized in one of the two FIs. At these values of Q, the interlayer dipole coupling is also dominated by the intralayer exchange coupling. For these high-wave-number modes, the system behaves similar to two separate FI|N($l_{\mathrm{sf}} = 0$) systems. When the two films are of different thicknesses, the exchange energies of the higher-order transverse $n > 1$ modes differ between the two layers. Because of the relatively small coupling attributable to spin pumping, the synchronization of these modes at $QL_1 \ll 1$ requires that the FI thicknesses be very similar. A small asymmetry breaks the synchronization; however, for larger $QL_1 \sim 1$, the modes can again become coupled through interlayer dipole interaction. This coupling arises in addition to the spin-pumping-induced coupling. At even larger Q, both the dipolar- and spin-pumping-induced couplings are reduced. Consequently, the modes of the two layers are desynchronized. Depending on the quality of the interface between the FIs and the strength of the spin-orbit coupling in the NM, additional effective surface fields may be present because of surface anisotropy energies. When surface anisotropy is present, the lowest-energy modes are localized at the FI|N surfaces. These modes couple in the same manner as the macrospin modes. For films that are much thicker than the decay length A/K_S, the energies of the surface modes do not depend on the film thickness. Consequently, the coupling of these modes is independent of the thickness of the two FIs. Similar to the simpler FI|N system, the damping enhancement may attain values as high as an order of magnitude larger than the intrinsic Gilbert damping. However, in the trilayer system, the presence of both acoustic and optical modes results in large variations in the effective damping within the same physical sample. Because of this wide range of effective damping, which spans a difference in $\Delta\alpha$ of several orders of magnitude as a function of Q, we suggest that trilayer modes should be measurable in an experimental setting. With more complicated FI structures in mind, we believe that this work may serve as a guide for experimentalists. The large variations in effective damping for different modes make the magnetic properties of the system detectable both with and without surface anisotropy. For spin waves, dipole-dipole interactions assist spin pumping in interlayer synchronization, which can be exploited in the design of future spintronic devices.

ACKNOWLEDGMENTS

We acknowledge support from EU-FET grant InSpin 612759 and the Research Council of Norway, Project No. 216700.

APPENDIX A: DIPOLE TENSOR

The dipole tensor in the $\zeta\eta\xi$ coordinate system, $\hat{G}(\xi)$ from Eq. (9), can be rotated in the xyz coordinate system using the rotation matrix

$$R = \begin{pmatrix} s_\theta & -c_\theta s_\theta & -c_\theta c_\phi \\ 0 & c_\phi & -s_\phi \\ c_\theta & s_\theta s_\phi & s_\theta c_\phi \end{pmatrix}, \tag{A1}$$

where we have introduced the shorthand notation $s_\theta \equiv \sin\theta$, $c_\theta \equiv \cos\theta$, and so forth. Thus, we obtain the following result:

$$\begin{aligned} \hat{\mathcal{G}}_{xyz} &= R\hat{G}R^T \\ &= \begin{pmatrix} s_\theta^2 G_{\xi\xi} - c_\phi s_{2\theta} G_{\xi\zeta} + c_\theta^2 c_\phi^2 G_{\zeta\zeta} & -s_\phi s_\theta G_{\xi\zeta} + s_\phi c_\phi c_\theta G_{\zeta\zeta} & s_\theta c_\theta G_{\xi\xi} - s_\theta c_\theta c_\phi^2 G_{\zeta\zeta} + c_\phi\left(s_\theta^2 - c_\theta^2\right) G_{\xi\zeta} \\ -s_\phi s_\theta G_{\xi\zeta} + s_\phi c_\phi c_\theta G_{\zeta\zeta} & s_\phi^2 G_{\zeta\zeta} & -s_\phi c_\theta G_{\xi\zeta} + s_\phi s_\theta c_\phi G_{\zeta\zeta} \\ s_\theta c_\theta G_{\xi\xi} - s_\theta c_\theta c_\phi^2 G_{\zeta\zeta} + c_\phi\left(s_\theta^2 - c_\theta^2\right) G_{\xi\zeta} & -s_\phi c_\theta G_{\xi\zeta} + s_\phi s_\theta c_\phi G_{\zeta\zeta} & c_\theta^2 G_{\xi\xi} + s_{2\theta} c_\phi G_{\xi\zeta} + c_\phi^2 s_\theta^2 G_{\zeta\zeta} \end{pmatrix}. \end{aligned} \tag{A2}$$

As we are considering the linear response regime, the equilibrium magnetization should be orthogonal to the dynamic deviation, $\mathbf{m}_i \cdot \hat{\mathbf{z}} = 0$. Thus, it is sufficient to retain only the xy part of $\hat{\mathcal{G}}_{xyz}$. Thus, we obtain the following result:

$$\hat{\mathcal{G}}_{xy} = \begin{pmatrix} s_\theta^2 G_{\xi\xi} - c_\phi s_{2\theta} G_{\xi\zeta} + c_\theta^2 c_\phi^2 G_{\zeta\zeta} & -s_\phi s_\theta G_{\xi\zeta} + s_\phi c_\phi c_\theta G_{\zeta\zeta} \\ -s_\phi s_\theta G_{\xi\zeta} + s_\phi c_\phi c_\theta G_{\zeta\zeta} & s_\phi^2 G_{\zeta\zeta} \end{pmatrix}. \tag{A3}$$

APPENDIX B: SPIN ACCUMULATION

The functions $\Gamma_1(\xi)$ and $\Gamma_2(\xi)$ are taken directly from Ref. [40] and modified to apply to the more complex magnetic texture model. Thus, we obtain the following result:

$$\begin{aligned} \Gamma_1(\xi) &\equiv \frac{\cosh(\xi/\tilde{l}_{\rm sf})}{\cosh(\xi/\tilde{l}_{\rm sf}) + \sigma \sinh(\xi/\tilde{l}_{\rm sf})/2g_\perp \tilde{l}_{\rm sf}}, \\ \Gamma_2(\xi) &\equiv \frac{\sinh(\xi/\tilde{l}_{\rm sf})}{\sinh(\xi/\tilde{l}_{\rm sf}) + \sigma \cosh(\xi/\tilde{l}_{\rm sf})/2g_\perp \tilde{l}_{\rm sf}}. \end{aligned} \tag{B1}$$

For $Ql_{\rm sf} \gg 1$, the effective spin diffusion length is shortened, $\Gamma_1 \to 1$ and $\Gamma_2 \to 0$ at the FI|N interfaces.

APPENDIX C: EFFECTIVE SPIN DIFFUSION LENGTH

Diffusion in the NM can be described as follows:

$$\partial_t \boldsymbol{\mu}_S = D\nabla^2 \boldsymbol{\mu}_S - \frac{1}{\tau_{\rm sf}} \boldsymbol{\mu}_S, \tag{C1}$$

where D is the diffusion constant, and $\tau_{\rm sf}$ is the spin-flip relaxation time. We assume that the FMR frequency is much smaller than the electron traversal time, $D/d_{\rm N}^2$, and the spin-flip relaxation rate, $1/\tau_{\rm sf}$ [40]. Thus, the left-hand side of Eq. (C1) can be neglected. In linear response, the spin accumulation, which is a direct consequence of spin pumping, must be proportional to the rate of change of magnetization at the FI|N interfaces. We perform the same Fourier transform, as on the magnetization, such that $\boldsymbol{\mu} \sim \exp\{i(\omega t - Q\zeta)\}$. The spin diffusion equation then takes the form

$$\partial_\xi^2 \boldsymbol{\mu}_S = \left(Q^2 + \frac{1}{D\tau_{\rm sf}}\right) \boldsymbol{\mu}_S. \tag{C2}$$

The spin diffusion length becomes $l_{\rm sf} = \sqrt{D\tau_{\rm sf}}$. We introduce the effective spin diffusion length as follows: $\tilde{l}_{\rm sf} = l_{\rm sf}/\sqrt{1 + (Ql_{\rm sf})^2}$ one gets

$$\partial_\xi^2 \boldsymbol{\mu}_S = \frac{1}{\tilde{l}_{\rm sf}^2} \boldsymbol{\mu}_S. \tag{C3}$$

APPENDIX D: SYNCHRONIZATION WITH VANISHING SPIN PUMPING

We identify the relative contributions of spin pumping and interlayer dipole coupling by considering the results of the numerical calculation in Sec. IV A in the absence of spin pumping and the associated coupling ($g_\perp = 0$). In Fig. 6, we show the relative amplitude between the two layers for the four lowest energy modes. The frequencies of the two uniform modes are independent of the thickness and are therefore synchronized even at $Q \to 0$, where the interlayer dipole coupling becomes small. Comparing this calculation to the same calculation with spin pumping shows that the synchronization observed at $QL_1 \sim 1$ primarily results from dipole coupling.

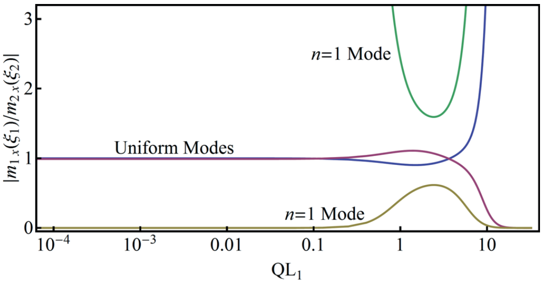

FIG. 6. (Color online) FI(100 nm)|N(50 nm)|FI(101 nm), BVMSW without spin pumping, showing relative amplitude of the out-of-plane magnetizations along x at the edges of FI1|N and FI2|N as functions of QL_1; blue and yellow (red and green) lines show acoustical (optical) modes.

[1] C. Kittel, Phys. Rev. **73**, 155 (1948).

[2] R. W. Damon and J. R. Eshbach, J. Phys. Chem. Solids **19**, 308 (1961).

[3] V. Cherepanov, I. Kolokolov, and V. L'vov, Phys. Rep. **229**, 81 (1993).

[4] A. Brataas, A. D. Kent, and H. Ohno, Nat. Mater. **11**, 372 (2012).

[5] G. Binasch, P. Grünberg, F. Saurenbach, and W. Zinn, Phys. Rev. B **39**, 4828 (1989).

[6] L. Berger, Phys. Rev. B **54**, 9353 (1996).

[7] J. C. Slonczewski, J. Magn. Magn. Mater. **159**, L1 (1996).

[8] Y. Kajiwara, K. Harii, S. Takahashi, J. Ohe, K. Uchida, M. Mizuguchi, H. Umezawa, H. Kawai, K. Ando, K. Takanashi, S. Maekawa, and E. Saito, Nature (London) **464**, 262 (2010).

[9] C. W. Sandweg, Y. Kajiwara, K. Ando, E. Saitoh, and B. Hillebrands, Appl. Phys. Lett. **97**, 252504 (2010).

[10] C. W. Sandweg, Y. Kajiwara, A. V. Chumak, A. A. Serga, V. I. Vasyuchka, M. B. Jungfleisch, E. Saitoh, and B. Hillebrands, Phys. Rev. Lett. **106**, 216601 (2011).

[11] B. Heinrich, C. Burrowes, E. Montoya, B. Kardasz, E. Girt, Y.-Y. Song, Y. Sun, and M. Wu, Phys. Rev. Lett. **107**, 066604 (2011).

[12] L. H. Vilela-Leao, C. Salvador, A. Azevedo, and S. M. Rezende, Appl. Phys. Lett. **99**, 102505 (2011).

[13] C. Burrowes, B. Heinrich, B. Kardasz, E. A. Montoya, E. Girt, Yiyan Sun, Young-Yeal Song, and Mingzhong Wu, Appl. Phys. Lett. **100**, 092403 (2012).

[14] S. M. Rezende, R. L. Rodríguez-Suárez, M. M. Soares, L. H. Vilela-Leão, D. Ley Domínguez, and A. Azevedo, Appl. Phys. Lett. **102**, 012402 (2013).

[15] P. Pirro, T. Brächer, A. V. Chumak, B. Lägel, C. Dubs, O. Surzhenko, P. Görnert, B. Leven, and B. Hillebrands, Appl. Phys. Lett. **104**, 012402 (2014).

[16] H. Nakayama, M. Althammer, Y.-T. Chen, K. Uchida, Y. Kajiwara, D. Kikuchi, T. Ohtani, S. Geprägs, M. Opel, S. Takahashi, R. Gross, G. E. W. Bauer, S. T. B. Goennenwein, and E. Saitoh, Phys. Rev. Lett. **110**, 206601 (2013).

[17] C. Hahn, G. de Loubens, O. Klein, M. Viret, V. V. Naletov, and J. Ben Youssef, Phys. Rev. B **87**, 174417 (2013).

[18] N. Vlietstra, J. Shan, V. Castel, B. J. van Wees, and J. Ben Youssef, Phys. Rev. B **87**, 184421 (2013).

[19] A. Brataas, Physics **6**, 56 (2013).

[20] A. Hamadeh, O. d'Allivy Kelly, C. Hahn, H. Meley, R. Bernard, A. H. Molpeceres, V. V. Naletov, M. Viret, A. Anane, V. Cros, S. O. Demokritov, J. L. Prieto, M. Muñoz, G. de Loubens, and O. Klein, arXiv:1405.7415.

[21] J. Xiao and G. E. W. Bauer, Phys. Rev. Lett. **108**, 217204 (2012).

[22] Y. Zhou, H. J. Jiao, Y. T. Chen, G. E. W. Bauer, and J. Xiao, Phys. Rev. B **88**, 184403 (2013).

[23] T. Schneider, A. A. Serga, B. Leven, B. Hillebrands, R. L. Stamps, and M. P. Kostylev, Appl. Phys. Lett. **92**, 022505 (2008).

[24] Y.-T. Chen, S. Takahashi, H. Nakayama, M. Althammer, S. T. B. Goennenwein, E. Saitoh, and G. E. W. Bauer, Phys. Rev. B **87**, 144411 (2013).

[25] Y. M. Lu, J. W. Cai, S. Y. Huang, D. Qu, B. F. Miao, and C. L. Chien, Phys. Rev. B **87**, 220409 (2013).

[26] V. V. Kruglyak, S. O. Demokritov, and D. Grundler, J. Phys. D. Appl. Phys. **43**, 264001 (2010).

[27] R. Urban, G. Woltersdorf, and B. Heinrich, Phys. Rev. Lett. **87**, 217204 (2001).

[28] S. Mizukami, Y. Ando, and T. Miyazaki, J. Magn. Magn. Mater. **239**, 42 (2002).

[29] Y. Tserkovnyak, A. Brataas, and G. E. W. Bauer, Phys. Rev. Lett. **88**, 117601 (2002).

[30] A. Brataas, Y. Tserkovnyak, G. E. W. Bauer, and B. I. Halperin, Phys. Rev. B **66**, 060404 (2002).

[31] Y. Tserkovnyak, A. Brataas, G. E. W. Bauer, and B. I. Halperin, Rev. Mod. Phys. **77**, 1375 (2005).

[32] A. Kapelrud and A. Brataas, Phys. Rev. Lett. **111**, 097602 (2013).

[33] B. Heinrich, Y. Tserkovnyak, G. Woltersdorf, A. Brataas, R. Urban, and G. E. W. Bauer, Phys. Rev. Lett. **90**, 187601 (2003).

[34] B. A. Kalinikos and A. N. Slavin, J. Phys. C **19**, 7013 (1986).

[35] A. A. Serga, A. V. Chumak, and B. Hillebrands, J. Phys. D: App. Phys. **43**, 264002 (2010).

[36] M. Vohl, J. Barnaś, and P. Grünberg, Phys. Rev. B **39**, 12003 (1989).

[37] B. Heinrich (private communication).

[38] A. Brataas, Yu. V. Nazarov, and G. E. W. Bauer, Phys. Rev. Lett. **84**, 2481 (2000).

[39] M. Althammer, S. Meyer, H. Nakayama, M. Schreier, S. Altmannshofer, M. Weiler, H. Huebl, S. Geprägs, M. Opel, R. Gross, D. Meier, C. Klewe, T. Kuschel, J.-M. Schmalhorst, G. Reiss, L. Shen, A. Gupta, Y.-T. Chen, G. E. W. Bauer, E. Saitoh, and S. T. B. Goennenwein, Phys. Rev. B **87**, 224401 (2013).

[40] H. Skarsvåg, G. E. W. Bauer, and A. Brataas, Phys. Rev. B **90**, 054401 (2014).

[41] A. Kapelrud and A. Brataas (unpublished).

[42] M. B. Jungfleisch, V. Lauer, R. Neb, A. V. Chumak, and B. Hillebrands, Appl. Phys. Lett. **103**, 022411 (2013).

[43] D. Giancoli, *Physics for Scientists and Engineers*, 4th ed. (Prentice Hall, Englewood, NJ, 2009), Chap. 25.

Paper 3

Spin pumping, dissipation, and direct and alternating inverse spin Hall effects in magnetic-insulator/normal-metal bilayers
Phys. Rev. B 95, 214413 (2017) - Published June 20, 2017

PHYSICAL REVIEW B **95**, 214413 (2017)

Spin pumping, dissipation, and direct and alternating inverse spin Hall effects in magnetic-insulator/normal-metal bilayers

André Kapelrud and Arne Brataas
Department of Physics, Norwegian University of Science and Technology, NO-7491 Trondheim, Norway

(Received 21 December 2016; revised manuscript received 6 April 2017; published 20 June 2017)

We theoretically consider the spin-wave mode- and wavelength-dependent enhancement of the Gilbert damping in magnetic insulator–normal metal bilayers due to spin pumping as well as the enhancement's relation to direct and alternating inverse spin Hall voltages in the normal metal. In the long-wavelength limit, including long-range dipole interactions, the ratio of the enhancement for transverse volume modes to that of the macrospin mode is equal to two. With an out-of-plane magnetization, this ratio decreases with both an increasing surface anisotropic energy and mode number. If the surface anisotropy induces a surface state, the enhancement can be an order of magnitude larger than for the macrospin. With an in-plane magnetization, the induced dissipation enhancement can be understood by mapping the anisotropy parameter to the out-of-plane case with anisotropy. For shorter wavelengths, we compute the enhancement numerically and find good agreement with the analytical results in the applicable limits. We also compute the induced direct- and alternating-current inverse spin Hall voltages and relate these to the magnetic energy stored in the ferromagnet. Because the magnitude of the direct spin Hall voltage is a measure of spin dissipation, it is directly proportional to the enhancement of Gilbert damping. The alternating spin Hall voltage exhibits a similar in-plane wave-number dependence, and we demonstrate that it is greatest for surface-localized modes.

DOI: 10.1103/PhysRevB.95.214413

I. INTRODUCTION

In magnonics, one goal is to utilize spin-based systems for interconnects and logic circuits [1]. In previous decades, the focus was to gain control over these systems by exploiting long-range dipole interactions in combination with geometrical shaping. However, the complex nature of the nonlinear magnetization dynamics persistently represents a challenge in using geometrical shaping alone to realize a variety of desired properties [1].

In magnonic systems, a unique class of materials consists of magnetic insulators. Magnetic insulators are electrically insulating, but localized magnetic moments couple to form a long-range order. The prime example is *yttrium iron garnet* (YIG). YIG is a complex crystal [2] in the Garnet family, where Fe^{3+} ions at different sites in the unit cell contribute to an overall ferrimagnetic ordering. What differentiates YIG from other ferromagnetic (ferrimagnetic) systems is its extremely low intrinsic damping. The Gilbert damping parameter measured in YIG crystals is typically two orders of magnitude smaller than that measured in conventional metallic ferromagnets (Fe, Co, Ni, and alloys thereof).

The recent discovery that the spin waves in magnetic insulators strongly couple to spin currents in adjacent normal metals has reinvigorated the field of magnonics [3–12]. Although there are no mobile charge carriers in magnetic insulators, spin currents flow via spin waves and can be transferred to itinerant spin currents in normal metals via spin transfer and spin pumping [13,14]. These interfacial effects open new doors with respect to local excitation and detection of spin waves in magnonic structures. Another key element is that we can transfer knowledge from conventional spintronics to magnonics, opening possibilities for novel physics and technologies. Traditionally, spin-wave excitation schemes have focused on the phenomenon of resonance or the use of Ørsted fields from microstrip antennas.

A cornerstone for utilizing these systems is to establish a good understanding of how the itinerant electrons in normal metals couple across interfaces with spin-wave dynamics in magnetic insulators. Good models for addressing uniform (macrospin) magnetization that agrees well with experiments have been previously developed [13–15]. We recently demonstrated that for long-wavelength magnons the enhanced Gilbert damping for the transverse volume modes is twice that of the uniform mode, and for surface modes, the enhancement can be more than ten times stronger. These results are consistent with the theory of current-induced excitations of the magnetization dynamics [16] because spin pumping and spin transfer are related by Onsager reciprocity relations [17]. Moreover, mode- and wave-vector-dependent spin pumping and spin Hall voltages have been clearly observed experimentally [4].

In this paper, we extend our previous findings [18] in the following four aspects. (i) We compute the influence of the spin backflow on the enhanced spin dissipation. (ii) We also compute the induced direct and alternating inverse spin Hall voltages. We then relate these voltages to the enhanced Gilbert damping and the relevant energies for the magnetization dynamics. The induced voltages give additional information about the spin-pumping process, which can also be directly measured. (iii) We also provide additional information on the effects of interfacial pinning of different types in various field geometries. (iv) Finally, we explain in more detail how the numerical analysis is conducted for a greater number of in-plane wave numbers.

It was discovered [19–23] and later quantitatively explained [13,15,24,25] that if a dynamic ferromagnetic material is put in contact with a normal metal, the magnetization dynamics will exert a torque on the spins of electrons in the immediate vicinity of the magnet. This effect is known as spin pumping (SP) [13,15,25]. As the electrons are carried away from the ferromagnet-normal metal interface, the electrons spin with respect to each other, causing an overall loss of angular momentum. The scattering formalism and a dynamic magnetic susceptibility equivalently describe the resulting pumped spin current [26,27]. The inverse effect, in which a spin-polarized current can affect the magnetization of a ferromagnet, is called spin-transfer torque (STT) [14,28,29].

The discovery that a precessing magnetization in magnetic insulators [3], such as YIG, also pumps spins into an adjacent metal layer was made possible by the fact that the mixing conductance in YIG-normal metal systems is of such a size that the extra dissipation of the magnetization due to the spin pumping is of the same order of magnitude as the intrinsic Gilbert damping. A consequence of this effect is that the dissipation of the magnetization dynamics is enhanced relative to that of a system in which the normal metal contact is removed. The detection of the antiferromagnet-paramagnet phase transition in CoO is a recent development of spin pumping from YIG [30]. The CoO spacer layer is sandwiched between YIG and a normal metal. Distinguishing the dynamics in the antiferromagnet from the dynamics from the YIG-normal metal system also requires a robust understanding of the spin pumping properties of the YIG-normal metal bilayer system.

This paper is organized in the following manner. Section II presents the equation of motion for the magnetization dynamics and the currents in the normal metal and the appropriate boundary conditions, both for general nonlinear excitations and in the fully linear response regime. In Sec. III, we derive approximate solutions to the linearized problem, demonstrating how the magnetization dissipation is enhanced by the presence of an adjacent metal layer. Section IV presents our numerical method and results. Finally, we summarize our findings in Sec. V.

II. EQUATIONS OF MOTION

The equation of motion for the magnetization is given by the Landau-Lifshitz-Gilbert equation [31] (presented here in CGS units)

$$\frac{\partial \mathbf{M}}{\partial t} = -\gamma \mathbf{M} \times \mathbf{H}_{\text{eff}} + \frac{\alpha}{M_s} \mathbf{M} \times \frac{\partial \mathbf{M}}{\partial t}, \tag{1}$$

where $\gamma = |g\mu_B/\hbar|$ is the magnitude of the gyromagnetic ratio; $g \approx 2$ is the Landé g-factor for the localized electrons in the ferromagnetic insulator (FI), and α is the dimensionless Gilbert damping parameter. In equilibrium, the magnitude of the magnetization is assumed to be close to the saturation magnetization M_s. The magnetization is directed along the z axis in equilibrium. Out of equilibrium, we assume that we have a small transverse dynamic magnetization component, such that

$$\mathbf{M} = \mathbf{M}(\mathbf{r},t) = \mathbf{M}_s + \mathbf{m}(\mathbf{r},t) = M_s \hat{\mathbf{z}} + \mathbf{m}(\mathbf{r},t), \tag{2}$$

where $|\mathbf{m}| \ll M_s$ and $\mathbf{m} \cdot \hat{\mathbf{z}} = 0$. Furthermore, we assume that the dynamic magnetization can be described by a plane wave traveling along the in-plane ζ axis. In the (ξ,η,ζ) coordinate system (see Fig. 1), we have

$$\mathbf{m}(\mathbf{r},t) = \mathbf{m}(\xi,\zeta,t) = \mathbf{m}_Q(\xi) e^{i(\omega t - Q\zeta)}, \tag{3}$$

where ω is the harmonic angular frequency, Q is the in-plane wave number, and $\mathbf{m}_Q(\xi) = X_Q(\xi)\hat{\mathbf{x}} + Y_Q(\xi)\hat{\mathbf{y}}$, where X_Q and Y_Q are complex functions. Note that $\mathbf{m}$ is independent of the η coordinate due to translational invariance. The in-plane wave number, Q, can be engineered by lateral dimensioning of the sample in such a way as to induce standing waves in the film plane [4,32].

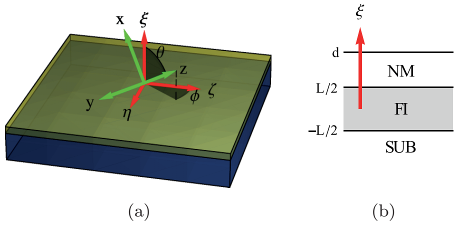

FIG. 1. (a) The coordinate system. $\hat{\boldsymbol{\xi}}$ is the film normal and $\hat{\boldsymbol{\zeta}}$ is the spin-wave propagation direction. $\xi\eta\zeta$ form a right-handed coordinate system. The $\hat{\mathbf{z}}$ axis is the direction of the magnetization in equilibrium, such that xy is the magnetization-precession plane. (b) The film stack is in the normal direction.

$\mathbf{H}_{\text{eff}}$ is the effective field, given as the functional derivative of the free energy [31,33]

$$\mathbf{H}_{\text{eff}}(\mathbf{r},t) = -\frac{\delta U[\mathbf{M}(\mathbf{r},t)]}{\delta \mathbf{M}(\mathbf{r},t)} = \mathbf{H}_i + \frac{2A}{M_s^2}\nabla^2 \mathbf{M}(\mathbf{r},t) + 4\pi \int_{-\frac{L}{2}}^{\frac{L}{2}} d\xi' \, \widehat{\mathcal{G}}_{xy}(\xi - \xi')\mathbf{m}(\xi',\zeta,t), \tag{4}$$

where $\mathbf{H}_i$ is the internal field, which is composed of the applied external field and the static demagnetization field. The direction of $\mathbf{H}_i$ defines the z axis (see Fig. 1). The second term of Eq. (4) is the field, $\mathbf{H}_{ex}$, induced by the exchange interaction (assuming cubic symmetry), where A is the exchange stiffness parameter. The last term is the dynamic field, $\mathbf{h}_d(\mathbf{r},t)$, induced by dipole-dipole interactions, where $\widehat{\mathcal{G}}_{xy}$ is the upper 2×2 part of the dipole-dipole tensorial Green's function $\widehat{\mathcal{G}}_{\xi\eta\zeta}$ in the magnetostatic approximation (see Ref. [34]) rotated to the xyz coordinate system (see Appendix for coordinate-transformation matrices) [35].

The effect of the dipolar interaction on the spin-wave spectrum depends on the orientation of the internal field with respect to both the interface normal of the thin film, $\hat{\boldsymbol{\xi}}$, and the in-plane spin-wave propagation direction, $\hat{\boldsymbol{\zeta}}$. Traditionally, the three main configurations are the out-of-plane configuration ($\theta = 0$), in the *forward volume magnetostatic wave* (FVMSW) geometry [see Fig. 2(a)]; the in-plane and parallel-to-$\hat{\boldsymbol{\zeta}}$ configuration, in the *backward volume magnetostatic wave* (BVMSW) geometry [see Fig. 2(b)]; and the in-plane and perpendicular-to-$\hat{\boldsymbol{\zeta}}$ configuration, in the *magnetostatic surface wave* (MSSW) geometry [see Fig. 2(c)] [1,35–39]. Here, the term "forward volume modes" denotes modes that have positive group velocities for all values of QL, whereas backward volume modes can have negative group velocities in the range of QL, where both exchange and dipolar interactions are significant. Volume modes are modes in which $\mathbf{m}_Q(\xi)$ is distributed across the thickness of the entire film, whereas the surface modes are localized more closely near an interface.

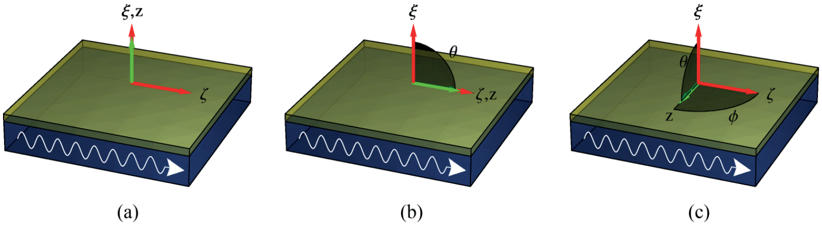

FIG. 2. Laboratory field configurations, i.e., directions of $\hat{\mathbf{z}}$ (green arrow) in relation to film normal $\hat{\boldsymbol{\xi}}$ and the spin-wave propagation direction $\hat{\boldsymbol{\zeta}}$, resulting in the different geometries: (a) FVMSW geometry, (b) BVMSW geometry, and (c) MSSW geometry.

A. Spin-pumping torque

We consider a *ferromagnetic insulator* (FI) in contact with a *normal metal* (NM) (see Fig. 1). If the magnetization in the FI close to the interface is precessing around the effective field, electron spins in the NM reflected at the interface will start to precess due to the local exchange coupling to the magnetization in the FI. The reflected electrons carry the angular momentum away from the interface, where the spin information can get lost through dephasing of the spins within a typical spin diffusion length l_{sf}. This loss of angular momentum manifests itself as an increased local damping of the magnetization dynamics in the FI. The magnetization dissipation due to the spin-pumping effect can be taken into account by adding the local dissipation torque [15],

$$\boldsymbol{\tau}_{\mathrm{sp}} = \frac{\gamma\hbar^2 g_\perp}{2e^2 M_s^2}\delta\left(\xi - \frac{L}{2}\right)\mathbf{M}(\mathbf{r},t) \times \frac{\partial \mathbf{M}(\mathbf{r},t)}{\partial t}, \tag{5}$$

to the right-hand side (rhs) of Eq. (1). Here, $g_\perp$ is the real part of the spin-mixing conductance per area, and e is the electron charge. We neglect the contribution from the imaginary part of the mixing conductance, because this has been shown to be significantly smaller than that of the real part, in addition to affecting only the gyromagnetic ratio [15]. The spin-current density pumped from the magnetization layer is thus given by

$$\mathbf{j}_{\mathrm{sp}}^{(s)} = -\frac{\hbar^2 g_\perp}{2e^2 M_s^2}\left[\mathbf{M}(\mathbf{r},t) \times \frac{\partial \mathbf{M}(\mathbf{r},t)}{\partial t}\right]_{\xi = L/2}, \tag{6}$$

in units of erg. Next, we will see how the spin pumping affects the boundary conditions.

B. Spin-pumping boundary conditions

Following the procedure of Rado and Weertman [40], we integrate Eq. (1) with the linear expansion of Eq. (2) over a small pill-box volume straddling one of the interfaces of the FI. Upon letting the pill box thickness tend to zero, only the surface torques of the equation survive. Accounting for the direction of the outward normal of the lid on the different top and bottom interfaces, we arrive at the exchange-pumping boundary condition

$$\left(\frac{2A}{M_s^2}\mathbf{M} \times \frac{\partial \mathbf{M}}{\partial \xi} + \frac{\hbar^2}{2e^2 M_s^2} g_\perp \mathbf{M} \times \frac{\partial \mathbf{m}}{\partial t}\right)_{\xi = \pm L/2} = 0. \tag{7}$$

There is no spin current pumped at the interface to the insulating substrate; thus a similar derivation results in a boundary condition that gives an unpinned magnetization,

$$\left.\frac{\partial \mathbf{M}(\mathbf{r},t)}{\partial \xi}\right|_{\xi = -L/2} = 0. \tag{8}$$

In the next section, we will generalize the boundary conditions of Eq. (7) by also considering possible surface-anisotropy energies.

1. Including surface anisotropy:

In the presence of surface anisotropy at an interface with an *easy-axis* (EA) pointing along the direction $\hat{\mathbf{n}}$, the surface free energy is

$$U_s[\mathbf{M}(\mathbf{r},t)] = \int dV\, K_s\left[1 - \left(\frac{\mathbf{M}(\mathbf{r},t)\cdot\hat{\mathbf{n}}}{M_s}\right)^2\right]\delta(\xi - \xi_i), \tag{9}$$

where K_s is the surface-anisotropy energy density at the interface, which is assumed to be constant; $\hat{\mathbf{n}}$ is the direction of the anisotropy *easy* axis; and ξ_i is the transverse coordinate of the interface. The contribution from the EA surface-anisotropy energy to the effective field is determined by

$$\mathbf{H}_s = -\frac{\delta U_s[\mathbf{M}(\mathbf{r},t)]}{\delta \mathbf{M}(\mathbf{r},\mathbf{t})} = \frac{2K_s}{M_s^2}(\mathbf{M}\cdot\hat{\mathbf{n}})\,\delta(\xi - \xi_i)\hat{\mathbf{n}}.$$

However, if we have an *easy-plane* (EP) surface anisotropy with $\hat{\mathbf{n}}$ being the direction of the *hard* axis, the effective field is the same as that for the EA case, except for a change of sign of K_s. We unify both cases by defining $K_s > 0$ to imply that we have an EA surface anisotropy with its easy axis along $\hat{\mathbf{n}}$, whereas $K_s < 0$ implies that we have an EP surface anisotropy with its hard axis along $\hat{\mathbf{n}}$.

Following the approach from Sec. II B, the total boundary condition, including exchange, pumping, and surface anisotropy, becomes

$$\left[\pm\frac{2A}{M_s^2}\mathbf{M} \times \frac{\partial \mathbf{M}}{\partial \xi} - \frac{2K_s}{M_s^2}(\mathbf{M}\cdot\hat{\mathbf{n}})(\mathbf{M}\times\hat{\mathbf{n}}) + \frac{\hbar^2}{2e^2 M_s^2} g_\perp \mathbf{M} \times \frac{\partial \mathbf{M}}{\partial t}\right]_{\xi = \pm L/2} = 0, \tag{10}$$

where the positive (negative) sign in front of the exchange term indicates that the bulk FI is located below (above) the interface coordinate.

C. Linearization

We linearize the equation of motion using Eq. (2) with respect to the dynamic magnetization $\mathbf{m}$. The linearized equation of motion for the bulk magnetization, Eq. (1), becomes [35]

$$\left\{ i\frac{\omega}{\omega_M}\begin{pmatrix} \alpha & -1 \\ 1 & \alpha \end{pmatrix} + \mathbb{1}\left[\frac{\omega_H}{\omega_M} + 8\pi\frac{\gamma^2 A}{\omega_M^2}\left(Q^2 - \frac{d^2}{d\xi^2}\right)\right]\right\}\mathbf{m}_Q(\xi) = \int_{-\frac{L}{2}}^{\frac{L}{2}} d\xi'\,\widehat{\mathcal{G}}_{xy}(\xi - \xi')\mathbf{m}_Q(\xi'), \tag{11}$$

where $\omega_H \equiv \gamma H_i$, $\omega_M \equiv 4\pi\gamma M_s$, and $\mathbb{1} = \left(\begin{smallmatrix} 1 & 0 \\ 0 & 1 \end{smallmatrix}\right)$.

Next, we linearize the boundary conditions of Eq. (10). We choose the anisotropy axis to be perpendicular to the film plane, $\hat{\mathbf{n}} = \hat{\boldsymbol{\xi}}$, which in the xyz coordinate system is given by $\hat{\boldsymbol{\xi}}_{xyz} = (\sin\theta, 0, \cos\theta)$, where θ is the angle between the z axis and the film normal (see Fig. 1). The finite surface anisotropy forces the magnetization to be either perpendicular or coplanar with the film surface so that $\theta = 0, \pi/2, \pi$. Linearizing to first order in the dynamic magnetization, we arrive at the linearized boundary conditions for the top interface:

$$\left(L\frac{\partial}{\partial\xi} + i\frac{\omega}{\omega_M}\rho + d\cos(2\theta)\right)m_{Q,x}(\xi)|_{\xi=\frac{L}{2}} = 0, \tag{12a}$$

$$\left(L\frac{\partial}{\partial\xi} + i\frac{\omega}{\omega_M}\rho + d\cos^2(\theta)\right)m_{Q,y}(\xi)|_{\xi=\frac{L}{2}} = 0, \tag{12b}$$

where $d \equiv LK_s/A$ is the dimensionless surface-pinning parameter that relates the exchange to the surface anisotropy and the film thickness and $\rho \equiv \omega_M L\hbar^2 g_\perp/4Ae^2$ is a dimensionless constant relating the exchange stiffness and the spin-mixing conductance.

D. Spin accumulation in NM and spin backflow

The pumped spin current induces a spin accumulation, $\boldsymbol{\mu}^{(\mathbf{s})} = \mu^{(s)}\hat{\mathbf{s}}$, in the normal metal. Here, $\hat{\mathbf{s}}$ is the spin-polarization axis, and $\mu^{(s)} = (\mu_\uparrow - \mu_\downarrow)/2$ is half of the difference between chemical potentials for spin-up and spin-down electrons in the NM.

As the spin accumulation is a direct consequence of the spin dynamics in the FI [see Eq. (6)], the spin accumulation cannot change faster than the magnetization dynamics at the interface. Thus, assuming that spin-flip processes in the NM are must faster than the typical precession frequency of the magnetization in the FI [25], we can neglect the precession of the spin accumulation around the applied field and any decay in the NM. With this assumption, the spin-diffusion equation $\frac{\partial\boldsymbol{\mu}^{(\mathbf{s})}}{\partial t} = D\nabla^2\boldsymbol{\mu}^{(\mathbf{s})} - \frac{\boldsymbol{\mu}^{(\mathbf{s})}}{\tau_{\mathrm{sf}}}$, where D is the spin-diffusion constant, and τ_{sf} is the material-specific average spin-flip relaxation time, becomes

$$\boldsymbol{\mu}^{(\mathbf{s})} \approx l_{\mathrm{sf}}^2\nabla^2\boldsymbol{\mu}^{(\mathbf{s})}, \tag{13}$$

where $l_{\mathrm{sf}} \equiv \sqrt{\tau_{\mathrm{sf}}D}$ is the average spin-flip relaxation length.

The spin accumulation results in a backflowing spin-current density, given by

$$\mathbf{j}_{\mathrm{bf}}^{(s)}(L/2) = \frac{\hbar g_\perp}{e^2M_s^2}[\mathbf{M}(\mathbf{r},t) \times (\mathbf{M}(\mathbf{r},t) \times \boldsymbol{\mu}^{(\mathbf{s})}(\mathbf{r},t))]_{\xi=L/2}, \tag{14}$$

where the positive sign indicates flow from the NM into the FI. This spin current creates an additional spin-transfer torque on the magnetization at the interface:

$$\boldsymbol{\tau}_{\mathrm{bf}} = -\frac{\gamma\hbar g_\perp}{e^2M_s^2}\delta\left(\xi - \frac{L}{2}\right)\mathbf{M}(\mathbf{r},t) \times (\mathbf{M}(\mathbf{r},t) \times \boldsymbol{\mu}^{(\mathbf{s})}). \tag{15}$$

Because the spin accumulation is a direct result of the pumped spin current, it must have the same orientation as the $\mathbf{M}(\mathbf{r},t) \times \partial_t\mathbf{M}(\mathbf{r},t)$ term in Eq. (5). That term is comprised of two orthogonal components: the first-order term $M_s\hat{\mathbf{z}} \times \dot{\mathbf{m}}$, in the xy plane, and the second-order term $\mathbf{m} \times \dot{\mathbf{m}}$, oriented along $\hat{\mathbf{z}}$. Because the magnetization is a real quantity, care must be taken when evaluating the second-order term. Using Eq. (3), the second-order pumped spin current is proportional to

$$\mathrm{Re}\{\mathbf{m}\} \times \partial_t\mathrm{Re}\{\mathbf{m}\}|_{\xi=L/2} = e^{-2\mathrm{Im}\{\omega\}t}\mathrm{Re}\{\omega\}\hat{\mathbf{z}}[\mathrm{Im}X_Q\mathrm{Re}Y_Q - \mathrm{Re}X_Q\mathrm{Im}Y_Q], \tag{16}$$

which is a decaying *direct-current* (DC) term. This is in contrast to the first-order term, which is an *alternating-current* (AC) term. Thus we write the spin accumulation as

$$\boldsymbol{\mu}^{(\mathbf{s})} = \mu_{\mathrm{AC}}^{(s)}(\hat{\mathbf{z}} \times \hat{\mathbf{m}}_t) + \mu_{\mathrm{DC}}^{(s)}\hat{\mathbf{z}}, \tag{17}$$

where we have used the shorthand notation $\mathbf{m}_t = \dot{\mathbf{m}}(\xi = L/2)$, such that $\hat{\mathbf{m}}_t = \mathbf{m}_t/|\mathbf{m}_t|$, which in general is not parallel to $\mathbf{m}$ but guaranteed to lie in the xy plane. Inserting Eq. (17) into Eq. (13) gives one equation each for the AC and DC components of the spin accumulation,

$$\frac{\partial^2\mu_j^{(s)}}{\partial\xi^2} = l_{\mathrm{sf},j}^{-2}\mu_j^{(s)}, \tag{18}$$

where j denotes either the AC or DC case and $l_{\mathrm{sf,DC}} = l_{\mathrm{sf}}$ while $l_{\mathrm{sf,AC}} = l_{\mathrm{sf}}(1 + l_{\mathrm{sf}}^2Q^2)^{-1/2}$ because $\mathbf{m}_t \propto \exp(i(\omega t - Q\zeta))$. Equation (18) can be solved by demanding spin-current conservation at the NM boundaries: at the free surface of the NM, there can be no crossing spin current; thus the ξ component of the spin-current density must vanish there, $\partial_\xi\mu_j^{(s)}|_{\xi=L/2+d} = 0$. Similarly, by applying conservation of angular momentum at the FI-NM interface, the net spin-current density crossing the interface, due to spin pumping and backflow, must equal the spin current in the NM layer, giving

$$\left[-\frac{\hbar^2 g_\perp}{2e^2M_s^2}\mathbf{M} \times \frac{\partial\mathbf{M}}{\partial t} + \frac{\hbar g_\perp}{e^2M_s^2}\mathbf{M} \times (\mathbf{M} \times \boldsymbol{\mu}^{(\mathbf{s})})\right]_{\xi=L/2} = -\frac{\hbar\sigma}{2e^2}\partial_\xi\boldsymbol{\mu}^{(\mathbf{s})}|_{\xi=L/2}, \tag{19}$$

TABLE I. Typical values for the parameters used in the calculations [6,7,11,42,43].

Parameter	Value	Unit
A	3.66×10^{-7}	$\mathrm{erg\,cm^{-1}}$
α	3×10^{-4}	–
K_s	0.05	$\mathrm{erg\,cm^{-2}}$
$g_\perp$	8.18×10^{22}	$\mathrm{cm^{-1}\,s^{-1}}$
γ	1.76×10^{7}	$\mathrm{G^{-1}\,s^{-1}}$
$4\pi M_s$	1750	G
σ	8.45×10^{16}	$\mathrm{s^{-1}}$
d	50	nm
l_{sf}	7.7	nm
Θ	0.1	–

where σ is the conductivity of the NM. Using these boundary conditions, we recover the solutions (see, e.g., Refs. [25,41])

$$\mu_j^{(s)} = \mu_{j,0}^{(s)} \frac{\sinh\left(l_{\mathrm{sf},j}^{-1}[\xi - (L/2+d)]\right)}{\sinh\left(-\frac{d}{l_{\mathrm{sf},j}}\right)}, \tag{20}$$

where $\mu_{j,0}^{(s)}$ is time dependent and depends on the ζ coordinate only in the AC case. We find that the AC and DC spin accumulations $\mu_{j,0}^{(s)}$ are given by

$$\mu_{\mathrm{AC},0}^{(s)} = -\frac{\hbar}{2}\frac{m_t}{M_s}\left[1 + \frac{\sigma}{2g_\perp l_{\mathrm{sf,AC}}}\coth\left(\frac{d}{l_{\mathrm{sf,AC}}}\right)\right]^{-1}, \tag{21}$$

$$\mu_{\mathrm{DC},0}^{(s)} = -\frac{l_{\mathrm{sf}}\hbar}{\sigma M_s^2}\tilde{g}_\perp \tanh\left(\frac{d}{l_{\mathrm{sf}}}\right)\hat{\mathbf{z}}\cdot[\mathbf{m}\times\dot{\mathbf{m}}]_{\xi=L/2}, \tag{22}$$

where $\tilde{g}_\perp$ is a renormalized mixing conductance, which is given by

$$\tilde{g}_\perp = g_\perp\left\{1 - \left[1 + \frac{\sigma}{2g_\perp l_{\mathrm{sf,AC}}}\coth\left(\frac{d}{l_{\mathrm{sf,AC}}}\right)\right]^{-1}\right\}. \tag{23}$$

This scaling of $g_\perp$ occurring in the DC spin accumulation originates from the second-order spin backflow due to the AC spin accumulation that is generated in the normal metal.

Adding both the spin-pumping and the backflow torques to Eq. (1) and repeating the linearization procedure from Sec. II C, we find that the AC spin accumulation renormalizes the pure spin-mixing conductance. Thus the addition of the backflow torque can be accounted for by replacing $g_\perp$ with $\tilde{g}_\perp$ in the boundary conditions of Eq. (12), making the boundary conditions Q-dependent in the process.

Using the values from Table I, which are based on typical values for a YIG-Pt bilayer system, we obtain $\tilde{g}_\perp/g_\perp \sim 0.4$ for $QL \ll 1$, whereas $\tilde{g}_\perp/g_\perp \to 1$ for large values of QL. Thus AC backflow is significant for long-wavelength modes and should be considered when estimating $g_\perp$ from the linewidth broadening in *ferromagnetic resonance* (FMR) experiments [11].

E. Inverse spin Hall effect

The *inverse spin Hall effect* (ISHE) converts a spin current in the NM to an electric potential through the spin-orbit coupling in the NM. For a spin current in the $\hat{\boldsymbol{\xi}}$ direction, the ISHE electric field in the NM layer is $\mathbf{E}_{\mathrm{ISHE}} = -e^{-1}\Theta\langle(\partial_\xi\boldsymbol{\mu}^{(\mathbf{s})})\times\hat{\boldsymbol{\xi}}\rangle_\xi$, where Θ is the dimensionless spin-Hall angle, and $\langle\cdot\rangle_\xi$ is a spatial average across the NM layer, i.e., for $\xi \in (L/2, L/2+d)$. Using the previously calculated spin accumulation, we find that the AC electric field is

$$\begin{aligned}\mathbf{E}_{\mathrm{ISHE}}^{\mathrm{AC}} = &-\Theta\frac{\hbar}{2deM_s}\left[1 + \frac{\sigma}{2g_\perp l_{\mathrm{sf,AC}}}\coth\left(\frac{d}{l_{\mathrm{sf,AC}}}\right)\right]^{-1}\\ &\times[-\hat{\boldsymbol{\eta}}(-m_{t,y}\cos\theta\cos\phi + m_{t,x}\sin\phi)\\ &+\hat{\boldsymbol{\xi}}(-m_{t,x}\cos\phi - m_{t,y}\cos\theta\sin\phi)],\end{aligned} \tag{24}$$

where

$$m_{t,i} = -[\mathrm{Im}\omega\mathrm{Re}m_i + \mathrm{Re}\omega\mathrm{Im}m_i]_{\xi=L/2}, \tag{25}$$

and $i = x,y$. For BVMSW ($\theta = \pi/2, \phi = 0$) modes, the AC field points along $\hat{\boldsymbol{\xi}}$, whereas for MSSW ($\theta = \phi = \pi/2$) modes, it points along $\hat{\boldsymbol{\eta}}$ (i.e., in plane, but transverse to ζ; see Fig. 1). Notice that for both BVMSW and MSSW mode geometries, only the x component of $\mathbf{m}_t$ contributes to the field. In contrast, for FVMSW ($\theta = 0$) modes, the field points somewhere in the $\eta\zeta$ plane, depending on the ratio of $m_{t,x}$ to $m_{t,y}$.

Similarly to the AC field, the DC ISHE electric field is given by

$$\mathbf{E}_{\mathrm{ISHE}}^{\mathrm{DC}} = \Theta\frac{\mu_{\mathrm{DC},0}^{(s)}}{de}\sin\theta(\hat{\boldsymbol{\eta}}\cos\phi - \hat{\boldsymbol{\xi}}\sin\phi), \tag{26}$$

which is perpendicular to the AC electric field and zero for the FVMSW mode geometry.

The total time-averaged energy in the ferromagnet $\mathcal{E}_{\mathrm{total}}$ (see, Morgenthaler [44]) is given by

$$\langle\mathcal{E}_{\mathrm{total}}\rangle_T = \int_{\mathrm{ferrite}}\mathrm{Re}\left[-i\pi\frac{\omega^*}{\omega_M}(\mathbf{m}\times\mathbf{m}^*)\hat{\mathbf{z}}\right]dV, \tag{27}$$

where the integral is taken over the volume of the ferromagnet.

Because the DC ISHE field is in-plane, the voltage measured per unit distance along the field direction, $\hat{\boldsymbol{\Lambda}} = \hat{\boldsymbol{\eta}}\cos\phi - \hat{\boldsymbol{\xi}}\sin\phi$, can be used to construct an estimate of the mode efficiency. Taking the one-period time average of Eq. (26) using Eq. (22) and normalizing it by Eq. (27) divided by the in-plane surface area, $\mathcal{A}$, we find an amplitude-independent measure of the DC ISHE:

$$\begin{aligned}\epsilon^{\mathrm{DC}} &= \frac{\langle e\hat{\boldsymbol{\Lambda}}\cdot\mathbf{E}_{\mathrm{ISHE}}^{\mathrm{DC}}\rangle_T}{\langle\mathcal{E}_{\mathrm{total}}\rangle_T/\mathcal{A}}\\ &= -2\gamma\Theta\frac{l_{\mathrm{sf}}\hbar}{d\sigma M_s}\tilde{g}_\perp\tanh\left(\frac{d}{l_{\mathrm{sf}}}\right)\sin\theta\\ &\quad\times\frac{\mathrm{Re}\left[-i\frac{\omega^*}{\omega_M}(\mathbf{m}\times\mathbf{m}^*)\hat{\mathbf{z}}\right]_{\xi=L/2}}{\int_{-L/2}^{L/2}\mathrm{Re}\left[-i\frac{\omega^*}{\omega_M}(\mathbf{m}\times\mathbf{m}^*)\hat{\mathbf{z}}\right]d\xi},\end{aligned} \tag{28}$$

given in units of cm, and where $\{\cdot\}^*$ denotes complex conjugation.

Similarly, the AC ISHE electric field, being time-varying, will contribute a power density that, when normalized by the power density in the ferromagnet, becomes

$$\epsilon^{\mathrm{AC}} = \frac{\left\langle \sigma \left(\mathbf{E}^{\mathrm{AC}}_{\mathrm{ISHE}}\right)^2 \right\rangle_T}{\frac{\mathrm{Re}\{\omega\}}{2\pi \mathcal{A}L}\langle \mathcal{E}_{\mathrm{total}}\rangle_T}$$
$$= \frac{\pi\sigma}{\mathrm{Re}\{\omega\}}\left(\frac{\Theta\hbar}{2deM_s}\right)^2\left[1 + \frac{\sigma}{2g_\perp l_{\mathrm{sf,AC}}}\coth\left(\frac{d}{l_{\mathrm{sf,AC}}}\right)\right]^{-2}$$
$$\times \frac{|m_{t,x}|^2 + \cos^2\theta |m_{t,y}|^2}{\frac{1}{L}\int_{-L/2}^{L/2} \mathrm{Re}\left[-i\frac{\omega^*}{\omega_M}(\mathbf{m}\times\mathbf{m}^*)\hat{\mathbf{z}}\right]d\xi}. \quad (29)$$

To be able to calculate explicit realizations of the mode-dependent equations (28) and (29), one will need to first calculate the dispersion relation and mode profiles in the ferromagnet.

III. SPIN-PUMPING THEORY FOR TRAVELLING SPIN WAVES

Because the linearized boundary conditions [see Eqs. (12)] explicitly depend on the eigenfrequency ω, we cannot apply the method of expansion in the set of pure exchange spin waves, as was performed by Kalinikos and Slavin [35]. Instead, we analyze and solve the system directly for small values of QL, whereas the dipole-dipole regime of $QL \sim 1$ is explored using numerical computations in Sec. IV.

A. Long-wavelength magnetostatic modes

When $QL \ll 1$, Eq. (11) is simplified to

$$\left\{\begin{pmatrix}\sin^2\theta & 0\\ 0 & 0\end{pmatrix} + i\frac{\omega}{\omega_M}\begin{pmatrix}\alpha & -1\\ 1 & \alpha\end{pmatrix}\right.$$
$$\left. + \mathbb{1}\left[\frac{\omega_H}{\omega_M} - 8\pi\frac{\gamma^2 A}{\omega_M^2}\frac{d^2}{d\xi^2}\right]\right\}\cdot \mathbf{m}_Q(\xi) = 0, \quad (30)$$

where the first-order matrix term describes the dipole-induced shape anisotropy and stems from $\widehat{\mathcal{G}}_{xy}$ (see Ref. [35]). We make the ansatz that the magnetization vector in Eq. (3) is composed of plane waves, e.g., $\mathbf{m}_Q(\xi) \propto e^{ik\xi}$. Inserting this ansatz into Eq. (30) produces the dispersion relation

$$\left(\frac{\omega}{\omega_M}\right)^2 = \left(\frac{\omega_H}{\omega_M} + \lambda_{\mathrm{ex}}^2 k^2 + i\alpha\frac{\omega}{\omega_M}\right)$$
$$\times\left(\frac{\omega_H}{\omega_M} + \lambda_{\mathrm{ex}}^2 k^2 + \sin^2\theta + i\alpha\frac{\omega}{\omega_M}\right), \quad (31)$$

where $\lambda_{\mathrm{ex}} \equiv \sqrt{8\pi\gamma^2 A/\omega_M^2}$ is the *exchange length*. Keeping only terms to first order in the small parameter α, we arrive at

$$\frac{\omega(k)}{\omega_M} = \pm\sqrt{\left(\frac{\omega_H}{\omega_M} + \lambda_{\mathrm{ex}}^2 k^2\right)\left(\frac{\omega_H}{\omega_M} + \lambda_{\mathrm{ex}}^2 k^2 + \sin^2\theta\right)}$$
$$+ i\alpha\left(\frac{\omega_H}{\omega_M} + \lambda_{\mathrm{ex}}^2 k^2 + \frac{\sin^2\theta}{2}\right). \quad (32)$$

The boundary conditions in Eq. (12) depend explicitly on ω and k and give another equation $k = k(\omega)$ to be solved simultaneously with Eq. (32). However, in the absence of spin pumping, i.e., when the spin-mixing conductance vanishes, $g_\perp \to 0$, it is sufficient to insert the constant k solutions from the boundary conditions into Eq. (32) to find the eigenfrequencies.

Different wave vectors can give the same eigenfrequency. It turns out that this is possible when $\omega(k) = \omega(i\kappa)$, which has a nontrivial solution relating κ to k:

$$\lambda_{\mathrm{ex}}^2\kappa^2 = \sin^2\theta + \lambda_{\mathrm{ex}}^2 k^2 + 2\frac{\omega_H}{\omega_M} \pm i2\alpha\omega(k)/\omega_M. \quad (33)$$

With these findings, a general form of the magnetization is

$$\mathbf{m}_Q(\xi) = \begin{pmatrix}1\\ r(k)\end{pmatrix}\left\{\left[C_1\cos\left[k\left(\xi + \frac{L}{2}\right)\right]\right.\right.$$
$$\left.\left. + C_2\sin\left[k\left(\xi+\frac{L}{2}\right)\right]\right]\right\} + \begin{pmatrix}1\\ r(i\kappa)\end{pmatrix}$$
$$\times\left\{C_3\cosh\left[\kappa\left(\xi + \frac{L}{2}\right)\right]\right.$$
$$\left. + C_4\sinh\left(\kappa\left(\xi+\frac{L}{2}\right)\right)\right]\Bigg\}, \quad (34)$$

where $\{C_i\}$ are complex coefficients to be determined from the boundary conditions, and where $\kappa = \kappa(k)$ is given by Eq. (33). The ratio between the transverse components of the magnetization, $r(k) = Y_Q/X_Q$, is determined from the bulk equation of motion [see Eq. (30)] and is in linearized form,

$$r(k) = -\frac{\alpha\sin^2\theta \pm 2i\sqrt{\left(\frac{\omega_H}{\omega_M} + \lambda_{\mathrm{ex}}^2 k^2\right)\left(\frac{\omega_H}{\omega_M} + \lambda_{\mathrm{ex}}^2 k^2 + \sin^2\theta\right)}}{2\left(\frac{\omega_H}{\omega_M} + \lambda_{\mathrm{ex}}^2 k^2\right)}, \quad (35)$$

implying elliptical polarization of $\mathbf{m}_Q$ when $\theta \neq 0$.

Inserting Eq. (34) into Eq. (8) only leads to a solution when $k = 0$, such that $C_2 = C_4 = 0$ in the general case. By solving Eq. (12b) for C_3, we find

$$\frac{C_3}{C_1} = -\frac{\frac{\omega_H}{\omega_M} + \lambda_{\mathrm{ex}}^2 k^2 + \sin^2\theta + i\alpha\frac{\omega}{\omega_M}}{\frac{\omega_H}{\omega_M} - \lambda_{\mathrm{ex}}^2\kappa^2 + \sin^2\theta + i\alpha\frac{\omega}{\omega_M}}$$
$$\times\frac{\left(i\frac{\omega}{\omega_M}\tilde{\rho} + d\cos^2\theta\right)\cos(kL) - kL\sin(kL)}{\left(i\frac{\omega}{\omega_M}\tilde{\rho} + d\cos^2\theta\right)\cosh(\kappa L) + \kappa L\sinh(\kappa L)}, \quad (36)$$

where $\tilde{\rho} \equiv \rho|_{g_\perp \to \tilde{g}_\perp}$ is the pumping parameter altered by the AC spin backflow from the NM (see Sec. II D). C_1 is chosen to be the free parameter that parameterizes the dynamic magnetization amplitude, which can be determined given a particular excitation scheme. The linearization of Eq. (36) with respect to α is straightforward, but the expression is lengthy; we will therefore not show it here.

Inserting the ansatz with $C_2 = C_4 = 0$ and C_3 given by Eq. (36) into Eq. (12a) gives the second equation for k and ω [the first is Eq. (32)]. In the general case, the number of terms in this equation is very large; thus we describe it as

$$f(k,\omega,\alpha,\tilde{\rho}) = 0, \quad (37)$$

i.e., an equation that depends on the wave vector k, frequency ω, Gilbert damping constant α, and the spin-pumping parameter $\tilde{\rho}$.

Because both the bulk and interface-induced dissipation are weak, $\alpha \ll 1, \tilde{\rho} \ll 1$, the wave vector is only slightly perturbed with respect to a system without dissipation, i.e., $k \to k + \delta k$ where $\lambda_{\mathrm{ex}}\delta k \ll 1$. It is therefore sufficient to expand f up to first order in these small quantities:

$$f(k,\omega,0,0) + (\tilde{\rho})\frac{\partial f}{\partial \tilde{\rho}}\bigg|_0 + \alpha \frac{\partial f}{\partial \alpha}\bigg|_0 + (\lambda_{\mathrm{ex}}\delta k)\frac{\partial f}{\partial(\lambda_{\mathrm{ex}}\delta k)}\bigg|_0 \approx 0, \tag{38}$$

where the sub-index 0 means evaluation in a system without dissipation, i.e., when $(\alpha,\tilde{\rho},\delta k) = (0,0,0)$. By solving the system of equations in the absence of dissipation, $f(k,\omega,0,0) = 0$, the dissipation-induced change in the wave vector δk is given by

$$\delta k \approx -\frac{\tilde{\rho}\frac{\partial f}{\partial \tilde{\rho}}\big|_0 + \alpha \frac{\partial f}{\partial \alpha}\big|_0}{\lambda_{\mathrm{ex}}\frac{\partial f}{\partial(\lambda_{\mathrm{ex}}\delta k)}\big|_0}. \tag{39}$$

In turn, this change in the wave vector should be inserted into the dispersion relation of Eq. (31) to find the dissipation. Inspecting Eq. (31), we note that δk-induced additional terms proportional to ω are of the form $(k+\delta k)^2 - k^2 \approx 2k\delta k$, which renormalize the Gilbert-damping term $i\alpha\frac{\omega}{\omega_M}$. Thus, in Eq. (39), there are terms proportional to the frequency in both terms in the numerator. We extract these terms $\propto i\frac{\omega}{\omega_M}$ by differentiating with respect to ω and define the renormalization of the Gilbert damping, i.e., $\alpha \to \alpha + \Delta\alpha$, from spin pumping as

$$\Delta\alpha = \frac{i2\lambda_{\mathrm{ex}}k\omega_M\partial_\omega(\lambda_{\mathrm{ex}}\delta k|_{\alpha=0})}{i2\lambda_{\mathrm{ex}}k\omega_M\partial_\omega(\lambda_{\mathrm{ex}}\delta k|_{\tilde{\rho}=0}) - 1}, \tag{40}$$

where ∂_ω represents the derivative with respect to ω and k is the solution to the zeroth-order equation. Note that in performing a further local analysis around some point k_0 in the k space of Eq. (37), a series expansion of f around k_0 must be performed before evaluating Eqs. (39) and (40).

Equation (40) is generally valid, except when $d = 0$ and $kL \to 0$, which we discuss below. In the following section, we will determine explicit solutions of the zeroth-order equation for some key cases, and map out the spin-wave dispersion relations and dissipation in the process.

B. No surface anisotropy ($d = 0$)

Let us first investigate the case of a vanishing surface anisotropy. In this case, the zeroth-order expansion of Eq. (37) has a simple form and is independent of the magnetization angle θ. The equation to determine k is given by

$$kL\tan(kL) = 0, \tag{41}$$

with solutions $k = n\pi/L$, where $n \in \mathbb{Z}$. Similarly, the expression for δk is greatly simplified, $\delta k_n = i\frac{\omega}{\omega_M}\frac{\tilde{\rho}}{n\pi}\frac{\lambda_{\mathrm{ex}}}{L}$, $n \neq 0$, such that the mode-dependent Gilbert damping is

$$\Delta\alpha_n = 2\tilde{\rho}\left(\frac{\lambda_{\mathrm{ex}}}{L}\right)^2, \quad n \neq 0. \tag{42}$$

For the macrospin mode, when $n = 0$, the linear expansion in δk becomes insufficient. This is because $kL\tan(kL) \sim (kL)^2$ for $kL \to 0$; thus we must expand the function f to second order in the deviation δk around $kL = 0$. For $d = 0$, we find that the boundary condition becomes $\delta k^2 L^2 = i\frac{\omega}{\omega_M}\tilde{\rho}\lambda_{\mathrm{ex}}^2$, and when inserted into Eq. (31), it immediately gives

$$\Delta\alpha_0 = \tilde{\rho}\left(\frac{\lambda_{\mathrm{ex}}}{L}\right)^2 = \frac{1}{2}\Delta\alpha_n, \tag{43}$$

which is the macrospin renormalization factor found in Ref. [15]. Using a different approach, our results in this section reproduce our previous result that the renormalization of the Gilbert damping for standing waves is twice the renormalization of the Gilbert damping of the macrospin [18]. Next, we will obtain analytical results beyond the description in Ref. [18] for the enhancement of the Gilbert damping in the presence of surface anisotropy.

C. Including surface anisotropy ($d \neq 0$)

In the presence of surface anisotropy, the out-of-plane and in-plane field configurations must be treated separately. This distinction is because the boundary condition (37) has different forms for the two configurations in this scenario.

1. Out-of-plane magnetization

When the magnetization is out of plane, i.e., $\theta = 0$, the spin-wave excitations are circular and have a high degree of symmetry. A simplification in this geometry is that the coefficient $C_3 = 0$. In the absence of dissipation, the boundary condition (37) determining the wave vectors becomes

$$kL\tan(kL) = d. \tag{44}$$

Let us consider the effects of the two different anisotropies in this geometry.

a. Easy-axis surface anisotropy ($d > 0$). When $d \sim 1$ or larger, the solutions of Eq. (44) are displaced from the zeros of $\tan(kL)$, i.e., the solutions we found in the case of no surface anisotropy, and towards the upper poles located at $k_uL = (2n+1)\pi/2$, where $n = 0,1,2,\ldots$. We therefore expand f in Eq. (37) [and thus also in Eq. (44)] into a Laurent series around the poles from the first negative order up to the first positive order in kL to solve the boundary condition for kL, giving

$$kL \approx \frac{\lambda_{\mathrm{ex}}}{L}\frac{3(1+d) + 2(k_uL)^2 - \sqrt{12(k_uL)^2 + 9(1+d)^2}}{2k_uL}. \tag{45}$$

Using this result and the Laurent-series expansion for f in Eqs. (39) and (40), we find the Gilbert-damping renormalization term ($\alpha \to \alpha + \Delta\alpha^{(\mathrm{oop})}_{\mathrm{EA,n}}$) and the ratio between the modes

$$\frac{\Delta\alpha^{(\mathrm{oop})}_{\mathrm{EA,n}}}{\Delta\alpha_0} \approx 3\left(3(1+d) + 2(k_uL)^2 - \sqrt{12(k_uL)^2 + 9(1+d)^2}\right) \times \frac{\left(\sqrt{4(k_uL)^2 + 3(1+d)^2} - \sqrt{3}(1+d)\right)}{2(k_uL)^2\sqrt{4(k_uL)^2 + 3(1+d)^2}}. \tag{46}$$

This ratio is plotted in Fig. 3 for $n \leqslant 5$. We see that the ratio vanishes for large values of d. For small values of the

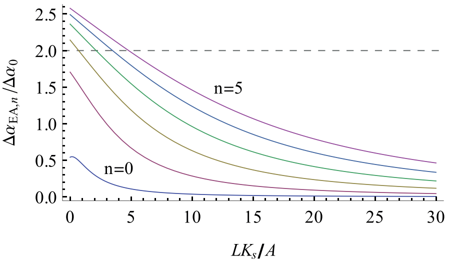

FIG. 3. The ratio of enhanced Gilbert damping $\Delta\alpha_{\mathrm{EA,n}}/\Delta\alpha_0$ in a system with easy-axis surface anisotropy vs the enhanced Gilbert damping of macrospin modes in systems with no surface anisotropy as a function of surface-anisotropy energy. n refers to the mode number, where $n = 0$ is the uniformlike mode. The dashed line represents the ratio $\Delta\alpha_n/\Delta\alpha_0$ in the case of no surface anisotropy [see Eq. (42)].

anisotropy energy d, the approximate ratio exceeds the exact result of the ratio we found in the limiting case of no surface anisotropy [see Eq. (42)]. For moderate values of $d \sim 5$, the expansion around the upper poles is sufficient, but only for the first few modes. This implies that moderate-strength easy-axis surface anisotropy quenches spin pumping for the lowest excited modes but does not affect modes with higher transverse exchange energy.

b. Easy-plane surface anisotropy ($d < 0$). Easy-plane surface anisotropy is represented by a negative surface anisotropy d in Eq. (44). In this case, the boundary condition must be treated separately for the uniformlike ($n = 0$) mode and the higher excitations. When $|d| > 1$, we can obtain a solution by expanding along the imaginary axis of kL. This corresponds to expressing the boundary condition in the form $-ikL\tanh(ikL) = -|d|$, with the asymptotic behavior $kL \approx -i|d|$. Using the asymptotic form of the boundary condition in Eq. (39) and calculating the renormalization of the Gilbert damping using Eq. (40), we find that the renormalization is $\alpha \to \alpha + \Delta\alpha^{(\mathrm{oop})}_{\mathrm{EP,0}}$, where

$$\frac{\Delta\alpha^{(\mathrm{oop})}_{\mathrm{EP,0}}}{\Delta\alpha_0} = 2|d|. \tag{47}$$

Thus the Gilbert damping of the lowest mode is much enhanced by increasing the surface anisotropy. The surface-anisotropy mode is localized at the surface because it decays from the spin-active interface and into the film. Because the effective volume of the mode is reduced, spin pumping more strongly causes dissipation out of the mode and into the normal metal.

For the higher modes ($n > 0$), the negative term on the rhs of Eq. (44) forces the kL solutions closer to the negative, lower poles of $\tan(kL)$, located at $k_n^{(l)}L = (2n-1)\pi/2$, where $n = 1, 2, 3, \ldots$. We repeat the procedure used for the EA case by expanding f into a Laurent series around these lower poles,

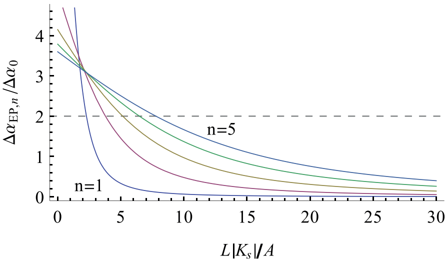

FIG. 4. Plot of $\Delta\alpha^{(\mathrm{oop})}_{\mathrm{EP,n}}/\Delta\alpha_0$. The dashed line represents the ratio $\Delta\alpha_n/\Delta\alpha_0$ in the case of no surface anisotropy [see Eq. (42)].

arriving at

$$kL \approx \frac{3(1-|d|) + 2\left(k_n^{(l)}L\right)^2 + \sqrt{12\left(k_n^{(l)}L\right)^2 + 9(1-|d|)^2}}{2k_n^{(l)}L}. \tag{48}$$

Using this relation and the new lower-pole Laurent expansion for f, Eqs. (39) and (40) give us the renormalization of the Gilbert damping ($\alpha \to \alpha + \Delta\alpha^{(\mathrm{oop})}_{\mathrm{EP,n}}$) and the ratio

$$\begin{aligned}\frac{\Delta\alpha^{(\mathrm{oop})}_{\mathrm{EP,n}}}{\Delta\alpha_0} \approx\, & 3(3(1-|d|) + 2(k_uL)^2 \\ & + \sqrt{12(k_uL)^2 + 9(1-|d|)^2}) \\ & \times \frac{(\sqrt{4(k_uL)^2 + 3(1-|d|)^2} + \sqrt{3}(1-|d|))}{2(k_uL)^2\sqrt{4(k_uL)^2 + 3(1-|d|)^2}}.\end{aligned} \tag{49}$$

This ratio is plotted in Fig. 4 from $n = 1$ up to $n = 5$. We see that the ratio vanishes for large values of $|d|$. Similar to the case of EA surface anisotropy, the approximation breaks down for large n and/or small values of $|d|$.

Whereas the $n = 0$ mode exhibits a strong spin-pumping enhanced dissipation in this field configuration, the DC ISHE field vanishes when $\theta = 0$ [see Eq. (26)]. This is one of the reasons why this configuration is seldom used in experiments. However, this configuration can lead to a significant AC ISHE, and a similar AC signal was recently detected [12]. Because of the strong dissipation enhancement, the EP surface anisotropy induced localized mode in perpendicular magnetization geometry could be important in future experimental work.

2. *In-plane magnetization*

We will now complete the discussion of the spin-pumping enhanced Gilbert damping by treating the case in which the magnetization is in plane ($\theta = \pi/2$). For such systems, the coefficient $C_3 \neq 0$, and the zeroth-order expansion of Eq. (37) becomes

$$kL\tan kL = -\frac{d\left((\lambda_{\mathrm{ex}}k)^2 + \frac{\omega_H}{\omega_M}\right)\sqrt{1 + (\lambda_{\mathrm{ex}}k)^2 + 2\frac{\omega_H}{\omega_M}}}{\sqrt{1 + (\lambda_{\mathrm{ex}}k)^2 + 2\frac{\omega_H}{\omega_M}}\left(1 + 2(\lambda_{\mathrm{ex}}k)^2 + 2\frac{\omega_H}{\omega_M}\right) - d\frac{\lambda_{\mathrm{ex}}}{L}\left(1 + (\lambda_{\mathrm{ex}}k)^2 + \frac{\omega_H}{\omega_M}\right)\coth\left(\frac{L}{\lambda_{\mathrm{ex}}}\sqrt{1 + (\lambda_{\mathrm{ex}}k)^2 + 2\frac{\omega_H}{\omega_M}}\right)}. \tag{50}$$

For typical film thicknesses, of some hundred nanometers, we have $L/\lambda_{\rm ex} \gg 1$ and $(\lambda_{\rm ex}k)^2 \ll 1$ for the lowest eigenmodes. Thus we take the asymptotic coth ~ 1 and neglect the $(\lambda_{\rm ex}k)^2$ terms, ridding the rhs of Eq. (50) of any k dependence. Equation (50) now becomes similar to the out-of-plane case,

$$kL\tan(kL) = d_{\rm eff}, \tag{51}$$

where

$$d_{\rm eff} = -\frac{d\frac{\omega_H}{\omega_M}\sqrt{1+2\frac{\omega_H}{\omega_M}}}{\left(1+2\frac{\omega_H}{\omega_M}\right)^{3/2} - d\frac{\lambda_{\rm ex}}{L}\left(1+\frac{\omega_H}{\omega_M}\right)}. \tag{52}$$

$d_{\rm eff}$ is positive if $d<0$ and negative for $d>0$ up to a critical value $d\lambda_{\rm ex}/L = \lambda_{\rm ex}K_s/A = (1+2\frac{\omega_H}{\omega_M})^{3/2}/(1+\frac{\omega_H}{\omega_M})$, where the denominator becomes zero. For negative d, $|d_{\rm eff}| < |d|$, whereas for positive d, $|d_{\rm eff}|$ is initially smaller than that of $|d|$ but quickly approaches the critical value. With the value K_s from Table I, we have $|d_{\rm eff}| < |d|$, independent of the sign of d.

With this relation, we can calculate an approximate Gilbert damping renormalization in both the EA and EP cases using the EP and EA relations, respectively, obtained in the out-of-plane configuration. Thus

$$\Delta\alpha^{\rm ip}_{\rm EA,0} \approx \Delta\alpha^{\rm oop}_{\rm EP,0}|_{d\to d_{\rm eff}} = 2|d_{\rm eff}|, \tag{53}$$

$$\Delta\alpha^{\rm ip}_{\rm EA,n} \approx \Delta\alpha^{\rm oop}_{\rm EP,n}|_{d\to d_{\rm eff}}, \tag{54}$$

$$\Delta\alpha^{\rm ip}_{\rm EP,n} \approx \Delta\alpha^{\rm oop}_{\rm EA,n}|_{d\to d_{\rm eff}}. \tag{55}$$

To summarize this section regarding the enhancement of Gilbert damping, we see that the enhancement can be very strong for the surface modes because their effective sizes are smaller than the thickness of the film. For all other modes, the enhancement decreases with increasing magnitude of the surface-anisotropy energy.

IV. NUMERICAL CALCULATIONS

The first step in the numerical method is to approximate the equation of motion of Eq. (11) into by finite-size matrix eigenvalue problem. We discretize the transverse coordinate ξ on the interval $[-L/2,L/2]$ into N points labeled by $j = 1, 2, \ldots, N$, and characterize the transverse discrete solutions of the dynamic magnetization vectors $\mathbf{m}_Q$ by $(m_{x,j},m_{y,j})$ of size $2N$.

We approximate the second-order derivative arising from the exchange interaction using a nth-order central difference method. For the $n-2$ discretized points next to the boundaries, we also use nth-order methods, using forward (backward) difference schemes for the lower (upper) film boundary. This strategy avoids the introduction of "ghost" points outside the interval $[-L/2,L/2]$ to satisfy the boundary conditions.

Thus the total operator acting on the magnetization on the left-hand side of Eq. (11) becomes a sparse $2N \times 2N$ matrix operator. On the right-hand side of Eq. (11), we also represent the convolution integral as a $2N \times 2N$ dense matrix operator, where each row is weighted according to the extended integration formulas for closed integrals to nth order [45]. The four $N \times N$ subblocks of this integration operator correspond to the four tensor elements of $\widehat{\mathcal{G}}_{xy}$. In the final discrete form, we obtained a $2N \times 2N$ ω-dependent matrix.

Next, the four boundary conditions (at the left and right boundaries for the two components, m_x and m_y) are used to reduce the number of equations to $2N-4$. This is performed by algebraically solving the discretized boundary conditions with respect to the boundary points, i.e., by determining m_i where $i \in \{1,N,N+1,2N\}$ in terms of the magnetizations at the interior points.

Finally, each $(2N-4)\times(2N-4)$ matrix is separated into two parts: a term independent of the frequency ω and a term proportional to ω. The dipole interaction causes the eigenvalue problem to be non-Hermitian and therefore computationally more demanding than a generalized eigenvalue problem. We find the dispersion relation and magnetization vectors by solving this eigenvalue problem. The resulting eigenvectors are used to find the magnetization at the boundary by back-substitution into the equations for the boundary conditions.

We are interested in finding the mode and wave-vector dependence of the spin-pumping enhanced Gilbert damping. To obtain this information numerically, we perform two independent calculations of the (complex) eigenvalues. First, we calculate the complex eigenvalues $\omega_{\rm d}$ when there is no spin pumping, but dissipation occurs via the conventional bulk Gilbert damping. Second, we calculate the complex eigenvalues $\omega_{\rm sp}$ when spin pumping is active at the FI-NM interface but there is no bulk Gilbert damping. A mode- and wave-vector-dependent measure of the effective enhanced Gilbert damping enhancement is then given by

$$\Delta\alpha = \alpha\frac{{\rm Im}\omega_{\rm sp}}{{\rm Im}\omega_{\rm d}}. \tag{56}$$

To ensure that we treat the same modes in the two independent calculations, we check the convergence of the relative difference in the real part of the eigenvalues. Table I lists the values for the different system parameters that are used throughout this section.

Let us first discuss the renormalization of the Gilbert damping when there is no surface anisotropy. We will present the numerical results for the three main geometries described in Sec. I and compare the results to the analytical results of Sec. III A.

A. FVMSW ($\theta = 0$)

Figure 5 shows the wave-vector dependent renormalization of the Gilbert damping $\Delta\alpha$ due to spin pumping at the FI-NM interface in the FVMSW geometry. In this geometry, waves traveling along $\pm\hat{\zeta}$ have the same symmetry; thus each line is doubly degenerate and corresponds to two waves of $\pm\omega$. The "spikes" in the figure are due to degeneracies, i.e., mode crossings, and upon inspection, these spikes can be observed in the dispersion relation.

1. Easy-axis surface anisotropy ($\hat{\xi}$ easy axis)

Figure 6 shows $\Delta\alpha_{\rm EA}$ for the FVMSW geometry with an EA surface anisotropy at the spin-active interface. As predicted in Sec. III C 1a, all modes exhibit a decreased $\Delta\alpha$ compared with those in Eqs. (43) and (42). For small QL and the chosen value of K_s (see Table I), the first four modes match the

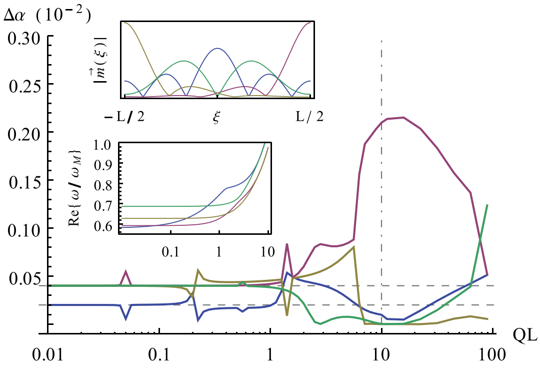

FIG. 5. $\Delta\alpha$ vs wave vector for the FVMSW geometry of the four smallest eigenvalues. (Top inset) Magnitudes of eigenvectors (in arbitrary units) across the film at $QL = 10$. (Bottom inset) Dispersion relation in the dipole-dipole active regime.

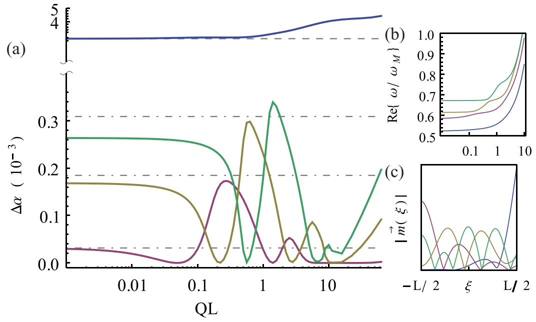

FIG. 7. (a) $\Delta\alpha_{\mathrm{EP}}$ vs wave vector for the FVMSW geometry, showing the four smallest eigenvalues. The dashed lines represent the analytic solutions from Sec. III C 1b. (b) Dispersion relation in the dipole-dipole active regime. (c) Magnitude of eigenvectors (in arbitrary units) across the film at $QL = 5$.

analytical result of Eq. (46), which is consistent with the plot in Fig. 3. For even higher excited modes, the effect of the EA surface anisotropy becomes weaker due to the increase in transverse exchange energy. These modes (not shown in the figure) approach the value of $\Delta\alpha_n$.

2. *Easy-plane surface anisotropy ($\hat{\xi}$ hard axis)*

Figure 7 shows $\Delta\alpha_{\mathrm{EP}}$ for the FVMSW geometry with an EP surface anisotropy. We see that the mode corresponding to $n = 0$ has been promoted to a surface mode with a large $\Delta\alpha$, which for small values of QL matches Eq. (47). For the higher excited modes, we observe a decrease in $\Delta\alpha$ compared to the case with no surface anisotropy.

B. BVMSW ($\theta = \pi/2$ and $\phi = 0$)

Figure 8 shows the QL-dependent renormalization of the Gilbert damping due to spin pumping at the FI-NM interface in the BVMSW geometry. We see that the enhancement $\Delta\alpha$ agrees with the analytic limits in Eqs. (43) and (42) for small values of QL. For large values of QL, we are in the strong exchange regime, in which the in-plane exchange energy becomes large compared to all other energy contributions. This in-plane exchange stiffness effectively quenches the coupling to the normal metal layer, causing $\Delta\alpha \to 0$ for large values of QL.

Although Fig. 8 only appears to show the three first eigenvalues and eigenvectors, it actually contains double this amount. Because $\hat{\mathbf{z}}$ is parallel to the wave-propagation direction $\hat{\zeta}$ in this geometry, there is no change in dipolar energies, regardless of whether the wave travels in the $+\hat{\zeta}$ direction or in the $-\hat{\zeta}$ direction; thus, the Gilbert damping is enhanced equally in both wave directions. A slight offset from this configuration, taking either $\theta < \pi/2$ or $\phi \neq 0$, would result in a splitting of each line in Fig. 8 into two distinct lines.

Including surface anisotropy

Figure 9 shows both the EA and the EP surface-anisotropy calculations in the BVMSW geometry. In the case of an EA

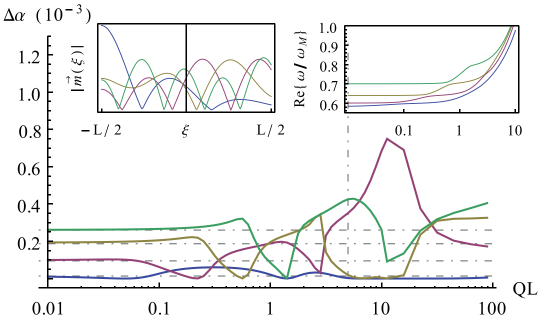

FIG. 6. $\Delta\alpha_{\mathrm{EA}}$ vs wave vector for the FVMSW geometry showing the four smallest eigenvalues. The horizontal dashed lines indicate solutions of Eq. (46). (Left inset) Magnitudes of eigenvectors (in arbitrary units) across the film at $QL = 5$. (Right inset) Dispersion relation in the dipole-dipole active regime.

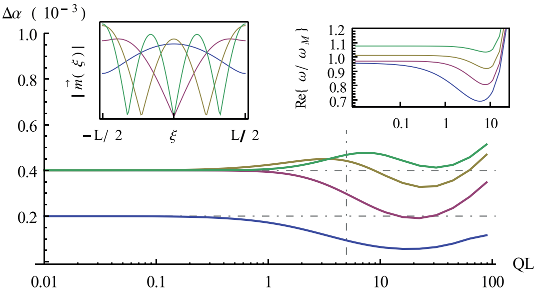

FIG. 8. $\Delta\alpha$ vs wave vector for the BVMSW geometry ($\theta = \pi/2$ and $\phi = 0$) with $K_s = 0$, plotted for the four smallest eigenvalues. (Left inset) Magnitudes of normalized eigenvectors across the film at $QL = 5$. (Right inset) Dispersion relation in the dipole-dipole active regime.

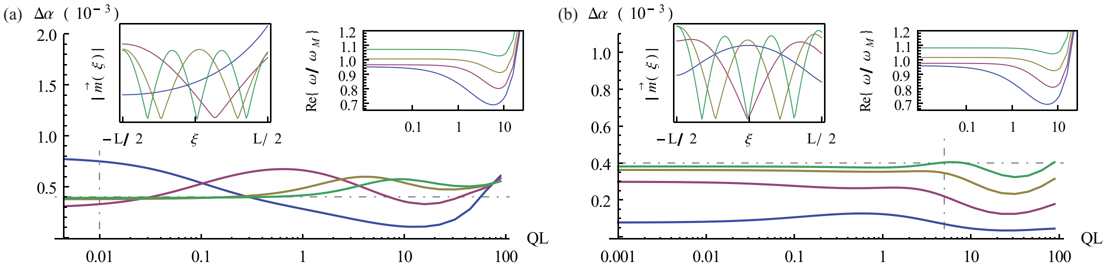

FIG. 9. (a) Dispersion relation vs wave vector for the BVMSW geometry ($\theta = \pi/2$, $\phi = 0$) for the four lowest eigenvalues in the case of EA surface anisotropy. (b) Dispersion relation in the case of EP surface anisotropy. In both figures, the horizontal dashed lines mark the value of $\Delta\alpha_n$ in the case of no surface anisotropy.

surface anisotropy, the mode corresponding to $n = 0$ gets promoted to a surface mode, similarly to the case in which there is EP surface anisotropy in the FVMSW geometry. The increase in $\Delta\alpha$ is much smaller for the same magnitude of K_s, as explained in detail in Sec. III C. The higher modes, corresponding to $n > 0$, exhibit increased quenching of the Gilbert damping enhancement. In the case of EP surface anisotropy, all modes exhibit quenched Gilbert damping enhancement.

C. MSSW ($\theta = \phi = \pi/2$)

Figure 10 shows the QL-dependent renormalization of the Gilbert damping due to spin pumping at the FI-NM interface in the MSSW geometry. The computed eigenvalues agree with Eqs. (43) and (42) for small values of QL. We see in the inset of Fig. 10 that in this geometry, the macrospinlike mode behaves as predicted by Damon and Eshbach [36], Eshbach and Damon [37], cutting through the dispersion relations of the higher excited modes for increasing values of QL in the dipole-dipole regime. A prominent feature of this geometry is the manner in which the modes with different signs of Re{ω} behave differently due to the dipole-dipole interaction. This is because the internal field direction ($\hat{\mathbf{z}}$) is not parallel to the direction of travel ($\hat{\boldsymbol{\zeta}}$) of the spin wave. Hence, changing the sign of ω is equivalent to inverting the externally applied field, changing the xyz coordinate system in Fig. 1 from a right-handed coordinate system to a left-handed system. In the middle of the dipole regime, the lack of symmetry with respect to propagation direction has different effects on the eigenvectors; e.g., in the dipole-dipole active region the modes with positive or negative Re{ω} experience an increased or decreased magnitude of the dynamic magnetization, depending on the value of QL, as shown in Figs. 10(e) and 10(f). This magnitude difference creates different renormalizations of the Gilbert damping, as the plot of $\Delta\alpha^{(\pm)}$ in Figs. 10(b) and 10(c) shows.

Including surface anisotropy

Figure 11 shows $\Delta\alpha$ computed for modes in the MSSW geometry with EA and EP surface anisotropies. We can clearly see that for small QL an exponentially localized mode exists in the EA case, and as predicted in Sec. III C, all the lowest-energy modes have spin pumping quenched by EP surface

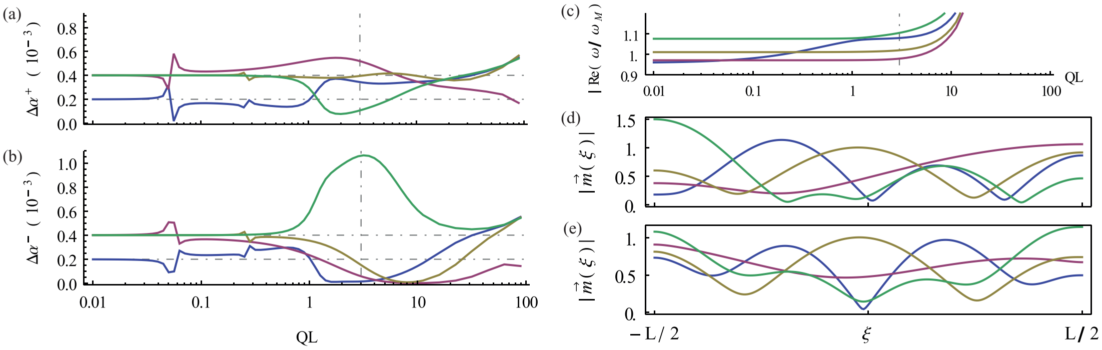

FIG. 10. Gilbert damping renormalization in the MSSW geometry. Subplots (a) and (b) show Gilbert damping renormalization $\Delta\alpha$ for modes with positive (negative) Re{ω}. The horizontal dashed lines represent the analytical values $\Delta\alpha_0$ and $\Delta\alpha_n$ for small QL. (c) Dispersion relation vs wave vector for the MSSW geometry ($\theta = \phi = \pi/2$) for the four smallest eigenvalues, colored pairwise in $\pm\omega$. Subplot (d) [(e)] shows the magnitude of normalized eigenvectors (in arbitrary units) at $QL = 3$ across the film modes with positive [(negative)] Re{ω}.

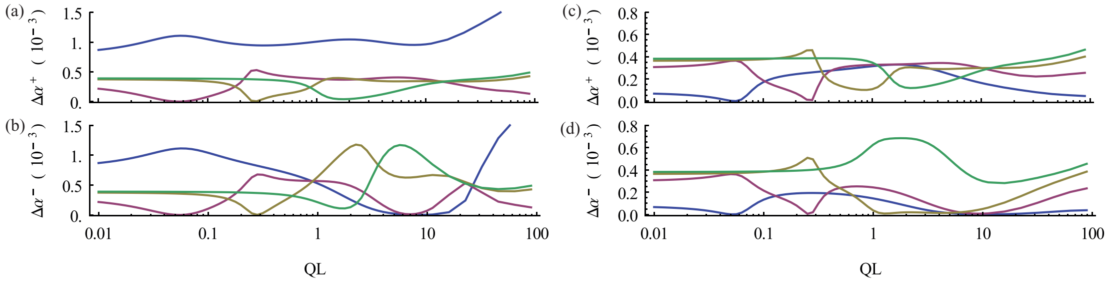

FIG. 11. (a) and (b) Gilbert damping renormalization from spin pumping in the MSSW geometry ($\theta = \phi = \pi/2$) for modes with positive (negative) Re$\{\omega\}$ in the case of EA surface anisotropy. The four smallest eigenvalues are colored pairwise in $\pm\omega$ across the plots. (c) and (d) show the Gilbert damping renormalization in the case of EP surface anisotropy.

anisotropy. This is similar to the corresponding case in the BVMSW geometry.

D. AC and DC ISHE

Figure 12 shows the DC and AC ISHE measures for the BVMSW geometry corresponding to the data represented in Fig. 8. In this geometry, the angular term, $\sin\theta$, in Eq. (28) is to equal one, ensuring that the DC measure is nonzero. This is not the case for all geometries because the DC electric field vanishes in the FVMSW geometry. The mode-dependent DC ISHE measure exhibits the same QL-dependence as the spectrum of the Gilbert damping enhancement in all geometries where $\sin\theta \neq 0$. We have already presented the renormalization of the Gilbert damping in the most general cases above. Therefore we restrict ourselves to presenting the simple case of the BVMSW geometry with no surface anisotropy here.

The AC ISHE measure plotted in Fig. 12 exhibits a similar QL dependence to the Gilbert damping renormalization (and hence the DC ISHE measure), but with a slight variation in the spectrum towards higher values of QL. Note that because Eq. (24) is nonzero for all values of θ, the AC effect should be detectable in the FVMSW geometry. By comparing the computed renormalization of the Gilbert damping for the different geometries in the previous subsections, we see that the strong renormalization of the $n = 0$ induced surface mode that occurs in the FVMSW geometry with easy-plane surface anisotropy (see Sec. IV A2 and Fig. 7) can have a proportionally strong AC ISHE signal in the normal metal.

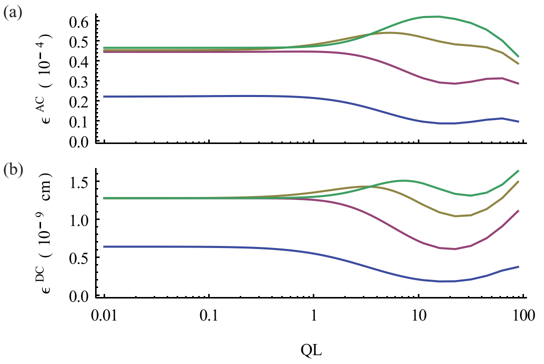

FIG. 12. ISHE as a function of in-plane wave vector in the BVMSW geometry with $K_s = 0$. (a) AC ISHE measure of Eq. (28) and (b) DC ISHE measure of Eq. (28).

V. CONCLUSION

In conclusion, we have presented analytical and numerical results for the spin-pumping-induced Gilbert damping and direct- and alternating terms of the inverse spin-Hall effect. In addition to the measures of the magnitudes of the DC and AC ISHE, the effective Gilbert damping constants strongly depend on the modes through the wave numbers of the excited eigenvectors.

In the long-wavelength limit with no substantial surface anisotropy, the spectrum is comprised of standing-wave volume modes and a uniformlike (macrospin) mode. These results are consistent with our previous findings [18]: in the long-wavelength limit, the ratio between the enhanced Gilbert damping for the higher volume modes and that of the macrospin mode is equal to two. When there is significant surface anisotropy, the uniform mode can be altered to become a pure localized surface mode (in the out-of-plane geometry and with EP surface anisotropy), a blend between a uniform mode and a localized mode (in-plane geometries and EA surface anisotropy), or quenched uniform modes (out-of-plane field configuration and EA surface anisotropy, or in-plane field configuration and EP surface anisotropy). The effective Gilbert damping is strongly enhanced for the surface modes but decreases with increasing surface-anisotropy energies for all the other modes.

The presented measures for both the AC and DC inverse spin-Hall effects are strongly correlated with the spin-pumping renormalization of the Gilbert damping, with the DC effect exhibiting the same QL dependency, whereas the AC effect exhibits a slighthly different variation for higher values of QL. Because the AC effect is nonzero in both in-plane and out-of-plane geometries and because both EP and EA surface anisotropies induce surface-localized waves at the spin-active interface, the AC ISHE can be potentially large for these modes.

ACKNOWLEDGMENTS

We acknowledge support from EU-FET Grant No. 612759 (“InSpin”), ERC AdG Grant No. 669442 (“Insulatronics”), and the Research Council of Norway Grant No. 239926.

APPENDIX: COORDINATE TRANSFORMS

The transformation for vectors from $\xi\eta\zeta$ to xyz coordinates (see Fig. 1) is given by an affine transformation matrix T, so that

$$\mathbf{f}_{(xyz)} = \mathbf{T}\cdot\mathbf{f}_{(\xi\eta\zeta)},$$

for some arbitrary vector $\mathbf{f}$. Tensor-vector products are transformed by inserting a unity tensor $\mathbf{I} = \mathbf{T}^{-1}\mathbf{T}$ between the tensor and vector and by left multiplication by the tensor $\mathbf{T}$, such that the tensor transforms as $\mathbf{T}\widehat{\mathcal{G}}\mathbf{T}^{-1}$ for some tensor $\widehat{\mathcal{G}}$ written in the $\xi\eta\zeta$ basis.

$\mathbf{T}$ is given by the concatenated rotation matrices $\mathbf{T} = \mathbf{R}_2\cdot\mathbf{R}_1$, where R_1 is a rotation ϕ around the ξ axis, and R_2 is a rotation $\theta - \frac{\pi}{2}$ around the new η axis/y axis. Hence

$$\mathbf{R}_1 = \begin{pmatrix} 1 & 0 & 0 \\ 0 & \cos\phi & -\sin\phi \\ 0 & \sin\phi & \cos\phi \end{pmatrix}, \tag{A1}$$

$$\mathbf{R}_2 = \begin{pmatrix} \sin\theta & 0 & -\cos\theta \\ 0 & 1 & 0 \\ \cos\theta & 0 & \sin\theta \end{pmatrix}, \tag{A2}$$

such that

$$\mathbf{T} = \begin{pmatrix} \sin\theta & -\cos\theta\sin\phi & -\cos\theta\cos\phi \\ 0 & \cos\phi & -\sin\phi \\ \cos\theta & \sin\theta\sin\phi & \sin\theta\cos\phi \end{pmatrix}. \tag{A3}$$

This transformation matrix consists of orthogonal transformations; thus the inverse transformation, which transforms $xyz \to \xi\eta\zeta$, is just the transpose, $\mathbf{T}^{-1} = \mathbf{T}^{T}$.

---

[1] A. Serga, A. Chumak, and B. Hillebrands, J. Phys. D **43**, 264002 (2010).

[2] V. Cherepanov, I. Kolokolov, and V. L’vov, Phys. Rep. **229**, 81 (1993).

[3] Y. Kajiwara, K. Harii, S. Takahashi, J. Ohe, K. Uchida, M. Mizuguchi, H. Umezawa, H. Kawai, K. Ando, K. Takanasahi, S. Maekawa, and E. Saitoh, Nature (London) **464**, 262 (2010).

[4] C. W. Sandweg, Y. Kajiwara, K. Ando, E. Saitoh, and B. Hillebrands, Appl. Phys. Lett. **97**, 252504 (2010).

[5] C. W. Sandweg, Y. Kajiwara, A. V. Chumak, A. A. Serga, V. I. Vasyuchka, M. B. Jungfleisch, E. Saitoh, and B. Hillebrands, Phys. Rev. Lett. **106**, 216601 (2011).

[6] B. Heinrich, C. Burrowes, E. Montoya, B. Kardasz, E. Girt, Y.-Y. Song, Y. Sun, and M. Wu, Phys. Rev. Lett. **107**, 066604 (2011).

[7] S. M. Rezende, R. L. Rodriguez-Suarez, M. M. Soares, L. H. Vilela-Leao, D. L. Dominguez, and A. Azevedo, Appl. Phys. Lett. **102**, 012402 (2013).

[8] L. H. Vilela-Leao, A. A. C. Salvador, and S. M. Rezende, Appl. Phys. Lett. **99**, 102505 (2011).

[9] K. Ando and E. Saitoh, Phys. Rev. Lett. **109**, 026602 (2012).

[10] C. Burrowes, B. Heinrich, B. Kardasz, E. A. Montoya, E. Girt, Y. Sun, Y.-Y. Song, and M. Wu, Appl. Phys. Lett. **100**, 092403 (2012).

[11] M. B. Jungfleisch, V. Lauer, R. Neb, A. V. Chumak, and B. Hillebrands, Appl. Phys. Lett. **103**, 022411 (2013).

[12] C. Hahn, G. de Loubens, M. Viret, O. Klein, V. V. Naletov, and J. B. Youssef, Phys. Rev. Lett. **111**, 217204 (2013).

[13] Y. Tserkovnyak, A. Brataas, G. E. W. Bauer, and B. I. Halperin, Rev. Mod. Phys. **77**, 1375 (2005).

[14] A. Brataas, A. D. Kent, and H. Ohno, Nat. Mater. **11**, 372 (2012).

[15] Y. Tserkovnyak, A. Brataas, and G. E. W. Bauer, Phys. Rev. Lett. **88**, 117601 (2002).

[16] J. Xiao and G. E. W. Bauer, Phys. Rev. Lett. **108**, 217204 (2012).

[17] A. Brataas, Y. Tserkovnyak, G. E. W. Bauer, and P. J. Kelly, in *Spin Current*, edited by S. Maekawa, S. O. Valenzuela, E. Saitoh, and T. Kimura (Oxford University Press, 2012).

[18] A. Kapelrud and A. Brataas, Phys. Rev. Lett. **111**, 097602 (2013).

[19] P. Monod, H. Hurdequint, A. Janossy, J. Obert, and J. Chaumont, Phys. Rev. Lett. **29**, 1327 (1972).

[20] R. H. Silsbee, A. Janossy, and P. Monod, Phys. Rev. B **19**, 4382 (1979).

[21] A. Janossy and P. Monod, Phys. Rev. Lett. **37**, 612 (1976).

[22] S. Mizukami, Y. Ando, and T. Miyazaki, Jpn. J. Appl. Phys. **40**, 580 (2001).

[23] R. Urban, G. Woltersdorf, and B. Heinrich, Phys. Rev. Lett. **87**, 217204 (2001).

[24] A. Brataas, Y. Tserkovnyak, G. E. W. Bauer, and B. I. Halperin, Phys. Rev. B **66**, 060404 (2002).

[25] Y. Tserkovnyak, A. Brataas, and G. E. W. Bauer, Phys. Rev. B **66**, 224403 (2002).

[26] E. Šimánek and B. Heinrich, Phys. Rev. B **67**, 144418 (2003).

[27] A. Brataas, Y. Tserkovnyak, and G. E. W. Bauer, Phys. Rev. Lett. **101**, 037207 (2008).

[28] L. Berger, Phys. Rev. B **54**, 9353 (1996).

[29] J. Slonczewski, J. Magn. Magn. Mater. **159**, L1 (1996).

[30] Z. Qiu, J. Li, D. Hou, E. Arenholz, A. T. N’Diaye, A. Tan, K.-i. Uchida, K. Sato, S. Okamoto, Y. Tserkovnyak, Z. Q. Qiu, and E. Saitoh, Nat. Commun. **7**, 12670 (2016).

[31] T. Gilbert, Phys. Rev. **100**, 1243 (1955).

[32] S. Demokritov, B. Hillebrands, and A. Slavin, Phys. Rep. **348**, 441 (2001).

[33] T. Gilbert, IEEE Trans. Magn. **40**, 3443 (2004).

[34] B. A. Kalinikos, Sov. Phys. J. **24**, 718 (1981).

[35] B. A. Kalinikos and A. N. Slavin, J. Phys. C **19**, 7013 (1986).

[36] R. Damon and J. Eshbach, J. Phys. Chem. Solids **19**, 308 (1961).

[37] J. R. Eshbach and R. W. Damon, Phys. Rev. **118**, 1208 (1960).

[38] H. Puszkarski, IEEE Trans. Magn. **9**, 22 (1973).

[39] R. E. D. Wames and T. Wolfram, J. Appl. Phys. **41**, 987 (1970).
[40] G. Rado and J. Weertman, J. Phys. Chem. Solids **11**, 315 (1959).
[41] H. J. Jiao and G. E. W. Bauer, Phys. Rev. Lett. **110**, 217602 (2013).
[42] Z. Qiu, K. Ando, K. Uchida, Y. Kajiwara, R. Takahashi, T. An, Y. Fujikawa, and E. Saitoh, Appl. Phys. Lett. **103**, 092404 (2013).
[43] H. L. Wang, C. H. Du, Y. Pu, R. Adur, P. C. Hammel, and F. Y. Yang, Phys. Rev. Lett. **112**, 197201 (2014).
[44] F. R. Morgenthaler, IEEE Trans. Magn. **8**, 130 (1972).
[45] W. Press, S. Teukolsky, W. Vetterling, and B. Flannery, *Numerical Recipies*, 3rd ed. (Cambridge University Press, 2007).

Paper 4

Training and recovery behaviors of exchange bias in FeNi/Cu/Co/FeMn spin valves at high field sweep rates

J. Magn. Magn. Mater., 324, 3223-3226 (2012) - Published May 15, 2012

Journal of Magnetism and Magnetic Materials 324 (2012) 3223–3226

Contents lists available at SciVerse ScienceDirect

Journal of Magnetism and Magnetic Materials

journal homepage: www.elsevier.com/locate/jmmm

Training and recovery behaviors of exchange bias in FeNi/Cu/Co/FeMn spin valves at high field sweep rates

D.Z. Yang [a,b], A. Kapelrud [a], M. Saxegaard [a], E. Wahlström [a,*]

[a] Institutt for fysikk, NTNU, NO-7491 Trondheim, Norway
[b] The Key Laboratory for Magnetism and Magnetic Materials of Ministry of Education, Lanzhou University, Lanzhou 730000, China

A R T I C L E I N F O

Article history:
Received 1 September 2011
Received in revised form
20 April 2012
Available online 15 May 2012

Keywords:
Antiferromagnet
Exchange bias
Training effect

A B S T R A C T

Training and recovery of exchange bias in FeNi/Cu/Co/FeMn spin valves have been studied by magnetoresistance curves with field sweep rates from 1000 to 4800 Oe/s. It is found that training and recovery of exchange field are proportional to the logarithm of the training cycles and recovery time, respectively. These behaviors are explained within the model based on thermal activation. For the field sweep rates of 1000, 2000 and 4000 Oe/s, the relaxation time of antiferromagnet spins are 61.4, 27.6, and 11.5 in the unit of ms, respectively, much shorter than the long relaxation time ($\sim 10^2$ s) in conventional magnetometry measurements.

1. Introduction

The exchange bias (EB) effect in ferromagnetic/antiferromagnetic systems has been intensely studied in the last decade because of their physical complexity and important applications [1,2]. The technological importance lies in the pinning effect of the antiferromagnet (AFM) layers in which the hysteresis loop of the ferromagnet (FM) can be shifted away from the origin point by the amount of the exchange field (H_E), and is usually accompanied with an enhanced coercivity (H_C). Changes of H_E and H_C are accordingly directly related to the spin configuration of the AFM layer through the exchange coupling [3]. Among the variety of effects related to the EB phenomenon, the training effect is an important effect that reflects the AFM spin dynamic process during repeated hysteresis loops. It is ascribed to that the spin structure of the AFM layer deviates from its equilibrium configuration and approaches another equilibrium triggered by subsequent reversals of the FM magnetization. Nowadays, studies of AFM spin dynamic behaviors with training effect in both experiments and theories have been widely reported [4–13]. Because most of studies are limited to long timescales (>1 s), by the usually quite long measurement time in magnetometry approaches, the relaxation time of AFM spin are usually reported in second timescale ($\sim 10^2-10^4$ s) [4–6]. In contrast, at shorter measurement timescales the relaxation time of exchange bias system was demonstrated to cover a wide range ($\sim 10^{-8}-10^{11}$ s) [15–18], which has been ascribed to the magnetization reversal mechanism of FM layer [14]. Hence, the report *only* on AFM spin dynamic behavior in the millisecond timescale is still sparse. In addition, recently attempt frequencies up to 10^{12} Hz in AFM layer have been reported [19], which indicated a much shorter relaxation timescale of AFM spin than earlier anticipated. Therefore, it is necessary and interesting to study the AFM spin dynamic process at short timescale (technologic importance <1 s).

In this paper, we have studied the EB training and recovery behaviors at the *millisecond timescale* based on the electrical transport measurements in FeNi/Cu/Co/FeMn spin valves. The experiments show that at high field sweep rates recovery time of exchange field after training procedures is three orders of magnitude shorter than the values observed by usual magnetometry techniques, and the relaxation of magnetoresistance (MR) is demonstrated in the millisecond timescale. These clearly indicate that AFM spin dynamic behaviors can be studied and resolved down to the millisecond timescale utilizing the ordinary resistance measurements.

2. Experiment and results

The spin valves of Si (001)/Cu (10 nm)/$Fe_{20}Ni_{80}$ (3 nm)/Cu (3 nm)/Co (3 nm)/FeMn (8 nm)/Ta (3 nm) were prepared by a magnetron sputtering system. The base pressure was 2×10^{-5} Pa and the Ar pressure was 0.3 Pa during the deposition. The 10 nm Cu buffer layer was used to stimulate the fcc (1 1 1) preferred growth of the FeMn layer in order to enhance the EB. A magnetic field of 130 Oe was applied in the film plane during deposition to induce the uniaxial anisotropy and thus the EB.

---

* Corresponding author at: Institutt for fysikk, NTNU, NO-7491 Trondheim, Norway.
E-mail address: erik.wahlstrom@ntnu.no (E. Wahlström).

0304-8853/$ - see front matter © 2012 Elsevier B.V. All rights reserved.
http://dx.doi.org/10.1016/j.jmmm.2012.05.002

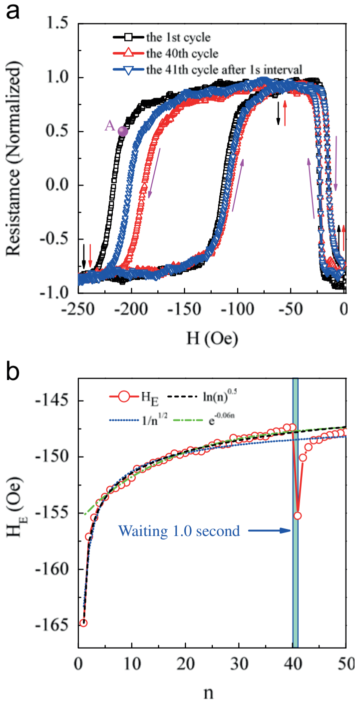

Fig. 1. (a) The magnetoresistance curves used to map the training effect for FeNi/Cu/Co/FeMn spin valve at the first, 40th and 41st (after 1 s waiting time) cycles with the field sweep rate of 4000 Oe/s. The resistance is dependent on corresponding magnetization configurations of FeNi (black left arrow) and Co (red right arrow). (b) The exchange field H_E as a function of the number of cycles n. The blue dot, green dash dot and black dash lines are the fitted data with the $1/\sqrt{n}$, $e^{-0.06n}$ and $\ln(n)$,respectively. (For interpretation of the references to color in this figure caption, the reader is referred to the web version of this article.)

Magnetoresistance (MR) measurements were performed to probe the switching behaviors of the pinned layer for different subsequent hysteresis loops. The magnetic field was provided by home-built Helmholtz coils, and MR was measured in real-time system with 2 M/s sampling rate. To study training and recovery of the EB, we first performed 40 consecutive MR measurements with a fixed field sweep rate to characterize the training procedures. Then we stopped the magnetic field sweep with an waiting time t. Finally 10 consecutive MR measurements with the same field sweep rate were measured in order to observe and confirm the EB recovery. For each sweep rate, t varied from 0.1 to 10 s.

The spin valves and MR curves of the training and recovery effects at the 1st, 40th and 41st cycles with the field sweep rate of 4000 Oe/s are displayed in Fig. 1(a). At large negative field the Co and FeNi magnetizations are parallel and pointing down. When the field is increased above the switch field of the Co layer, about −110 Oe, the Co magnetization reverses and resistance switches from low value (−1) to high value (+1). When the field is further increased above the switch field of the FeNi layer, about −15 Oe, its magnetization reverses, the two magnetizations become parallel once more but this time pointing up, and resistance switches to low value (−1). If the field is then decreased, the two magnetizations will remain parallel until the negative switch field of the FeNi layer is reached at −25 Oe, when its magnetization reverses and resistance switches to high value. When the field is further reduced and reverses the Co magnetization, the two magnetizations align in parallel, and resistance changes to its low value. For all MR curves the hysteresis loops of the Co layer are shifted and fully separated from the hysteresis loops of FeNi layer due to the FeMn pinning effect, therefore the MR curves directly reflect the switching behaviors of the Co and the FeNi layers in detail [20]. Comparing the hysteresis loops of the Co layer in the first, and 40th MR curves, the switching field of the descent branch shifts more sharply than that of the ascent one, demonstrating the asymmetric magnetization reversal. However, after the magnetic field sweep is stopped for 1 s, a recovery is observed in the 41st MR curve. It contrasts to the behavior in the case of normally low field sweep rate, in which substantial recovery was only observed after several hours of waiting time [4]. The H_E is plotted as a function of cycles n in Fig. 1(b). The H_E gradually decreases with the cycle n, has an obvious resilience after 1 s waiting time and finally decreases. For the training procedure, the H_E versus n is fitted by a linear functions of $1/\sqrt{n}$, $e^{-0.06n}$ and $\ln(n)$. It is found that the logarithm function yields the best fit, except for initial point $n=1$ [8,10].

To further study the recovery of the trained EB, we measured the recovery rate R as a function of t at different field sweep rates, where $R=[H_E(41)-H_E(40)]/[H_E(1)-H_E(40)]\times 100(\%)$. Fig. 2(a) shows the dependence of R on t at different field sweep rates. The R increases with the increasing t as a linear function of $\log(t)$.

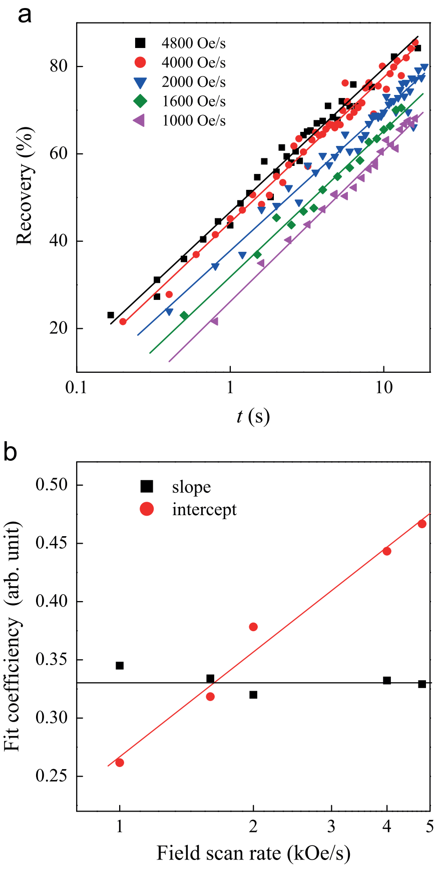

Fig. 2. (a) The recovery of H_E as a function of the waiting time t with different sweep rates. The solid lines display the linear fits of the $\ln(t)$. (b) The slope and the offset values as a function of the field sweep rate. The solid lines are the linear fits of the logarithm of the field sweep rate.

More remarkably, for a fixed waiting time *t*, *R* correspondingly increases with the increasing field sweep rate. This logarithm behavior is in a good agreement with the previous experiments in NiFe/FeMn system, while the recovery rate is several orders of magnitude faster than the value in the low field sweep rate case [4]. The slope and the intercept as a function of the field sweep rate are shown in Fig. 2(b). The slope displays little change with different field sweep rates whereas the intercept increases greatly as the field sweep rate increases in approximate linear function of the logarithm of the field sweep rate.

To investigate the dynamic behavior of the EB with high resolution, we observed the evolution of MR after setting the magnetic field from the positive saturation field to -210 Oe (the point A in Fig. 1(a)) near the switch field. As shown in Fig. 3, MR initially decreases sharply and then gradually reaches a constant. The small fluctuations in the curves are caused by 50 Hz AC noise in the amplifying circuit. Remarkably, a crossover of the normalized MR from positive to negative has been observed, demonstrating the reversal of the magnetization of the Co layer. It is possible to link the time dependence of MR with the magnetic viscosity in the Co/FeMn bilayers [7], in which the magnetization of the pinned layer gradually reverses due to the thermally activated process in Co/FeMn bilayers. Because the reversal process in the EB at the first cycle consists in the single domain wall motion [6], the change of MR here is proportional to the amounts of the reversal magnetization in the pinned layer. Shown as the solid line in Fig. 3, the evolutions of MR are described well by a first order exponential decay. From fitting the data, we extracted the relaxation times τ which are 11.5, 27.6, and 61.4 ms for the field sweep rate at 4000, 2000 and 1000 Oe/s, respectively. This is again in contrast to the long relaxation time (~ 800 s) in the conventional approaches [6]. One can also note that the relaxation time decreases with the increasing field sweep rate.

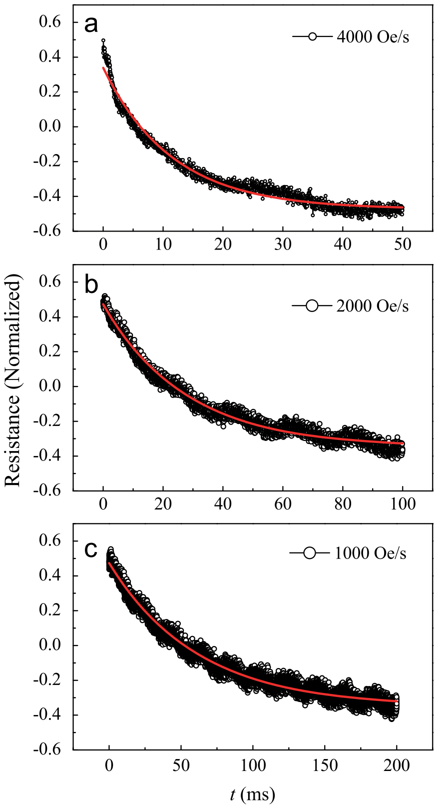

Fig. 3. The time dependence of the resistance after the external magnetic field is swept to -210 Oe (point A in Fig. 1(a)) from positive saturation field with different field sweep rates (a) 4000 Oe/s, (b) 2000 Oe/s, and (c) 1000 Oe/s. The solid lines are fits to the first-order exponential decay.

3. Discussion

The above results show that the recovery and relaxation of the EB at high field sweep rates are faster than that earlier observed [4–7]. Below we will interpret the experimental results in conventional models for AFM and training effects.

Firstly we consider the change and magnitude of the relaxation time constants at different field sweep rates shown in Fig. 3. The time constant for the relaxation can be described by an ordinary Arrhenius law $\tau = \nu_\sigma^{-1} \exp(E_\sigma / k_B T)$, where ν_σ is the attempting frequency and $E_\sigma = KV$ represents the AFM energy barrier, K is the AFM anisotropy and V is the AFM grain volume. According to the AFM grain volumes distribution, we can divide the E_σ into three different categories [10]: (i) small E_σ (small grain size), which follows the FM magnetization at the timescale of the experiment. (ii) Medium energy E_σ (medium grain size) which will determine the EB dynamics at the timescale we investigate. (iii) Large E_σ (large grain size), which is a stable configuration over the timescale of the experiment. Assuming a typical uniaxial anisotropy constant of 1×10^6 erg/cm^3 and ν_σ to be 1×10^9 Hz, then the average grain size of category (ii) is correspondingly about 9 nm extension, based on the relaxation time in Fig. 3. Accordingly, the relaxation time decreasing with the increasing field sweep rate demonstrates an apparent increase in attempt frequency ν_σ.

The EB recovery and relaxation at high field sweep rates can still be explained well with the model based on thermal activation [4,23]. As shown in Fig. 2(a), the logarithm time recovery relationship indicates a thermally activated reversal process involving the AFM spin configuration. To explain our data, the activation energy spectrum model simply based on a two-level system is adopted [23,24]. In our case the two level system represents an individual AFM grain or domain switching from a positive to a negative exchange energy with respect to the FM layer. For the system with a wide energy barrier distribution, ΔH_E can be expressed in terms of the AFM activation energy spectrum $q(E)$: $\Delta H_\mathrm{E} = q(E) k_B T \ln(\nu_\sigma t)$, which is taken from Eq. (1) in Ref. [4]. According to the equation, the slope observed for all field rates in Fig. 2(b) is a constant due to the same $q(E)$, while the intercept variation is mainly due to the different activated AFM energy ranges and the time delay at the different field sweep rates.

Finally, for the training process H_E is proportional to $\ln(n)$ at high field sweep rates in Fig. 1(b), which can be compared to the usual power law $(1/\sqrt{n})$ and the exponential $(e^{-\alpha n})$ relationships. We model this through following Binek et al. [21,22]. At beginning, the equilibrium AFM interface magnetization is defined $S^e_{AFM} = \lim_{n\to\infty} S_{AFM}(n)$. Each positive and negative deviation $\delta S_n = S_{AFM}(n) - S^e_{AFM}$ of the AFM interface magnetization from its equilibrium value will increase the total free energy F of the system by ΔF. The relaxation of the system towards equilibrium is determined by the Landau–Khalatnikov (LK) equation [25]: $\xi \dot{S}_{AFM} = -\partial \Delta F / \partial S_{AFM}$, where ξ is a phenomenological damping constant and ΔF is the function of δS. In Binek's model under the assumption $\Delta F(\delta S) = \Delta F(-\delta S)$, a series expansion of ΔF up to the fourth order in δS yields $\Delta F = \frac{1}{2} a(\delta S)^2 + \frac{1}{4} b(\delta S)^4 + O(\delta S)^6$. Evaluating the free energy expression with a leading term of second and fourth order in δS will result in the $e^{-\alpha n}$ [22] and $1/\sqrt{n}$ [21] evolution, respectively.

However, our understanding of the system is that we have a nonvanishing odd order term. This is an effect of working at a time scale where we also have substantial coupling at the FM/AFM interface due to large grains that are too large to follow the oscillating exchange coupling of the FM. Instead that portion of the ensemble of grain will orient itself gradually according to the mean coupling induced by the FM in a monotonic fashion. Accordingly we also have to consider the expansion of ΔF from first order of δS. We then assume $\delta S: \Delta F = f(n)(\delta S)^1 + O(\delta S)^2$, where the $f(n)$ indicates that the change in the AFM interface magnetization and δS_n is dependent on the training procedures n. By replacing $\dot{S}$ with $[S(n+1)-S(n)]/\lambda$, with λ being the relevant experimental time constant and the free energy expression of the first order into the LK equation, we obtain an implicit sequence equation: $\xi'(S(n+1)-S(n)) = -f(n)$, where $\xi' = \xi/\lambda$. The sum over N cycles of this equation with variable n yields $H_E(N+1) \propto S(N+1) = S(1) - \sum_{n=1}^{N} f(n)/\xi'$.

Since we do not know the exact energy distribution $F(V)$ of our system, we make a first-order approximation assuming a constant distribution of AFM grain volumes. An estimate of the change in thermally activated part of the interface magnetization can be found through: $f(n) = \int_{V_n}^{V_{n+1}} F(V)\, dV$, using a thermally activated grain volume V_n which is found through the Arrhenius expression and a constant distribution in volume $F(V)$ we find that $f(n)$ will follow a $\ln(n+1)-\ln(n)$ dependence, a logarithmic dependence of the exchange bias. This approximation may only be valid at large n when the overall reorientation due to the changed mean field dominate over other training effects. We also note that the training process H_E is proportional to $\ln(n)$ has also been reported at low field sweep rates [8], where the training speed is several orders of magnitude slower than the values reported here.

In summary, for the AFM spins the relaxation time in the millisecond timescale is demonstrated when the bilayers are exposed to high field sweep rates. This behavior can be well explained in terms of a time constrained thermal activation. Our finding gives a new insight into the dynamic behavior of the AFM spins.

Acknowledgments

We gratefully acknowledge helpful and fruitful discussions with S.M. Zhou. The work was supported by the Norwegian Research Council, Frinat project 171332. The author D.Z. Yang acknowledges the funding supported by the National Natural Science Foundation of China under Grand no. 11104122; the Fundamental Research Funds for the Central Universities lzujbky-2011-51.

References

[1] J. Nogues, I.K. Schuller, Journal of Magnetism and Magnetic Materials 192 (1999) 203.

[2] A.E. Berkowitz, K. Takano, Journal of Magnetism and Magnetic Materials 200 (1999) 552.

[3] X.P. Qiu, D.Z. Yang, S.M. Zhou, R. Chantrell, K. O'Grady, U. Nowak, J. Du, X.J. Bai, L. Sun, Physics Review Letters 101 (2008) 147207.

[4] J. Dho, C.W. Leung, M.G. Blamire, Journal of Applied Physics 99 (2006) 033910.

[5] P.A.A. van der Heijden, T.F.M.M. Maas, W.J.M. de Jonge, J.C.S. Kools, F. Roozeboom, P.J. van der Zaag, Applied Physics Letters 72 (1998) 492.

[6] E. Pina, C. Prados, A. Hernando, Physical Review B 69 (2004) 052402.

[7] C. Leighton, I.K. Schuller, Physical Review B 63 (2001) 174419.

[8] C.Y. Hung, M. Mao, S. Funada, T. Schneider, L. Miloslavsky, M. Miller, C. Qian, H.C. Hong, Journal of Applied Physics 87 (2000) 4915.

[9] M.J. Carey, N. Smith, B.A. Gurney, J.R. Childress, T. Lin, Journal of Applied Physics 89 (2001) 6579.

[10] M.K. Chan, J.S. Parker, P.A. Crowell, C. Leighton, Physical Review B 77 (2008) 014420.

[11] T. Hughes, K. O'Grady, H. Laidler, R.W. Chantrell, Journal of Magnetism and Magnetic Materials 235 (2001) 329.

[12] H.W. Xi, S. Franzen, S.N. Mao, R.M. White, Physical Review B 75 (2007) 014434.

[13] A.G. Biternas, R.W. Chantrell, U. Nowak, Physical Review B 82 (2010) 134426.

[14] B. Raquet, M.D. Ortega, M. Goiran, A.R. Fert, J.P. Redoules, R. Mamy, J.C. Ousset, A. Sdaq, A. Khmou, Journal of Magnetism and Magnetic Materials 150 (1995) L5.

[15] F. Garcia, J. Moritz, F. Ernult, S. Auffret, B. Rodmacq, B. Dieny, J. Camarero, Y. Pennec, S. Pizzini, J. Vogel, IEEE Transactions on Magnetics 38 (2002) 2730.

[16] J. Camarero, Y. Pennec, J. Vogel, M. Bonfim, S. Pizzini, M. Cartier, F. Ernult, F. Fettar, B. Dieny, Physical Review B 64 (2001) 172402.

[17] A M Goodman, K. O'Grady, H. Laidler, N.W. Owen, X. Portier, A.K. Petford-Long, F. Cebollada, IEEE Transactions on Magnetics 37 (2001) 565.

[18] S. Sahoo, S. Plisetty, Ch. Binek, A. Berger, Journal of Applied Physics 101 (2007) 053902.

[19] G. Vallejo-Fernandez, N.P. Aley, J.N. Chapman, K. O'Grady, Applied Physics Letters 97 (2010) 222505.

[20] J. Ventura, J.P. Araujo, J.B. Sousa, A. Veloso, P.P. Freitas, Physical Review B 77 (2008) 184404.

[21] Ch. Binek, Physical Review B 70 (2004) 014421.

[22] Ch. Binek, S. Polisetty, X. He, A. Berger, Physics Review Letters 96 (2006) 067201.

[23] E. Fulcomer, S.H. Charap, Journal of Applied Physics 43 (1972) 4190.

[24] M.R.J. Gibbs, J.E. Evetts, J.A. Leake, Journal of Materials Science 18 (1983) 278.

[25] G. Vizdrik, S. Ducharme, V.M. Fridkin, G. Yudin, Physical Review B 68 (2003) 094113.